DESIGN AND ANALYSIS OF MODEL REFERENCE ADAPTIVE CONTROL ON THE ENERGY MANAGEMENT SYSTEM OF AN ELECTRIC VEHICLE

BY

MAIDUL ISLAM

A thesis submitted in fulfillment of the requirement for the degree of Doctor of Philosophy in Engineering.

Kulliyyah of Engineering
International Islamic University Malaysia

DECEMBER 2024

ABSTRACT

Electric vehicles (EVs) have become a favourable choice due to the current environmental conditions and limited fuel resources. For efficient operation, EVs often use a lithium-ion battery as its main power source. Nevertheless, during acceleration, EVs require an instant high load demand, which is quite challenging to satisfy with the lithium-ion battery alone due to its slow discharging rate. This frequent fluctuation can damage the batteries' State of Health (SoH), and to overcome this issue, a Hybrid Energy Storage System (HESS) is proposed. In the system, a Supercapacitor (SC) is used to support the immediate load demand from a vehicle. To ensure that the correct amount of power is extracted, a suitable controller needs to be integrated with a Bidirectional DC-DC Converter (BDC). As a model disturbance can influence both the load demand and system feedback response, a novel contribution of this work is to introduce the application of Model Reference Adaptive Control (MRAC) to overcome this issue. A detailed derivation of this algorithm, along with the investigation of the tuning effect, is presented. To analyse the efficacy of this controller, several numerical simulations have been carried out using MATLAB/Simulink, where the MRAC performance is benchmarked against the Proportional Integral (PI) controller, based on several performance indexes such as Root Mean Square Error (RMSE) of current and voltage, power demand tracking, and controllers' characteristics. For regular operation, the results show that MRAC outperforms the PI controller in tracking voltage demand by 67% (with constant voltage) and 85% (with variable voltage) with inverting BDC and current demands by 16% (with variable current) in non-inverting BDC. While in the presence of disturbance, MRAC shows its efficacy in current demand tracking by surpassing PI controller with 15% higher accuracy. In this case, MRAC requires some time due to adjust its mechanism to surpass the PI controller in tracking the load demand. To validate the MRAC design, an EV model, designed by MathWorks has been utilised upon the integration of the HESS with a Power Management System (PMS) that operated with four (4) different driving cycles, approved by the Environmental Protection Agency (EPA), such as US06, Urban Dynamometer Driving Schedule (UDDS), Highway Fuel Economy Test (HWEFT) and Federal Test Procedure (FTP). The comparison results show MRAC consistently demonstrates superior current tracking compared to PI controller under disturbance conditions, as evidenced by significantly lower RMSE values in HWFET (8.15 vs. 39.74), UDDS (7.4 vs. 31.97), and FTP (6.34 vs. 24.89) drive cycles, respectively. Finally, the results of this study highlight the potential of adaptive control strategies in improving the efficiency, stability, and reliability of power management systems along with BDC for Hybrid Electric Vehicles (HEVs).

ملخص البحث

تشكل السيارات الكهربائية (EVs) خيارًا مفضلًا في ظل الظروف البيئية الحالية وندرة موارد الوقود. لضمان التشغيل الفعّال، تستخدم السيارات الكهربائية عادةً بطارية ليثيوم-أيون كمصدر رئيسي للطاقة. ومع ذلك، تتطلب السيارات الكهربائية أثناء التسارع حملًا فوريًا عاليًا، وهو ما يمثل تحديًا كبيرًا لتلبيته باستخدام بطارية الليثيوم-أيون وحدها بسبب معدل تفريغها البطيء. يمكن أن تؤدي هذه التقلبات المتكررة إلى تدهور حالة صحة البطاريات .(SoH) وللتغلب على هذه المشكلة، تم اقتراح نظام تخزين طاقة هجين (HESS)، حيث يتم استخدام المكثف الفائق (SC) لدعم الحمل الفوري المطلوب من السيارة. لضمان استخلاص الكمية الصحيحة من الطاقة، يجب دمج وحدة تحكم مناسبة مع محول تيار مستمر ثنائي الاتجاه .(BDC) نظرًا لأن اضطرابات النموذج يمكن أن تؤثر على كل من الحمل المطلوب واستجابة النظام، فإن الإسهام الجديد لهذا العمل يتمثل في تطبيق التحكم التكيفي المرجعي النموذجي (MRAC) للتغلب على هذه المشكلة. يتم تقديم اشتقاق مفصل لهذا الخوارزمية، مع دراسة تأثير ضبط المعايير. لتحليل فعالية هذه الخوارزمية، تم إجراء العديد من المحاكاة العددية باستخدام برنامج MATLAB/Simulink، حيث تمت مقارنة أداء MRAC مع وحدة التحكم التناسبي التكاملي (PI) استنادًا إلى عدة مؤشرات أداء مثل جذر متوسط المربع (RMSE) للتيار والجهد، وتتبع متطلبات الطاقة، وخصائص وحدات التحكم. تظهر النتائج، في ظروف التشغيل العادية، أن MRAC يتفوق على وحدة التحكم PI في تتبع متطلبات الجهد بنسبة 67٪ (مع جهد ثابت) و85٪ (مع جهد متغير) باستخدام محول تيار مستمر عاكس، وفي تتبع متطلبات التيار بنسبة 16٪ (مع تيار متغير) باستخدام محول تيار مستمر غير عاكس. أما في وجود الاضطرابات، فإن MRAC يثبت فعاليته في تتبع متطلبات التيار من خلال تفوقه على وحدة التحكم PI بدقة أعلى بنسبة 15٪. في هذه الحالة، يحتاج MRAC إلى

بعض الوقت لتعديل آليته من أجل التفوق على وحدة التحكم PI في تتبع الحمل المطلوب. لتأكيد تصميمMRAC ، تم استخدام نموذج للسيارة الكهربائية مصمم بواسطة MathWorksبعد دمج HESS مع نظام إدارة الطاقة (PMS) الذي يعمل مع أربع دورات قيادة مختلفة، معتمدة من قبل وكالة حماية البيئة(EPA) ، مثلUS06 ، الجدول الزمني للقيادة الديناميكية الحضرية(UDDS) ، اختبار اقتصاد الوقود على الطرق السريعة(HWFET) ، وإجراءات الاختبار الفيدرالية .(FTP) تظهر نتائج المقارنة أن MRACيظهر باستمرار أداءً متفوقًا في تتبع التيار مقارنة بوحدة التحكم PI في ظروف الاضطرابات، وهو ما يتضح من خلال قيم RMSE الأقل بشكل ملحوظ في دورات القيادة 8.15) HWFET مقابل 39.74(، UDDS(7.4 مقابل 31.97)، و FTP(6.34 مقابل 24.89) على التوالي. أخيرًا، تبرز نتائج هذه الدراسة إمكانيات استراتيجيات التحكم التكيفية في تحسين كفاءة واستقرار وموثوقية أنظمة إدارة الطاقة، جنبًا إلى جنب مع محول التيار المستمر ثنائي الاتجاه في السيارات الهجينة الكهربائية(HEVs).

APPROVAL PAGE

The thesis of Maidul Islam has been approved by the following:

Muhammad Bin Abdullah
Supervisor

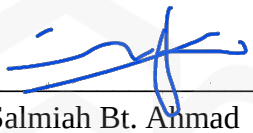

Salmiah Bt. Ahmad
Co-supervisor

Alia Farhana Binti Abdul Ghaffar
Co-supervisor

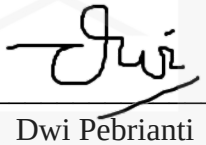

Dwi Pebrianti
Internal Examiner

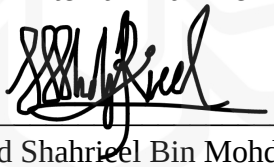

Mohd Shahrieel Bin Mohd Aras
External Examiner

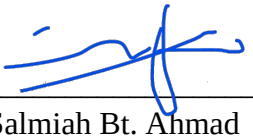

Salmiah Bt. Ahmad
Chairman

DECLARATION

I hereby declare that this thesis is the result of my own investigations, except where otherwise stated. I also declare that it has not been previously or concurrently submitted as a whole for any other degrees at IIUM or other institutions.

Maidul Islam

Signature…… Date……10/12/2024

INTERNATIONAL ISLAMIC UNIVERSITY MALAYSIA

DECLARATION OF COPYRIGHT AND AFFIRMATION OF FAIR USE OF UNPUBLISHED RESEARCH

DESIGN AND ANALYSIS OF MODEL REFERENCE ADAPTIVE CONTROL ON THE ENERGY MANAGEMENT SYSTEM OF AN ELECTRIC VEHICLE

I declare that the copyright holder of this thesis are jointly owned by the student and IIUM.

No part of this unpublished research may be reproduced, stored in a retrieval system, or transmitted, in any form or by any means, electronic, mechanical, photocopying, recording or otherwise without prior written permission of the copyright holder except as provided below

1. Any material contained in or derived from this unpublished research may only be used by others in their writing with due acknowledgement.

2. IIUM or its library will have the right to make and transmit copies (print or electronic) for institutional and academic purpose.

3. The IIUM library will have the right to make, store in a retrieval system and supply copies of this unpublished research if requested by other universities and research libraries.

By signing this form, I acknowledged that I have read and understand the IIUM Intellectual Property Right and Commercialization policy.

Affirmed by Maidul Islam

…… 10/12/2024 ……..

Signature Date

This thesis is dedicated to my parents and teachers for laying the foundation of what I turned out to be in life.

ACKNOWLEDGEMENTS

All glory is due to Allah, the Almighty, whose Grace and Mercies have been with me throughout the duration of my program. Although, it has been tasking, His Mercies and Blessings on me ease the herculean task of completing this thesis.

I am most indebted to supervisor, Assis. Prof. Dr Muhammad Bin Abdullah and Assis. Prof. Dr Alia Farhana Binti Abdul Ghaffar, whose enduring disposition, kindness, promptitude, thoroughness and friendship have facilitated the successful completion of my work. I keep on record and appreciate his detailed comments, useful suggestions and inspiring queries which have considerably improvedthis thesis. Their brilliant grasp of the aim and content of this work led to their insightful comments, suggestions and queries which helped me a great deal. Despite their commitments, they took time to listen and attend to me whenever requested. The moral support they extended to me is in no doubt a boost that helped in building and writing the draft of this research work. I am also grateful to my co-supervisor, Asst. Prof. Dr. Salmiah Bt. Ahmad, whose support and cooperation contributed to the outcome of this work.

Lastly, my gratitude goes to my parents; for their prayers, understanding and endurance while away.

Once again, I glorify Allah for His endless mercy on us, one of which is enabling me to successfully round off the efforts of writing this thesis. Alhamdulillah

CONTENTS

LIST OF FIGURES

LIST OF TABLES

LIST OF ABBREVIATIONS

ASIC	Application Specific Integrated Chip
BAC	Bidirectional DC-AC Converter
BDC	Bidirectional DC-DC Converter
BMS	Battery Management System
CAN	Controller Area Network
CCM	Continuous Conduction Mode
CV	Conventional Vehicle
DCM	Discontinuous Conduction Mode
MRAC	Direct Model Reference Adaptive Control
ECU	Electronic Control Unit
EDLC	Electric Double Layered Capacitor
EMS	Energy Management System
EPA	Environmental Protection Agency
EPS	Electrical Power System
ESS	Energy Storage System
EV	Electric Vehicle
FC	Fuel Cell
FTP	Federal Test Procedure
HEV	Hybrid Electric Vehicle
HWFET	Highway Fuel Economy Test
MPC	Model Predictive Control
IC	Internal Combustion
IGBT	Insulated-Gate Bipolar Transistor
Li-ion	Lithium Ion
MCU	Micro control unit

MDIBC	Multidevice/port Interleaved Bidirectional Converter
MPC	Model Predictive Control
MRAC	Model Reference Adaptive Control
Na-S	Sodium-Sulfur
NaNiCl	Sodium-Nickel Chloride
Ni-Cd	Nickel-Cadmium
Ni-MH	Nickel-Metal Hydride
Ni-Zn	Nickel-Zinc
OBID	On-Board Diagnosis
PCB	Printed Circuit Board
PCM	Phase Change Materials
PEV	Pure/Plugin Electric Vehicle
PHEV	Plugin Hybrid Electric Vehicle
PI	Proportional Integral
PID	Proportional Integral Derivative
PWM	Pulse Width Modulation
RMSE	Root Mean Square Error
SC	Supercapacitor
SMC	Sliding Mode Control
SMES	Superconducting Magnetic Energy Storage
SOC	State of Charge
SOH	State of Health
UDDS	Urban Dynamometer Driving Schedule
VRFB	Vanadium Redox Flow Battery
ZBFB	Zinc-Bromine Flow Battery
ZEBRA	Zero Emission Battery Research Activities
Zn-Air	Zinc-Air

CHAPTER ONE

INTRODUCTION

1.1 INTRODUCTION

Fossil fuel contributes to environmental pollution, and as its price is rising, electric-powered equipment has achieved great interest among researchers as an alternative energy. Since electricity can be generated from various renewable sources and is environmentally friendly, automotive policymakers are highly interested in bringing changes in the sources of energy for the transportation sector. Higher fuel economy, lower emissions and better performance are the key factors that motivate researchers to pay more attention to the development of electric vehicles as an alternative to internal combustion engine (Amjadi & Williamson, 2009; Emadi et al., 2008; Ghorbani et al., 2010; Khan & Tolbert, 2009). The ongoing demand can be observed from Figure 1.1, where it shows the dramatically increasing nature of the EV sales forecast from 2000 to 2040.

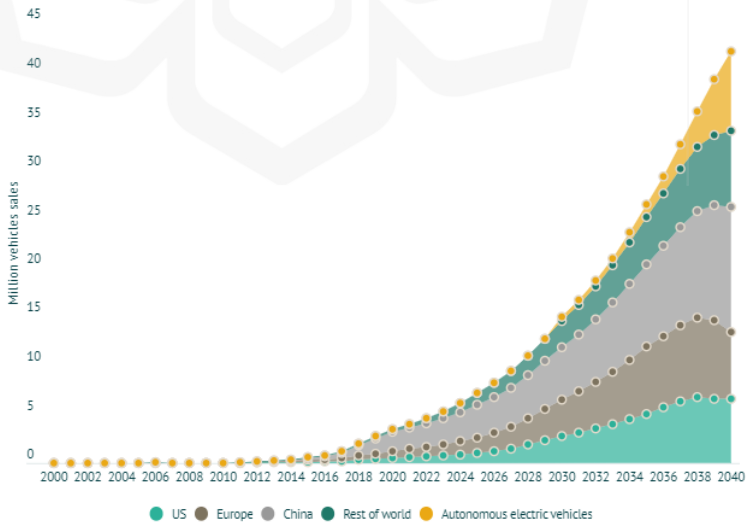

Figure 1.1 EV production from 2000 to 2010 (Mackenzie, 2020).

Figure 1.1 presents the evolution and growth of electric vehicle (EV) sales from 2000 to 2040, broken down by the United States, Europe, China, the rest of the world, and also the emergence of autonomous electric vehicles. From 2000 to 2010, EV sales are minimal across all regions. However, between 2010 and 2020, the industry begins to see gradual growth, especially in China due to the advancements in battery efficiency and lower costs. Post-2020, EV sales experience exponential growth, with China (dark green) becoming the dominant market by 2025, reflecting its aggressive EV adoption strategies. By 2030, EVs transition from niche to mainstream across most regions. At the same time, autonomous electric vehicles (yellow) begin to make significant progress around 2030, benefiting from advancements in AI, connectivity, and sensor technology. Early adoption occurs in regions with supportive regulations and advanced technology infrastructure. By 2040, it is projected that autonomous EVs represent a significant portion of the market, driven by the appeal of autonomous driving and electric propulsion. This data highlights the important in developing a technology specifically for EV.

1.1.1 Working Principle of Electric Vehicle

An electric vehicle consists of several important components, such as the battery, motor, and powertrain system, as shown in Figure 1.2. The batteries act as a storage system and provide Direct Current (DC) power, then the power converter will convert it into Alternate Current (AC) power to run the electric motors. The rotation speed from the motor is then transmitted through the transmission system to provide the required traction force according to the driver's demand. This is the basic working principle behind pure Battery

Electric Vehicles (BEVs), where the batteries can be recharged from any power grid through a plug-in system.

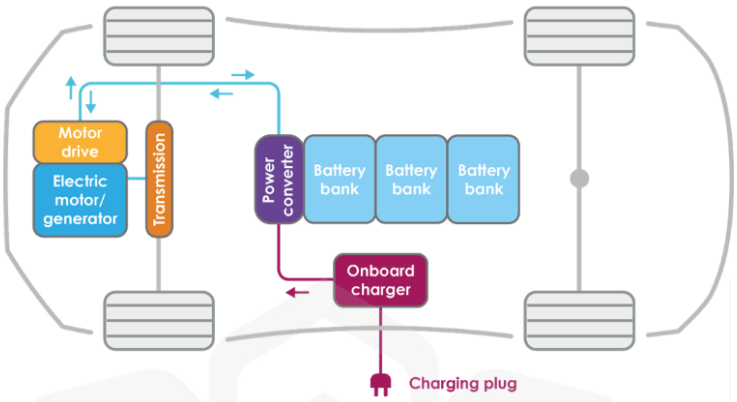

Figure 1.2 The drivetrain architecture of EV (Technology, 2020).

While Hybrid Electric Vehicle (HEV) and Plug-in Hybrid Electric Vehicle (PHEV) follow different working principles. For instance, HEVs primarily rely on internal combustion (IC) engines to generate traction force with conventional transmission systems while utilizing an electric motor as a secondary engine. In HEVs, batteries store the energy through a regenerative braking system from the IC engine power, especially when the vehicles are in braking mode. Figure 1.3 shows a HEV, Toyota Prius that receives popularity due to its fuel economy feature.

The PHEVs also have both an IC engine and an electric motor to run the car. Here, these vehicles are run by the electric motor at first, and after the depletion of the battery storage, they can switch to a powered engine system. Unlike HEVs, PHEVs have the features to recharge the batteries through a regenerative braking system or from any power grid. Hence, PHEVs are more similar to BEVs since the energy storage system of both vehicles can be recharged.

Figure 1.3 Toyota Prius (Maric, 2019)

1.1.2 Energy Storage Systems

Energy storage systems (ESSs) are one of the important components in EVs that have a similar function as a fuel tank. Its total capacity and fast energy release capability are two different factors that are widely considered in the design process (Lukic et al., 2008). Other characteristics also need to be considered, such as power density, energy density, cost, lifetime, and maintenance (Khaligh & Li, 2010). Based on these characteristics, the energy storage system can be categorized into chemical batteries, Supercapacitors (SCs), fuel cells, flywheels and engine generators (Khaligh & Li, 2010; Van Mierlo et al., 2004). It also can be categorized based on the method of storage such as chemical ESSs, electrical ESSs and thermal ESSs (Bindra & Revankar, 2018). In general, electromechanical batteries include lithium-ion, Nickel-Metal Hydride (Ni-MH), Nickel-Cadmium (Ni-Cd), Nickel-Zinc (Ni-Zn), Zinc-Air (Zn-Air), Sodium-Sulfur (Na-S), ZEBRA, and lead-acid can be considered as good candidates for storage devices (Azidin et al., 2013; Lukic et al., 2008; Tie & Tan, 2013). These batteries can be rechargeable and offer high power density, high specific energy, flat discharge profile and a wide thermal performance (Lukic et al., 2006).

Surprisingly, there is no such ESS that can satisfy all the requirements of HEVs, PHEVs and EVs. Hence, hybridization of ESS with a supercapacitor has been found in literature as a solution to enhance the performance of ESS and fulfil all possible requirements of EVs (Lukic et al., 2006; Ortúzar et al., 2007; Thounthong et al., 2009). SCs are mainly popular for their power densities, fast charging and discharging capacity and long life cycle with efficiency (Khaligh & Li, 2010). Thus, it can act as a secondary or backup power supply to the EV to fulfil the shortage of voltage. Nevertheless, a good Battery management System (BMS) is often needed.

1.1.3 Battery Management System (BMS)

BMS is responsible for managing the operation of a battery to ensure efficient, reliable, safe and durable operation (Xing et al., 2011). It helps to monitor the battery states such as SOC, SOH, state of available power (SOP) and state of battery life (SOL) (Ali et al., 2019). BMS is able to sense the battery current, voltage, charge, and temperature, which helps to avoid any sort of overcharge and over-discharge, over-voltage and overheating (M. A. Hannan et al., 2017; Lu et al., 2013). One of the responsibilities of BMS is to supply a suitable voltage to the motor to satisfy the load demand. Thus, BMS needs to rely on DC-DC converters to increase or decrease the voltage or current, maintaining the power according to the requirement. One of the common applications of DC-DC converters in a car is to convert high voltage to low voltage to meet the electrical equipment's demands, such as air conditioning, radio, lamp, etc. Section 1.1.4 will elaborate more about its necessity and working principles.

1.1.4 DC-DC Converter

DC-DC converter is a commonly used device in power electronics that adjusts the DC voltage or current according to the power demand of a system. In other words, a DC-DC converter is used to shift the DC input voltage and current to a required DC voltage or current. Figure 1.4 represents a block diagram of a DC-DC converter.

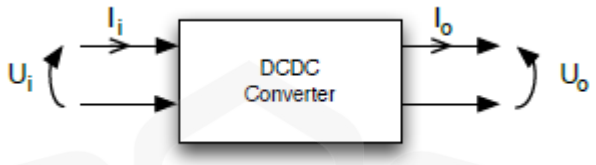

Figure 1.4 A block diagram of a DC-DC converter (Hedlund, 2010)

In practice, voltage, or current shifts through switch on and off with significantly high speed. During operation, when the output voltage (U_o) is greater than the input voltage (U_i), the converter works in buck mode. On the contrary, the converter works in the boost mode when the output voltage (U_o) is smaller than the input voltage (U_i). In automobiles, normally, the battery offers 250-360V, and SC provides 150-400V of voltage which are far from the DC-Bus demand of 400-750V of an EV. Hence, the step-up DC-DC converter is required for EV to meet the demand, and a step-down DC-DC converter is required to charge up the battery (Forouzesh et al., 2017).

A Bidirectional DC-DC converter (BDC) is a type of power electronics device that can convert direct current (DC) electrical power from one voltage level to another in two directions. Thus, it offers the feature of stepping up (boost) or stepping down (buck) the voltage and can transfer power in both directions between two DC sources. In the automobile industry, BDCs are inevitable components in many modern electrical systems,

particularly in EVs. As a DC-DC converter type, BDCs incorporate two types of circuit models: a boost circuit and a buck circuit. Importantly, the boost circuit increases the voltage from a lower level to a higher level, while the buck circuit decreases the voltage from a higher level to a lower level. Thus, the BDCs are able to direct and redirect power flow in both directions (Rashid, 2018).

A BDC extracts power from the main battery to supply auxiliary systems or recharge a secondary battery. In the reverse direction, it draws power from the regenerative braking or auxiliary sources to recharge the main battery or SC (Khaligh & Li, 2010). Importantly, a control system manages the direction and amount of power transfer to optimize the overall system performance. Therefore, researchers introduce several control algorithms for BDC, such as PI, PID (Ramya & Jegathesan, 2016), Model Predictive Control (MPC) (Pirooz & Noroozian, 2016), Sliding Mode Control (Ciccarelli & Lauria, 2010), H-infinity (Bai et al., 2019) and Backstepping (Khan et al., 2019) based on the suitability.

1.1.5 Working Principle of a BDC in EVs

While charging the ESSs (e.g., battery packs), the buck mode of a converter switches on, while during discharging or supplying the charge to the motors, the boost mode switches on. Figure 1.5 describes how power moves from battery and charger to motor and other electrical equipment. The battery is connected to a bidirectional DC-DC converter (BDC) to amplify the voltage, and the converter again sends it to a bidirectional DC-AC converter (BAC) to convert DC current into 3-phase AC current as the electric motor requires 3-phase current. In the meantime, the BDC also sends current to a unidirectional DC-DC converter

to step down the voltage and charge the small battery that is responsible for the car's internal usage. It is noted that during charging, the AC current is converted into DC current, and that's why a unidirectional AC-DC converter is used to transfer the current from the charger to the BDC that is directly connected to the battery to charge up the battery.

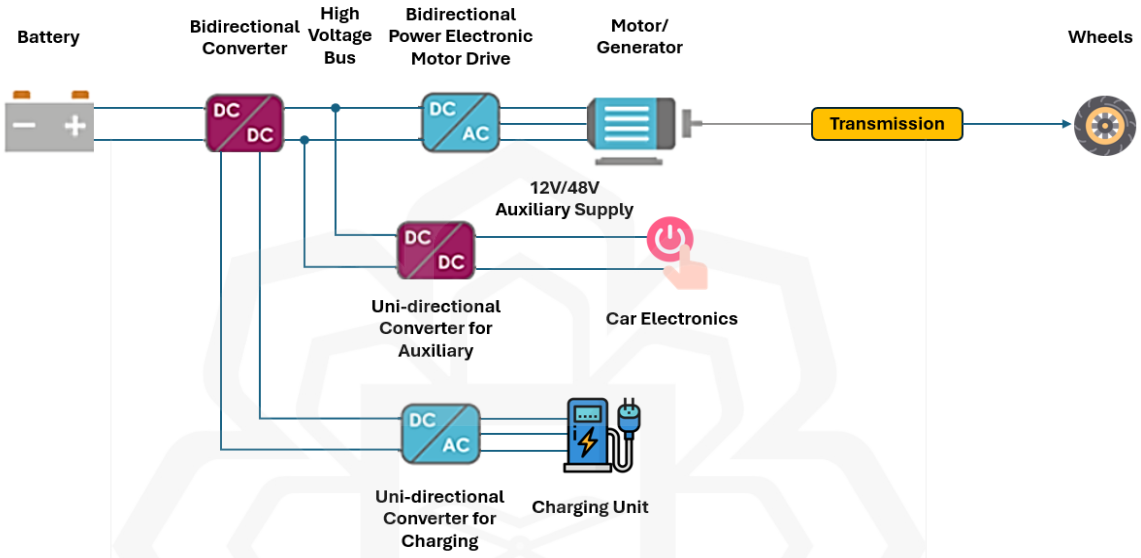

Figure 1.5 Schematic diagram of EV drivetrain architecture (Technology, 2020).

1.2 PROBLEM STATEMENT AND ITS SIGNIFICANCE

In this work, both the lithium-ion battery and supercapacitor have been considered as the sources of energy in electric vehicles where the battery is the primary source, and the supercapacitor is a secondary source. In general, an electric vehicle moves in three different modes such as i) acceleration mode, ii) normal (steady-state) mode and iii) regenerative braking mode (Pany et al., 2011).

In acceleration mode, the battery requires more power than in the normal mode, especially when climbing a hill. This demand may jeopardize the battery's health if extreme power is extracted frequently from the battery. Since the power density of the battery is

quite poor in general, it cannot supply sufficient power to the motor during sudden power demands. Besides, as discussed before, a BDC needs to regulate the demand for power either by boosting or releasing. For optimal performance, the voltage of BDC needs to be regulated by using a suitable controller to maintain a smooth step up or step down according to the demand. It is also required to track the continuous load demand, ensuring fast energy dissipation from the designated ESSs and tackling model uncertainty which may arise due to the variable switching frequency and power demands from the motor.

Ensuring a good State of Charge (SOC) and State of Health (SOH) of an ESS is also important for BMS, and thus, it must have a controller that will be able to deal with the nonlinearity of the BDC. The nonlinearity issues of BDCs have been discussed in the literature (Ebad & Song, 2012; Stramosk & Pagano, 2013; Xu et al., 2020). As a result, a suitable control algorithm should be introduced. Nonlinear controllers such as Sliding Mode Control often produce a chattering problem. As for MPC, the algorithm may require more computational time, while the Backstepping controller suffers from over-parameterization, making the design more complex. Considering these facts, this work proposes a Model Reference Adaptive Control (MRAC) algorithm that has been identified as a suitable candidate to tackle the problem that has not been applied before for EV applications. Since this is the first time DMRAC is used in BDC, a proper design, performance analysis, and tuning procedure may become a worthy contribution to this work.

1.3 RESEARCH OBJECTIVES

1. To design an adaptive controller for a simple BDC supplying a constant and variable battery pack voltage for satisfying the three driving modes in EV namely acceleration, cruising, and braking.
2. To evaluate the controller performance based on the standard index such as control effort and tracking error.
3. To analyze the performance of an adaptive controller with the BDC for a Hybrid Energy Storage System where the current supply is switched between battery pack and supercapacitor.
4. To validate the adaptive controller performance by analyzing its power and current tracking accuracy according to the demand from an electric vehicle longitudinal dynamic model based on different drive cycles.

1.4 RESEARCH HYPOTHESIS

In general, Battery Management System (BMS) fulfils the load demands that come from the motor by regulating a certain amount of supplied voltage. Li-ion battery supplies power with constant current (Zhang, 2018) maintaining a constant C-rate. The C-rate is a measure of the rate at which a battery is charged or discharged relative to its maximum capacity. In acceleration mode, the motor demands more power from the battery, and to fulfil the demand, the battery needs to change the C-rate immediately. Ironically, it is not possible for a Li-ion battery to jump from a lower to a higher C-rate in order to fulfil the demand and in general, it takes more than 6 min to discharge with 120 A (Burke & Miller, 2011).

To solve the problem, a secondary power source is required that has higher power density and fast charge-discharge capacity to fulfill the demand. In this study, hybrid ESS has been considered where Li-ion battery is the primary source that can maintain a constant C-rate, and SC plays the role of the secondary source that can offer the additional power demand after Li-ion battery. It is worth mentioning that SC has the ability to discharge by 0.3-30 seconds with nearly 95% efficiency based on the requirements (Douglas & Pillay, 2005). In this work, a Li-ion battery and an SC are connected with two separate BDCs in series to extract current or voltage. This extracted current or voltage is regulated according to the demand from the motor, and thus, two separate controllers have been considered to regulate the current or voltage separately. The DC link will deliver the regulated power from SC and battery to a DC-AC converter (also known as inverter) that supplies the AC current to the motor.

Figure 1.5 demonstrates the proposed drivetrain configuration that explains how the battery and SC are connected with the DC link in parallel and supply power to the inverter.

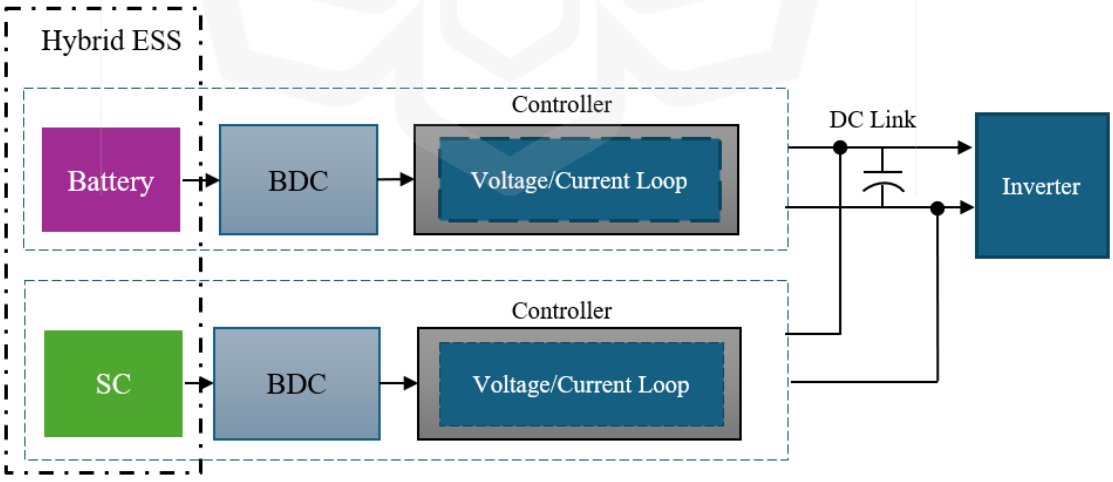

Figure 1.6 A block diagram of the proposed drivetrain configuration.

In the meantime, there is a possibility of a fluctuation of voltage or current demand during the fulfilment of the demand of the motor and the transfer of power because of sudden energy dissipation. The fluctuation and delay of voltage may destroy or prompt dysfunction of any electrical equipment in an EV, and that's why MRAC is proposed to ensure the smooth flow and delay-free voltage to the load through online tuning. In addition, since nonlinearity can disturb the system and the BDC needs to meet the demand of the motor, it is expected that the MRAC model can also handle these issues. Here, the MRAC model works with the supercapacitor loop since the battery power is delimited by the Battery Management System (BMS). To ensure the safety of the battery health, an additional PI controller has been considered with the BDC that is responsible for battery output, while the power extracted from the supercapacitor is controlled by a nonlinear MRAC controller since the motor demand is always fluctuating.

1.5 CONTRIBUTION

The contribution from this study as follows:

1. Design and implementation of a Model Reference Adaptive Control (MRAC) for Bidirectional DC-DC Converters (BDC), capable of regulating voltage under varying EV driving conditions (acceleration, cruising, braking).
2. Improvement in the stability and adaptability of the BDC system compared to traditional control methods such as PI controllers.
3. Development of a power management system (PMS) for switching between battery and supercapacitor, ensuring a smooth power supply during acceleration, cruising, and regenerative braking.

4. Evaluation of the adaptive control strategy in a simulated EV environment using multiple drive cycles (i.e., HWFET, FTP, UDDS, US06) to demonstrate the controller's effectiveness under different real-world driving conditions.

1.6 SCOPE AND LIMITATIONS OF THE STUDY

This study significantly focuses on adaptive controllers for the BDC of EVs. The controller is required to deal with the voltage or current demand that fluctuates with respect to driving modes. The novelty of this work is the consideration of adaptive controller and, more specifically, MRAC for BDC in EV. It would be challenging to know the characteristics of an adaptive controller on BDC and its performance at different voltage or current demands based on some benchmarks since previous works on the adaptive controllers for BDC specifically on this application, are not available (Brando et al., 2018; Nazir et al., 2020; Yanarates & Zhou, 2022).

The work proposes model-based adaptive controllers with two different sources for a BDC that will deal with model infidelity, model uncertainty, ripple reduction and varying gain. However, this work will not involve BMS features and will focus only on the output performance that will be linked to BDC through controllers. Apart from that, this work considers a system that is offered by MATLAB (Mathworks, 2022) as a benchmark model since this system goes through experimental work. Hence, the performance of MRAC is compared with the existing controller in the model.

1.7 THESIS OUTLINE

This study will proceed according to its objectives, which are detailed across this chapters. The Introduction outlines the future growth of electric vehicles, their working principles, and the significance of BDCs and their controllers in the automotive industry. It also includes the motivation and problem statement, objectives, methodology, research scope, and limitations. The Literature Review offers a comprehensive study of available ESSs, BDCs, and their controllers, comparing different ESSs and controllers to demonstrate the strength of the proposed controller. The Methodology chapter explains how the work will progress step-by-step towards the objectives, detailing the BDC topology and model, HESS configuration, and controller design. It also introduces a validation model with detailed parameters to verify the research. The Results and Validation chapter presents the outcomes from the designed models, focusing on the performance and evaluations of the controllers with different models. It also discusses the validation results obtained from simulations performed in the MATLAB/Simulink environment. The Conclusion chapter summarizes the research, highlighting achievements and contributions. It recommends steps for future improvements and suggests related future work.

CHAPTER TWO

LITERATURE REVIEW

2.1 INTRODUCTION

Due to the surge in the demand for EVs, the development and improvement of ESSs have become pivotal as they store and supply the energy needed for propulsion. This improvement includes regenerative braking, which captures energy during deceleration to extend the driving range, and energy management within the vehicle, which can ensure optimal performance and efficiency. As the core component of an EV's powertrain, ESS directly impacts vehicle range, performance, and sustainability, making them essential for the advancement and adoption of electric transportation. Besides, another important component in the EV drivetrain, such as BDC, is crucial for managing energy flow between the battery and other components, such as the motor and the ESS. They enable efficient energy transfer and support regenerative braking, allowing energy to be recaptured and stored during braking. These converters also help stabilize voltage levels, ensuring optimal performance and efficiency of the vehicle. Additionally, they facilitate vehicle-to-grid (V2G) capabilities, allowing EVs to supply power back to the grid, thereby enhancing energy flexibility and contributing to grid stability. This versatility makes bidirectional DC-DC converters essential for modern EVs.

In addition, integrating a control system with a BDC in an EV is important for optimizing energy management and enhancing performance. This integration enables precise regulation of power flow between the ESS and the electric motor, ensuring efficient energy use during driving and charging especially. It also allows for seamless transitions

between charging and discharging modes, maintaining battery health and extending its lifespan. Additionally, the control system ensures voltage stability, protects against overvoltage and under-voltage conditions, and improves the overall reliability and safety of the EV's powertrain system. However, each controller has its own advantages and disadvantages during their operations. Hence, this chapter is dedicated to outlining the available ESSs, and BDCs that are commonly used for EV drivetrain. In addition, commonly considered controllers in this application, including their pros and cons, have also been reviewed in this chapter.

2.2 ENERGY STORAGE SYSTEMS (ESSS) FOR EV

Studying literature review specifically on ESSs for EV can guide to choose a suitable ESS for this research work. In general, there are several types of ESSs for EV such as primary, auxiliary and hybrid ESS. The primary ESSs describes the type of ESSs that play the role as a main source of power in an EV, while auxiliary ESSs only assist the main source to boost up the power in EV. Interestingly, it is noted that primary ESSs do not always require auxiliary ESSs. However, to improve the performance of ESSs, hybrid ESSs have been introduced to accommodate both the primary and auxiliary ESSs. It is utilized not only to improve the performance of ESSs but also to enhance their lives. Figure 2.1. describes the classification and types of ESSs according to their usage.

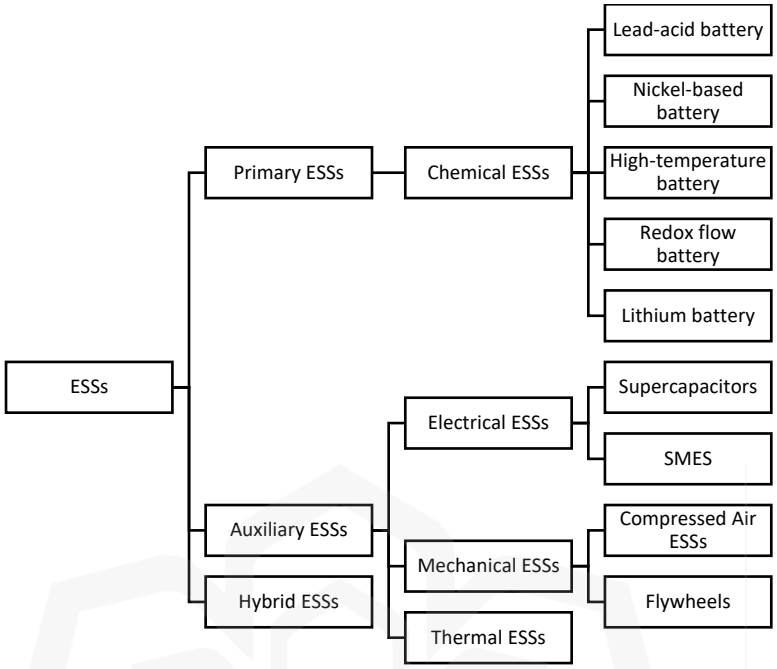

Figure 2.1 Classification of ESSs for electric vehicle.

2.2.1 Chemical ESSs

Chemical ESSs cover a wide range of batteries that includes chemical, electromechanical, flow batteries and fuel cells (Bindra & Revankar, 2018). This section will cover almost all these areas in brief.

2.2.1.1 Lead-acid battery

Lead-acid batteries are mostly popular among IC engine-powered vehicles because of their high availability in the market, are comparatively quite cost-effective and do not generate heat (Khaligh & Li, 2010). In general, these batteries last with a 2000-4500 cycle life of 6-15 years. The power density varies from 200 to 400 W/kg, efficiency is between 70-90% and operational temperature ranges between -20ºC to 60ºC of the batteries. For HEVs, VRLA (valva-regulated lead acid) batteries are highly used because of their fast charging

ability, low initial cost, high specific power and very insignificant maintenance cost (Hoque et al., 2017).

2.2.1.2 Nickel-based battery

Nickel-based batteries include Ni-Cd and Ni-MH, which have created significant demand for EVs. They offer high energy density that ranges from 50-80 Wh/kg and have 2000-3000 discharge life cycle without any damage (Z. Zhou et al., 2013). In addition, the efficiency of Ni-MH and Ni-Cd batteries ranges from 75-85%. The operational temperature of Ni-MH is -40º to 50ºC. Ni-MH has insignificant memory and environmental effects, while Ni-Cd offers high memory and environmental effects (Chau et al., 1999; David & Thomas, 2001; Khaligh & Li, 2010; Rashid, 2017). Notably, Ni-Cd is quite expensive, Ni-Zn offers a poor life cycle, and Ni-MH offers complexity in control and generates heat during operation (Hoque et al., 2017; Khaligh & Li, 2010). On the other hand, Ni-H_2 has become popular for aerial vehicle applications because of its remarkable lifecycle, withstanding ability during overcharging and over-discharging and higher capacity rate. However, it is expensive, has low energy density and offers a self-discharge problem (David & Thomas, 2001; Hoque et al., 2017).

2.2.1.3 High-temperature Battery

Sodium-Nickel Chloride (NaNiCl), also known as ZEBRA, is one of the suitable choices for EVs (Chan & Wong, 2004). It is economically effective and can tolerate more than 1000 cycles with insignificant degradation (Dixon et al., 2009). The specific energy is 350 Wh/kg (G. Li et al., 2016), which is significantly higher than high-capacity batteries like Li-ion. However, it is not recommended for specific power as it offers 400 W/kg, which is almost one-third of a Li-ion battery (Dixon et al., 2009). In addition, its operational

temperature is between 190ºC and 280ºC to achieve its most efficient performance. However, the operational temperature is the main hindrance that stops it from being demandable in the market (G. Li et al., 2016).

The second type of high-temperature battery for application in the EV industry is Sodium-Sulfur (Na-S), which was introduced in the late 1960s in China (Wen et al., 2013). The operational voltage of this battery is 2V (Chung et al., 2004) with more than 2500 life cycles, which is approximately 15 years of life (Kamibayashi & Tanaka, 2001). It has a high energy density of 355 Wh/L and a specific energy of 170 Wh/kg at a C-5 rate (Linden & Reddy, 2002). Its specific power is 250 W/kg, and takes 5 to 6 hours to be recharged (Linden & Reddy, 2002). However, its operational temperature ranges is from 300ºC to 360ºC (Chung et al., 2004) that is higher than the NaNiCl battery's operational temperature. Similar to Na-S, other Na-metal halide batteries are constructed in the way of the tubular beta-alumina membrane. As a result, their operational temperature is nearly 300ºC and offer a slightly higher voltage that is around 2.5V (Bindra & Revankar, 2018).

2.2.1.4 Redox Flow Battery

The heavy study on Zinc Bromine Flow Battery (ZBFB) started at the beginning of the 1970s, though the attention on this battery is not as significant as it was (Putt, 1979). Several reasons can be addressed for the declination of attention on this battery, such as electrical shortening because of dendrite formation on the electrode and corrosion of the electrode and battery casing (Rajarathnam & Vassallo, 2016). Apart from that, it has a relatively short battery life cycle and has the potential to be discharged if it is stored for a prolonged period (Weber et al., 2011). Its operational temperature is 20ºC to 50ºC (Linden & Reddy, 2002),

specific energy is 60 to 85 Wh/kg (Rajarathnam & Vassallo, 2016), energy efficiency is 71% (Lex & Matthews, 1992), and power density is 90 to 100 W/kg (Malachesky et al., 1982). However, it has some advantages for example, it is cost-effective, operational at room temperature (Lex & Matthews, 1992) and flexible to design and manufacture because of the availability of materials (David & Thomas, 2001). Moreover, researchers show that its life cycle can be improved up to 3000 cycles if specific modification can be performed in the electrode (Richards et al., 1990).

Fuel cell is another type of Redox Flow Battery and has become one of the emerging power sources for EVs to proceed with the target of decarbonized transportation. For the first time, it was introduced by Toyota, Hyundai and Daimler in 2013-14, using polymer electrolyte membrane (PEM) fuel cells. The main advantage of this fuel is that it can offer long driving ranges (more than 500km) and fast refuelling (3-5 minutes to refuel) (Cano et al., 2018). Despite providing such facilities, the popularity of fuel cells is a fraction of the popularity of battery (Carsalesbase, 2018) because of some challenges, such as significantly higher prices of fuel, higher payload, etc. (Khaligh & Li, 2010). However, some works on the hybridization of fuel cells with battery are available in order to enhance the efficiency, and it is also expected that plugin hybrid fuel cell power through power shifting between a battery and fuel cell can achieve greater reliability (Mercedes-Benz, 2016).

2.2.1.5 Lithium Battery

Lithium batteries have achieved great popularity among consumers and are promisingly advancing in the EV market. It has a high specific power density of 500-2000 W/kg and an energy density of 90-190 Wh/kg (Hadjipaschalis et al., 2009). Moreover, it includes some

other advantages like low discharge rate, low memory effect, higher efficiency and recyclable (Khaligh & Li, 2010; Z. Zhou et al., 2013) and these result to consider it as a suitable ESS candidate for upcoming EVs (Khaligh & Li, 2010). Lithium-ion and lithium polymer require -20º to 60ºC. Notwithstanding, this battery is expensive and requires a battery management system in order to ensure safe operation and enhance cell life (Khaligh & Li, 2010).

Besides, there are some other types of batteries available in the market that are also applicable for EVs, such as Zinc-Halogen, Metal-air (i.e. Fe, Al, Li and Zn as anodes with inexhaustible air as cathode) (David & Thomas, 2001; Li et al., 2013), Sodium-Sulphur (Chau et al., 1999; Yang et al., 2011), Sodium-Metal Chloride (Chau et al., 1999; Yang et al., 2011) etc. Significantly, lithium batteries are quite popular for EVs compared to other batteries because of their promising performance in terms of high power density, specific energy density, operational temperature, life cycle, efficiency and durability, though they require a proper battery management system for proper operation (Umair Ali et al., 2018).

Table 2.1 provides a comprehensive comparison of several battery types used in ESS, evaluating them on key parameters such as energy density, power density, nominal voltage, life cycle, depth of discharge, round trip efficiency, and estimated cost. This analysis highlights the strengths and weaknesses of each battery type, aiding in understanding their suitability for different applications, particularly in EVs. Importantly, each battery type has its unique advantages and limitations, making them suitable for different applications. Lead-acid batteries are cost-effective which is between USD 105-475 per kWh, but their heavy weight, lower energy density, and shorter lifespan make them less ideal for modern EV applications. On the other hand, NaNiCl and NaS batteries offer

higher energy densities and longer lifespans at higher costs compared to lead-acid batteries. NiCd batteries are robust but environmentally challenging, and flow batteries like ZBFB and VRFB are ideal for large-scale storage despite lower efficiency and higher costs. Lithium-ion batteries emerge as the most suitable for EVs due to their superior performance metrics such as energy density, power density, nominal voltage and round-trip efficiency despite their higher price point.

Table 2.1 Properties of several ESS (Ali et al., 2019; Ralon et al., 2017)

Battery Type	Energy Density (Wh/L)	Power Density (W/L)	Nominal Voltage (V)	Life Cycle	Depth of Discharge (%)	Round Trip (%)	Estimated cost (USD/kWh)
Lead-Acid	50-80	10-400	2.0	1500	50	82	105-475
NaNiCl	160-275	150-270	-	3000	100	84	315-488
NaS	140-300	`140-180	2.08	5000	100	80	263-735
NiCd	60-150	80-600	1.3	2500	85	83	-
ZBFB	55-65	1-25	1.8	10000	100	70	525-1680
VRFB	25-33	1-2	1.4	13000	100	70	315-1050
Li-ion	200-400	1500-10000	4.3	10000	95	96	200-1260

2.2.2 Auxiliary Electrical ESSs

2.2.2.1 Supercapacitors

SC is a suitable candidate as an assistive ESS that can be charged faster and discharge also faster to generate acceleration. It is estimated that 75000000 F can be generated from the accumulated work of 30000 SCs, that is significantly very high (Khaligh & Li, 2010).

2.2.2.2 Superconducting magnetic energy storage (SMES)

SMES is a technology that stores energy in DC electricity form and generates a DC magnetic field (Buckles & Hassenzahl, 2000). It is not as popular as other ESSs because

the superconductive material and cooling system are highly expensive (J. Li et al., 2016; Salama & Vokony, 2020). Despite the expense, it is able to overcome some shortcomings of conventional batteries such as short life-cycle, low power density and sensitivity to high discharge current (Ise et al., 2005; Li et al., 2015) and generate instantaneous power (J. Li et al., 2016).

Toyota introduced the Toyota Prius hybrid car that uses both IC engine and SMES together in order to improve the efficiency of the vehicle (Morandi et al., 2011). Recent works depict that SMES has a long life span of nearly 30 years with 97% efficiency (Salama & Vokony, 2020) and its response time is only a few milliseconds (Faisal et al., 2018; Gong et al., 2016). Therefore, in future, with the advancement of technology, SMES has high potential to create a significant demand in ESS market (Expresswire, 2019).

2.2.3 Auxiliary Mechanical ESSs

2.2.3.1 Compressed Air

Compresses Air ESS has been practiced since the 19th century and introduced for the first time in 1840 (Nayak et al., 2013). It was used for trams and locomotives in the cities (Wasbari et al., 2017). In these vehicles, air is highly compressed by an on-board stationary compressor and stored in a storage tank. This stored air is then released slowly to run a pneumatic motor (Papson et al., 2010).

Several researchers study the performance of compressed air ESSs as an alternative option for IC engine vehicles and compare them with gasoline and electric vehicle (Creutzig et al., 2009) from economic, environmental and driving efficiency perspectives

(Papson et al., 2010). As a result, it is found that it is suitable for low-speed and ranged vehicles that are nearly 47 km (Papson et al., 2010). In addition, their performance is worse than gasoline and electric vehicles from the perspective of fuel cost (Creutzig et al., 2009; Wasbari et al., 2017), carbon footprint (Creutzig et al., 2009; Wasbari et al., 2017) and driving range (Papson et al., 2010). Noted that the specific energy and energy density of compressed air at 300 bar is 500J/kg and 200J/kg, respectively (Wasbari et al., 2017). In order to overcome the shortcomings, researchers are paying attention on the hybridization of compressed air with other ESSs, though it is not very progressing because of environmental factors (Wasbari et al., 2017).

2.2.3.2 Flywheel

Flywheels can be considered as one of the suitable secondary power storage for EVs because of advancements in material engineering and power electronics (Liu & Jiang, 2007). It has a comparatively higher efficiency of 90-95%, a higher amount of power generation of 0-50MW (M. Hannan et al., 2017), shorter recharge time, deeper depth of discharge and long life with unlimited charge-discharge cycle (Long & Zhiping, 2008). Therefore, it is mainly hybridized with any primary source (i.e. battery) of a vehicle in order to overcome the shortcomings of the existing power source, such as lower peak current, lower power capacity and life cycle (Dhand & Pullen, 2015). However, the flywheel cannot beat the battery in self-discharge (M. Hannan et al., 2017; Hedlund et al., 2015), energy density, steady output voltage and cost per kWh (Hedlund et al., 2015). Table 2.2 offers a comparison between flywheels, electric double-layered capacitors (EDLC) and Li-ion batteries in terms of their specifications based on the same rated power, 120kW.

Table 2.2 A comparison between flywheels, electric double-layered capacitor (EDLC) and Li-ion battery (Hedlund et al., 2015)

Type	Flywheel system	Li-ion battery	EDLC system
Manufacturer	GKN	A123Systems	Maxwell Bootcamp
Energy capacity	456 Wh	26,400 Wh	647 Wh
Specific energy	8.3 Wh/kg	110 Wh/kg	1.75 Wh/kg
Specific power	2200 W/kg	500 W/kg	320 W/kg
Cycle lifetime	$>10^6$	$\sim10^3$	$\sim10^6$
System weight	55 kg	240 kg	370 kg

Table 2.2 shows the Li-ion battery stands out for its high energy capacity and specific energy, making it suitable for EVs and portable devices. The flywheel system is optimal for high-power applications and durability, with its exceptional specific power (2200 W/kg) and cycle lifetime (more than 10^6), and thus, it beats SC (also known as EDLC) since SC shows lower energy and power density with higher weight.

2.2.4 Auxiliary Thermal ESSs

Thermal energy storage technology is practised in several applications where solar energy is stored in the form of heat and used as a source of electricity. Researchers are looking for the potentiality of thermal ESSs for electric vehicles, especially in fuel cell powered (Arce et al., 2011), and as a result, Phase Change Materials (PCM) are introduced in order to store the thermal energy in order to implement in EVs (Belik et al., 2017; Hawlader et al., 2003; Zhou et al., 2012). In this technology, two different types of heat, namely sensible heat and latent heat (Hasnain, 1998), are stored where sensible heat means the heat that comes from rising any solid or liquid and latent heat is the heat that comes from changing one phase of a material into another phase (Sharma et al., 2009). Noted that this energy cannot be

considered as a primary source of any electric vehicle because the storage energy is not significant to run a vehicle, and that's why it is considered as a secondary source of energy.

2.2.5 Hybrid ESSs

Hybrid ESSs are the integration of primary sources and assistive/secondary sources of energy. These systems are developed to compensate for the fluctuation and intermittent nature of consuming power at the same time (Dinçer & Zamfirescu, 2014). In other words, hybrid ESSs are introduced to overcome the drawbacks of batteries, such as reduced battery life, limited driving range and low power density. In the meantime, hybridization offers some advantages, such as (Vidhya & Balaji, 2019):

- Ensures constant load profile for the battery that enhances the battery life.
- Improves the performance of EV while the individual battery has low power density and SC has low energy density.
- Enhances driving range and power density during acceleration and braking.

Primary sources of energy, in general, offer low power density and high energy density, while assistive sources of energy have the nature of high power and low energy density, as aforementioned. Literature introduces several hybrid ESSs, such as Li-ion batteries with supercapacitors (Mali & Tripathi, 2020; Mesbahi et al., 2020; Song et al., 2018), fuel cell with supercapacitors (Allaoua et al., 2017), Li-ion battery with flywheel (Itani et al., 2016), Li-air battery with SMES (Yang et al., 2020), lead-acid with supercapacitors (Kasprzyk, 2017), Ni-MH battery with fuel cell (Garcia et al., 2009) etc. Among them, lithium-ion battery with supercapacitors is one of the most widely used hybrid ESSs for electric car because lithium-ion offers higher energy density and SC offers

higher power density relatively. Therefore, in this work, as an auxiliary energy source, SC has been considered with the primary source, Li-ion. The advantages and disadvantages are listed as below:

Advantages of lithium-ion battery (Plett, 2015)

- has a higher density than most of the rechargeable batteries.
- can operate comparatively at a high voltage, typically 3.7V, whereas NiMH or NiCd operates around at 1.2V.
- has a lower self-discharge rate compared to other secondary cells.
- can offer long life because of a gentler intercalation process in each electrode.

Disadvantages of lithium-ion battery (Plett, 2015)

- is comparatively more expensive than NiCd and NiMH batteries that have similar capacities.
- is more complex to manufacture.
- requires special safety precautions because of more reactive chemicals.
- is very sensitive to cell construction and cell materials.

On the other hand, SC is another type of ESS that is mainly used for generating power instantly. The basic principle of SC is to store energy by separating negative and positive charges using an insulator. As it does not make any variations chemically in electrodes, it offers a long lifecycle. Its power density is remarkably higher than a battery while it offers very low energy density (Tie & Tan, 2013). Importantly, Table 2.2 demonstrates that flywheels have a higher specific power, specific energy, and cycle

lifetime compared to SC. However, presently available flywheels often suffer from significant losses, impacting their ability to hold a charge. These losses include electrical (hysteresis, eddy current and copper), mechanical (bearing, friction and drag), and those related to power converters (switching and conduction) (Choudhury, 2021). Additionally, flywheels need to be maintained to prevent failures, which could have catastrophic consequences (Li & Palazzolo, 2022). Considering the facts, Li-ion and SC have been proposed as suitable ESSs for EV in this study. Table 2.3 describes the properties of both ESSs and offers a comparative analysis (Nakad et al., 2023).

Li-ion batteries are favoured for their high energy density, reasonable specific power, and cost-effectiveness, making them suitable for EVs, portable electronics, and other energy-dense applications. However, they have limitations in cycle life and specific power. SCs, on the other hand, excel in specific power, cycle life, and temperature tolerance. They are ideal for applications requiring rapid charge and discharge cycles, such as in regenerative braking systems and short-duration energy storage. However, the high cost and low specific energy are the primary drawbacks of supercapacitors. Thus, compromising the cost for SC, a hybrid ESS is proposed where the weakness of the Li-ion battery, especially low specific power, can be replenished by the SC while SC's low specific energy capacity can be recovered by Li-ion battery.

Table 2.3 Properties of Li-ion and Supercapacitor.

Function	Li-ion	Supercapacitor
Cell Voltage	3.6 V	2.3-2.75 V
Specific Energy	120-240 Wh/kg	5 Wh/kg
Specific Power	1,000-3,000 W/kg	~ 10,000 W/kg
Charge Time	10-60 min	1-10 seconds
Cycle Life	500-10,000	30,000 h
Service Life	5-10 years	10-15 years
Cost (per Wh)	$0.5-$1	$20
Charge Temperature	0 to 45^{o}C	-40 to 65^{o}C
Discharge Temperature	-20 to 60^{o}C	-40 to 65^{o}C

2.3 DC-DC CONVERTERS AND THEIR APPLICATIONS

DC-DC converter has some advantages over transformer to perform the same function that draws the attention of the researchers. In general, it is lighter in weight, smaller in size, more cost-effective, comparatively reliable and highly efficient than a transformer (Chakraborty et al., 2017). Apart from that, a DC-DC converter can also be used with a complex BMS that may reduce the number of battery cells in series and, hence, reduce the complexity of BMS (Chakraborty et al., 2019). In addition, a higher voltage DC-DC converter is able to afford higher DC link voltage that enhances the performance of power electronics and electric motors (Lundmark et al., 2013). Noted that during the rushing period, the output of the DC-DC converter can be controlled, which enhances another dimension of the system (Chakraborty et al., 2019). On the other hand, it has some notable drawbacks such as flat voltage gain during moderate gate pulse switching, poor efficiency because of hard-switching, low efficiency in attaining high power density, the challenge in designing robust high bandwidth control loop and power loss during operation (Emadi et

al., 2008; Forouzesh et al., 2017; Kolli et al., 2015). However, these drawbacks can be overcome by adopting new topologies, design concepts or materials.

Switching-mode power supply is extensively used in electric power, household applications, communication, railway, automobile, aviation and industrial devices (Li & He, 2010; Pan & Lai, 2009). Based on the switching mode power supply, buck converter and boost converter have been developed to step-down or step-up voltages. These two converters are simple in structure and offer high efficiency, but their applications are limited because of limited voltage gain (Wu & Chen, 1998). As a solution to high voltage gain, Luo converters have been introduced, though it is also not free from other shortcomings such as topological complexity, volume, cost, and losses growing simultaneously (He & Luo, 2005; Luo, 2001; Luo & Ye, 2004). With low voltage stress, interleaved converters are able to reach high step-up or step-down conversion ratios though their structure, operational mode, and control strategy are sophisticated (Chen et al., 2015; Pan et al., 2013, 2014; L.-w. Zhou et al., 2013). Quadratic converters can offer high voltage gain of cascade converters having comparatively fewer switches. Notwithstanding this fact, the efficiency of quadratic converters is not promising (Morales-Saldana et al., 2014; Ye & Cheng, 2013).

BDC is a type of converter that allows constant energy exchange to form a source to load and vice versa, while earlier, unidirectional converters were not able to offer the functionality of exchanging power or energy in both directions at the same time. In order to ensure optimal exchange of power, features such as wide voltage exchange range, high power density, compactness, low EMI impact, ability to deal with current ripple and high voltage and current stress, and higher conversion efficiency are considered for choosing or

designing a BDC for the HESS of an EV. For instance, given the variety of driving conditions, the BDC converter must have a wide voltage conversion range to effectively match the voltage of the power battery or SC with DC bus voltage under changing conditions. In addition, a higher power density of a BDC can be accommodated within a limited vehicle space, saving installation space (Wang et al., 2022). Alongside, during the design of a BDC, the input and output of the BDC should share a common ground to avoid electromagnetic interference (EMI) caused by high-frequency pulse width modulation (PWM) voltage pulses; otherwise, it can cause sensitive electrical equipment failure in EV (Wu et al., 2021). Moreover, a suitable BDC can contribute to the durability of a battery or SC, eliminating large current ripple (Y. Zhang et al., 2019). The high exchange efficiency of a BDC can reduce heat generation and energy loss caused by device inefficiency (Elsayad et al., 2019).

Considering the safety of electrical devices and wide voltage range, BDCs can be classified mainly into two (2) types such as non-isolated and isolated. An isolated DC-DC converter ensures electrical separation between input and output with the help of a transformer that allows a wide range of voltage conversion with a high safety level. In contrast, a non-isolated DC-DC converter typically accommodates buck or boost circuits and is mostly used for low-voltage range applications (Liu & Wu, 2023). Figure 2.2 demonstrates a commercially used isolated DC-DC converter manufactured by Infineon Technologies (Infineon Technologies, 2024). In general, isolation is important when high gain is required for step-up and step-down. However, non-isolated DC-DC converters are mostly chosen because of some of their advantages over isolated DC-DC converters with design simplicity and cost-effectiveness (Du et al., 2011; Tytelmaier et al., 2016).

Figure 2.2 An isolated bidirectional DC-DC converter.

(Mira et al., 2017) discuss and compare several isolated and non-isolated BDCs extensively considering different specifications such as switching frequency, efficiency, number of switches and gain. (Chakraborty et al., 2019) introduce the commonly used BDCs that are used in electric vehicle powertrains where buck-boost, Cuk, SEPIC, and multi-device/port interleaved (MDIBC) are considered as non-isolated and half-bridge, full-bridge, push-pull, forward, and flyback are included under isolated BDCs. SEPIC and Cuk are suitable BDCs for ESSs where input comes from the battery or SC (Al Hysam et al., 2017; Chakraborty et al., 2015; Pachauri & Chauhan, 2016). In the meantime, (Wang et al., 2022) categorize non-isolated BDCs for HESSs into basic (i.e., boost, SEPIC and Cuk), inductor with inductor (i.e., switched inductor, interleaved and quadratic boost), capacitor with capacitor (i.e., switched capacitor, voltage multiplier, Z source, Quasi Z source, three-level), inductor with capacitor (i.e., voltage lifting circuit) and hybrid along with cascaded and discuss their functionalities along with their advantages and disadvantages.

Table 2.4 compares four types of non-isolated BDCs such as inductor with Inductor, capacitor with capacitor, inductor with capacitor, and hybrid/cascaded, based on their distinct functionalities, design specifications, advantages, and drawbacks. The Inductor +

Inductor converters, in general, improve the voltage conversion ratio by parallel charging and series discharging of the circuit inductors. They allow a wide range of voltage conversion and continuous current and have a feature of common ground, though they require high control precision and numerous switches. The capacitor with capacitor converter enhances the voltage conversion ratio by parallel charging and series discharging capacitors, offering a high voltage conversion ratio at non-extreme duty cycles and a common ground, but it suffers from high voltage stress and discontinuous current. Besides, the inductor with capacitor converters are designed in a structure that enables parallel charging and series discharging of both inductors and capacitors. This formation is suitable for generating new topologies with fewer energy storage devices, but it has complex control and doesn't significantly increase the voltage range.

Lastly, the hybrid/cascaded converter optimizes performance by integrating and cascading different impedance networks, providing a wide voltage range and inheriting the advantages of combined topologies, yet it is burdened by a large number of devices, lower conversion efficiency, and the disadvantages of its sub-topologies. These characteristics make each type suitable for specific applications within hybrid energy storage systems in new energy vehicles, highlighting the importance of choosing the appropriate converter based on the system's needs for voltage conversion range, control complexity, and device count. This comprehensive comparison helps in understanding the trade-offs involved in each topology, aiding in the selection of the most appropriate converter for achieving optimal performance, efficiency, and reliability in electric vehicle powertrains.

Table 2.4 Comparative discussion among non-isolated BDCs of different topologies (Wang et al., 2022).

Converter Type	Functionalities	Design Specifications	Advantages	Disadvantages
Inductor with Inductor	Improves voltage conversion ratio by parallel charging and series discharging of inductors.	Uses two inductors charged in parallel and discharged in series; interleaved design reduces current ripple.	Wide voltage conversion range, easy to control, continuous power source side current, input-output common ground.	High control precision required, large number of switches.
Capacitor with Capacitor	Enhances voltage conversion ratio through parallel charging and series discharging of capacitors.	Employs two capacitors charged in parallel and discharged in series; voltage multiplier and Z-source modifications.	Wide voltage conversion range, input-output common ground, high voltage conversion ratio at non-extreme duty cycle.	High voltage stress on high voltage side, discontinuous power source side current, steep slope of voltage conversion ratio.
Inductor with Capacitor	Increases voltage conversion ratio with combined parallel charging and series discharging of both.	Combines inductors and capacitors for parallel charging and series discharging; H-bridge configurations.	Easy to generate new topologies, input-output common ground, fewer energy storage devices.	Complex control, large number of switches, no significant increase in voltage conversion range.
Hybrid/ Cascaded	Optimizes performance by integrating and cascading different impedance networks.	Combines features of other types to optimize performance; can share devices without violating circuit laws.	Wide voltage conversion range, easy to generate new topologies, inherits advantages of sub-topologies.	Large number of devices, low conversion efficiency, inherits disadvantages of sub-topologies.

In this study, the hybrid/cascaded type has been considered since it is simple to build, offers a wide range of voltage conversion and enables the converter to adopt the advantages of each unit, though the possibility of low efficiency should be compromised. Despite the fact, (Arslan et al., 2021), (Fatah et al., 2012), (Majeed et al., 2020) and (Bai et al., 2019) consider cascaded type converters and evaluate the performance of their systems and controllers, which result in the level of satisfaction.

2.4 BDC CONTROLLERS

The BDC is regulated by a PWM signal to control the vehicle's speed by adjusting the output voltage. The efficiency of this voltage control depends on the performance of a suitable controller. While linear controllers can be effective for BDCs, they often fail to maintain robustness during model uncertainties, load disturbances, parameter variations, and input voltage fluctuations. Consequently, nonlinear and learning-based controllers are also considered (Allaoua & Laoufi, 2011).

Hegazy et al. (2011) explored the use of a PI controller with interleaved BDCs to reduce voltage ripples and ensure DC-link voltage stability. Ramya & Jegathesan (2016) focused on PI and PID controllers with a buck-boost converter in an EV, emphasizing voltage tracking. Their study concluded that using a PI filter effectively reduces voltage ripple and performs better than a PID controller by reducing settling time and steady-state error. Das & UddinChowdhury (2016) compared the performance of PI and PID controllers with a BDC and found that the PI controller performed satisfactorily in boost mode. Pany et al. (2011) used a PI controller with a buck-boost converter to achieve satisfactory performance in an electric vehicle's acceleration mode, steady-state, and regenerative

braking system. H. Zhang et al. (2019) proposed three different BDCs using a double-loop PI controller with an inner current loop and an outer voltage loop to track the required voltage in an EV.

Ciccarelli & Lauria (2010) applied a sliding mode controller (SMC) with a coupled-inductor BDC to improve supercapacitor performance. Albiol-Tendillo et al. (2012) designed and controlled the traction system of an EV, utilizing an SMC with a BDC to ensure fast response, robustness, and voltage regulation. This study demonstrated that SMC can track voltage effectively, even in the presence of disturbances. Purohit et al. (2019) highlighted the advantages of SMC over PI controllers in handling load variations up to 20%, whereas PI controllers showed fluctuations in voltage tracking of the BDC in both buck and boost modes (which will be discussed in detail in chapter 3). This suggests that SMC is suitable for dealing with uncertainties within the BDC's limits. However, chattering (Bartolini et al., 2000; Boiko & Fridman, 2005) and ripple in power converter (Perreault et al., 1999) are the main drawbacks of SMC. Utkin (2013) proposed harmonic cancellation principles to suppress SMC chattering. Lee et al. (2012) employed backstepping with sliding mode control to track voltage demand through the BDC of the EV, addressing the chattering problem of SMC. This work also incorporated two PI controllers for the current loop, aiding in voltage demand tracking, though steady-state error between 20%-25% appeared.

Khan et al. (2018) introduced another nonlinear control algorithm, backstepping sliding mode control, applied to a BDC of hybrid ESSs of Proton Exchange Membrane Fuel Cell (PEMFC) and supercapacitor, achieving fast and promising performance in load variation tracking. Allaoua & Laoufi (2011) proposed a fuzzy sliding mode controller with

a buck-boost BDC, achieving robustness during load current variations without chattering effects and with disturbance-free dynamic characteristics. Poyyamani Sunddararaj et al. (2019) combined PI and fuzzy controllers with a BDC, resulting in reduced ripple, higher voltage gain, and efficiency.

Pirooz & Noroozian (2016) proposed an MPC controller with a BDC to track reference voltage for applications like PV or EV. This simulation successfully tracked the reference and provided a fast response during transitions, though it did not consider disturbances. Akter et al. (2015) used an MPC controller with a bidirectional isolated full-bridge DC-DC converter to control both the reference voltage and current of the inverter, ultimately improving power efficiency to 92.52%. Despite its effectiveness, MPC faces issues with variable switching frequency and current ripples, as noted in the literature (Chan et al., 2017; Karamanakos et al., 2018; Yoo et al., 2019). To address the challenges associated, Zhang et al. (2018) introduced a novel three-level DC/DC converter configuration that enables full and independent regulation of both the battery and SC. Additionally, utilizing three voltage levels helps reduce the inductor size in both the battery and SC branches. However, it begot the reduction of the ratings of power switches and inductors. Liu et al. (2014) proposed an explicit model predictive control for BDCs with supercapacitors in electric trains, maintaining duty cycle constraints and reducing online computational complexity. Another study on hybrid ESSs proposed an integral backstepping controller with a buck-boost BDC, ensuring steady-state error and meeting vehicle load demands (Khan et al., 2019).

Bai et al. (2019) designed an H-infinity controller with a supercapacitor to track output current under load conditions, experimentally validating its robustness and tracking

performance. Mendoza-Torres et al. (2019) introduced a switching control strategy for BDC current control in EVs, based on hysteresis and logic switching. This strategy handles parametric uncertainty in the inductor up to 20% but suffers from variable switching frequency, leading to inconsistent harmonic content.

2.5 ADAPTIVE CONTROLLER AND ITS APPLICATION

As adaptive controller is considered as a suitable controller based upon an extensive study on literature, the pros and cons can be highlighted that may guide to a suitable conclusion for the controller selection. Adaptive controller offers a mechanism of parametric adjustability to control a system. Structurally this nonlinear controller includes two loops where one is used for normal feedback process and another one is used for parameter adjustment (Åström & Wittenmark, 2013).

Historically, adaptive controller emerged for the first time in the history in order to improve the performance of an aircraft in NASA X-15 Hypersonic Research Program in late 1950's (Åström, 1983; Walker & Weil, 1963). It was noticed that fixed gain controllers and gain-scheduling algorithm cannot ensure the required performance of X-15 hypersonic aircraft as dynamics vary with flight condition drastically (Adkins & Taylor Jr, 1964). Therefore, a newly invented adaptive flight controller, Honeywell MH-96 was implemented on NASA X-15-3 aircraft in 1961 to investigate the performance (Boskovich & Kaufmann, 1966). Moreover, between 1961 and 1967, this model-following adaptive variable gain controller was used in 65 hypersonic flights. The investigation concluded that this controller did not require prior knowledge of aircraft aerodynamics, could adapt to changes in aircraft configurations, and ensured consistent responses under all flight

conditions (Dennehy et al., 2014; Dydek et al., 2010; Holleman, 1966; Sheet, 2014). However, the crash of a Honeywell MH-96 aircraft in 1967 was attributed to a lack of understanding of adaptive controller theory and mechanisms (Dydek et al., 2008). Consequently, extensive research on adaptive controllers was conducted from the late 1960s to the 1970s. This research, documented in several publications, ultimately identified the root cause of adaptive controller instability as incorrect control gain choices (Erzberger, 1967; Landau, 1969).

In the meantime, the Lyapunov stability theory's emergence came as a blessing for overcoming the drawback of the adaptive controllers (Lyapunov, 1992; Monopoli, 1967; Parks, 1966). As a result, Honeywell MH-96 was modified according to Lyapunov stability theory, and finally, it was found that the new controller could obtain high performance and showed robustness in the presence of model uncertainty (Dydek, 2010). Since the early 1980s, researchers tried to improve its robustness more to deal with high control gains, noise and disturbances, and unmodelled dynamics that are responsible for system instability. As a consequence, robustification methods such as e-modification (Narendra & Annaswamy, 1987), dead-zone method (Peterson & Narendra, 1982), σ-modification (Ioannou & PV, 1983), parameter projection method (Goodwin & Mayne, 1987) were formulated in different literatures.

Apart from the aerospace industry, adaptive control algorithms have also gained popularity in power electronics. A type of adaptive control, Model Reference Adaptive control (MRAC), has several applications with power converters. This controller considers a pre-designed model and a reference model to define the required dynamics of the system and follows an adaptation process (Åström & Wittenmark, 2013). It has achieved interest

among the researchers as the performance of the system can be pre-defined through a reference model. Literature introduces multifarious applications of MRAC in power electronics. Ardhenta & Subroto (2020) have chosen Direct MRAC to control the voltage input to the DC-DC boost converter with the help of the PI controller. In this study have achieved a stable response and short period of settling time, rise time and overshoot during operation. Shyu et al. (2008) have chosen MRAC for single-phase shunt active power with a view to reducing line current harmonics and improving line power factor. This study significantly mentioned choosing MRAC as its adaptability, flexibility, and robustness surpasses the PI controller, and its self-tuning features ensure the stability of the system. Djebbri et al. (2018) have applied fractional order MRAC on a system that accommodates two power sources, a zero voltage switch full-bridge isolated DC-DC buck converter and a resistive load so that the controller can stabilize the current and voltage of the DC-DC converter that is coupled with the DC bus link. The proposed controller surprisingly offers a fast dynamic response in DC bus voltage and robustness to voltage variation on both load and input. Despite some applications of MRAC in power electronics, as aforementioned, the literature lacks the application of MRAC with a HESS of batter and SC in a cascaded configuration of non-isolated BDC. Hence, in this research work, MRAC has been proposed as a suitable controller choice because system stability and fast response with continuous variation of load demand and switching the buck mode to boost mode and vice-versa in BDCs are the primary concerns of this work.

2.6 COMPARISON AMONG DIFFERENT CONTROLLERS FOR BDCS

This section concentrates on an analysis of commonly used controllers like PID, LQR, SMC, Feedback Linearization, Backstepping and MPC based on their functional

advantages and disadvantages. The classical PID controller is only applied with a linear model. This controller gives the opportunity to design the controller according to the desired model performance. However, it becomes more challenging to design a well-performed PID controller when the model is nonlinear because the gain cannot be chosen in any systematic way that a classical PID controller requires. In addition, LQR also requires a linear model to get a properly controlled system, and it can handle multiple inputs and outputs at the same time, unlike the PID controller. The main drawback compared to PID is that sometimes it shows a steady-state error because it does not offer any integral part (Argentim, 2013).

The primary advantage of feedback linearization is its systematic framework for modelling a controller. This controller performs well when the difference between linear and nonlinear models is minimal. However, it falls short of providing a satisfactory response in the presence of model uncertainties and does not effectively handle constraints. Consequently, the robustness of this controller is not always reliable (Kurtz & Henson, 1998; Pop & Dulf, 2011; Zulu & John, 2016).

Backstepping is one of the most chosen nonlinear control techniques that require a systematic procedure and follows a recursive design methodology. It can cancel out the nonlinear terms in the system, and as a result, it does not require precisely designed models, unlike feedback linearization. It has the capability to overcome mismatched perturbations and can attain stability asymptotically. However, the main drawback of this controller is over-parameterization, which implies it needs many parameters to give a satisfactory performance to the system It sometimes becomes very difficult to find out all the parameters accurately (Basri et al., 2014; Chung & Chang; Huo et al., 2014).

The sliding mode control (SMC) technique has garnered significant attention for designing robust controllers in systems with high-order nonlinearity and uncertainties. SMC is less sensitive to disturbances and parametric uncertainties, ensuring system robustness. However, it presents a chattering problem due to the continuous switching of the controlled model. This issue can lead to energy loss, unmodeled dynamics, and occasionally system instability, which can be hazardous (Bendaas & Naceri, 2013; Levant, 2007; Runcharoon & Srichatrapimuk, 2013; Shtessel et al., 2014)

MPC has been used in different processes of chemical industries and refineries for more than three decades. Currently, researchers show great interest in applying it in all types of complex controlling systems because of its versatile capabilities like dealing with noise and disturbances and input and output constraints at the same time (Bouffard, 2012). Nevertheless, the computation burden is too heavy, and it needs to do internal calculations for optimizing the control input at each time step.

In general, MRAC is renowned specifically for dealing with a plant with unknown parameters when a system identification tool is required to predict the parameters online (Yechiel & Guterman, 2017). It maintains a predefined control law and makes the system to follow a predefined reference model (Kersting & Buss, 2017). The main advantage of this nonlinear controller is its simplicity and straightforward implementation. Apart from that, it is easy to design the control law for MRAC that can estimate the system's parameters. However, it also requires a suitable understanding of the dynamics of the system, and that can be considered the main drawback of MRAC (Yechiel & Guterman, 2017). In addition, MRAC with the Lyapunov approach sometimes requires higher values of adaptation gains in some applications as controlling inverse pendulum (Pawar & Parvat,

2015) that leads to oscillations, and it may cause instability in the system (Bierling, 2014). Table 2.5 summarizes the advantages and disadvantages of each control algorithm that have been discussed.

Table 2.5 A comparison of different controllers (Roy, Islam, Sadman, et al., 2021).

Controllers	Advantages	Disadvantages
PID	Easy to choose gain; can overcome the steady-state error.	Cannot handle constraints, noise and disturbance; cannot deal with multiple inputs and outputs at the same time.
LQR	Can deal with multiple inputs and outputs	Sometimes fails to overcome steady-state error due to model discrepancy, absence of an integral unit or non-zero setpoint model.
Feedback Linearization	Systematic model framework; well-performed when linear and nonlinear models are almost similar	Incapability of constraints handling and model uncertainties, poor robustness
Backstepping	Systematic and recursive designed; precisely designed model is not required; can handle nonlinearities to the system; can overcome mismatched perturbations and ensures stability.	Over-parameterization; difficult to choose proper parameters
SMC	Well-performed in high-nonlinearity; less sensitivity in disturbances and model uncertainties.	Chattering problems sometimes create system instability.
MPC	Predicts future behaviour of the states; deals with multiple inputs and outputs at the same time; can handle constraints at inputs and outputs; can overcome noise and disturbances	Slow in tracking
Adaptive Control	Easy to design a control law, predict unknown parameters	Sometimes slow in response, offers oscillations and improves slowly

2.7 SUMMARY

With the evolution of vehicles in automobile industry from IC powered vehicles to EVs, researchers are focusing on the ESS extensively. As a result, chemical batteries, SCs, fuel cells, flywheels and engine generators appear in the literature. Remarkably, two factors such as how fast an ESS can give power and how much it can store energy are considered to design an ESS. Therefore, hybridization of ESSs is a timely solution that have been considered in literatures to match all the requirements of a vehicles (Ostadi et al., 2013). It is found out that the combination of Li-ion battery and supercapacitor may provide a good combination. Nevertheless, there is a gap to propose a suitable controller to regulate the voltage via BDC converter to ensure a smooth power supply between primary and auxiliary sources.

Improper controller may cause to worsen the performance of these converters. For example, a commonly used controller, PID cannot deal with uncertainty in a system. Being a nonlinear controller, Sliding Mode Controllers are normally able to tackle system nonlinearity but often show chattering problem. Feedback linearization in general can deal with system nonlinearity, yet model parameterization is another challenging task. It seems that based on the survey, the MRAC can be considered as a potential candidate to control this system. Thus, further investigation on this algorithm specifically for BDC is another gap to be filled in for this work. The contributions may come from the design process, derivation of control algorithm, tuning process and analysis of the result with the benchmark system.

CHAPTER THREE

METHODOLOGY

3.1 INTRODUCTION

This chapter presents the methodology that has been taken to achieve the three main objectives by incorporating the design and modelling work specifically based on provided hypothesis. To ensure the BDC performs effectively, consistently, and safely, designing a controller for a power converter entails several important processes. A few steps outlining the processes needed to develop a controller for a BDC is provided below:

1. **Design requirements:** Based on the literature review, lithium-ion battery and supercapacitor should be the best energy storage system. Hence, a suitable BDC should be considered in the first place in details that will be responsible for transferring the power to the DC bus, which directly deals with the motor. The design requirement covers the voltage/current needs for the input and output, response times, and any other pertinent factors.
2. **Suitable converter topology:** Based on the needs of the system, a suitable power converter topology that best matches this application, such as buck, boost or buck-boost, should be considered.
3. **Model design:** Using circuit equations and control theory, a mathematical model or simulation of the power converter system, including all of its parts (switches, inductors, capacitors, etc.), should be considered. To comprehend the converter's dynamics, stability, and transient responsiveness, disturbance can be considered with input signals to the system.

4. **Controller design:** Depending on the topology and performance expectations of the converter, a suitable control technique should be considered and in this study, MRAC approach has been considered as the promising option. Its efficiency should be evaluated from multiple aspects that includes voltage-mode control and current-mode control.
5. **Simulation:** To test the developed controller's performance under various operating settings and load changes, it should be simulated in MATLAB/Simulink. Hence, multiple simulation models can be considered to evaluate the performance of the controller. Initially, a model with only a battery can be considered where the controller with BDC is responsible for voltage regulation. Then, a HESS that includes both battery and supercapacitor, with a BDC, can offer a better understanding of how the controller is performing. Here, the controller may control the power by controlling the current in the system. Thus, the performance of the controller can be analyzed from two different scenarios.
6. **Validation:** Finally, to validate the controller's performance from a real-time aspect, a complete EV model with a HESS should be adopted that can represent a real-time model. Based on the simulation results of the validation model, a real-time model experience can be achieved.

Noted that the control input and output from the system, with a response nature, vary from model to model.

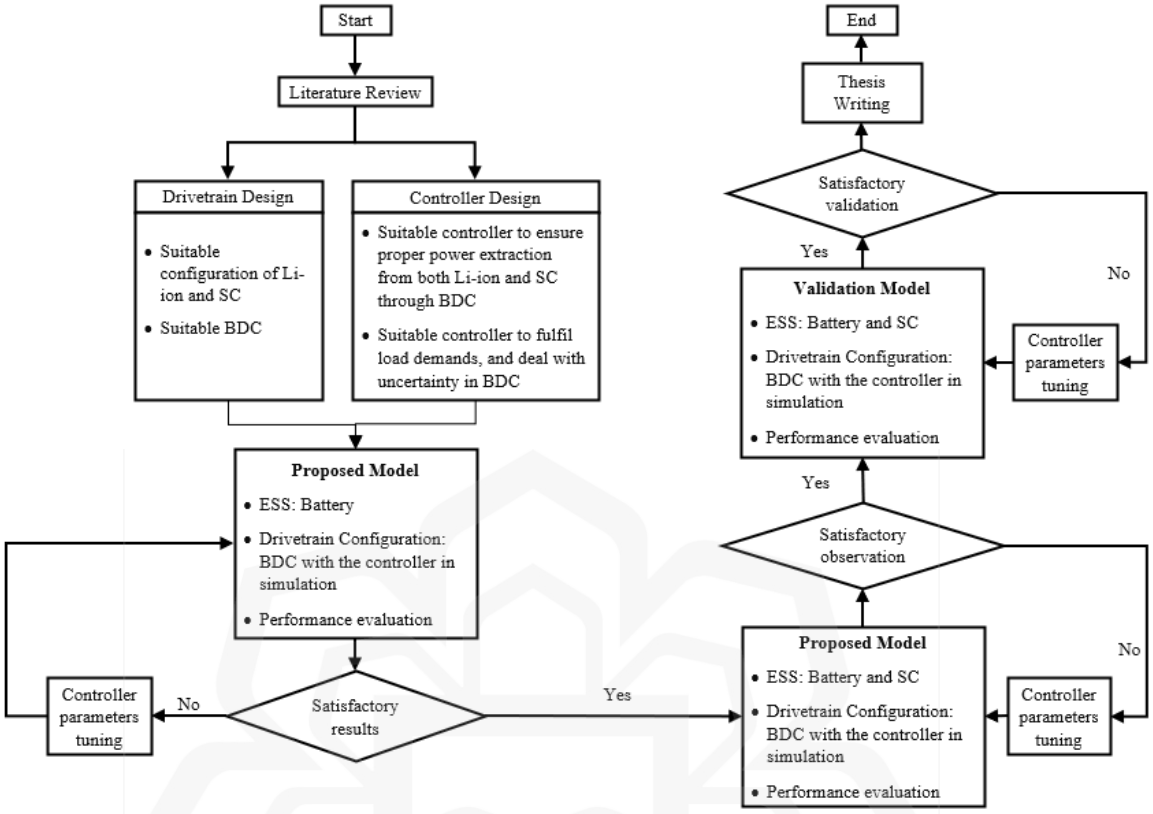

Figure 3.1 A flow chart of methodology.

Based on the objectives, this chapter highlights the working principle of DC-DC converter, buck-boost converter topologies, state-space model derivation, BDC design and adaptive controller design for BDC as parts of the methodology. The overall flow chart for the methodology is presented in Figure 3.1. Importantly, the methodology significantly depends on the obtained result as the unsuccessful or unexpected result may lead to modification of the methodology specifically for the BDC design and controller design. To avoid this uncertainty of design parameters, this work considers some of the existing BDC design models discussed in the literature. Since controller performance with the BDC is crucial, it can also be validated based on the controller's performance in previous works (Modabbernia et al., 2013; Utomo et al., 2011; Zhou & He, 2015). Based on that, a

controller computation time should be less than 1s, overshoot should be less than 5% and rise time and settling time should be less than 1s in a BDC in general. Nevertheless, the MRAC model for BDC is not found in the literature, and thus, other controllers' performance for BDC can be considered as the benchmarked performance for the proposed controller. In the future, successful achievement of the controller performance can lead towards hardware implementation. It is worth mentioning that MRAC may not reach the expectation with BDC and in that case, the sensitivity of this controller with BDC should be investigated extensively.

3.2 BUCK-BOOST CONVERTER TOPOLOGIES

In general, the buck-boost converter is responsible for producing an output voltage that can provide more or less voltage than the input. It follows the switching mode power supply through the combination of buck and boost converters principles in a single circuit. Interestingly, two different modes are found for buck-boost operation, such as inverting and non-inverting, where the choice depends on a specific application.

3.2.1 Inverting buck-boost converter

An inverting buck-boost converter offers negative output voltage with respect to the ground. It basically consists of a Metal-Oxide-Semiconductor Field-Effect Transistor (MOSFET), inductor, capacitor, diode, power source and a load that is shown in Figure 3.2.

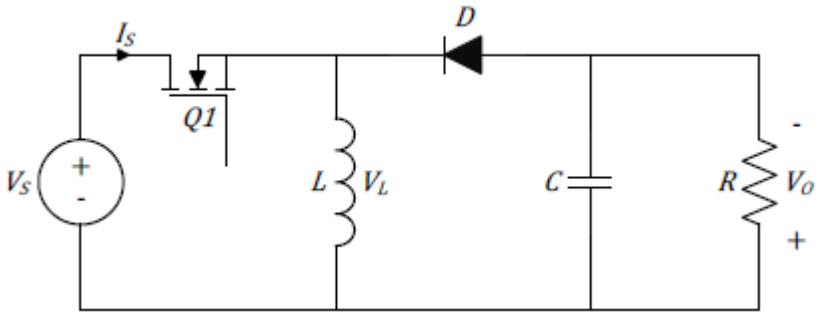

Figure 3.2 Inverting buck-boost converter (Kabala, 2017).

During on-state, as shown in Figure 3.3, the current rise up proportionally with a constant rate to input voltage. Hence, energy rises up in the inductor during on-state. On the other side, the capacitor supplies current to load. However, the voltage along the inductor will be:

$$V_s = V_L \tag{3.1}$$

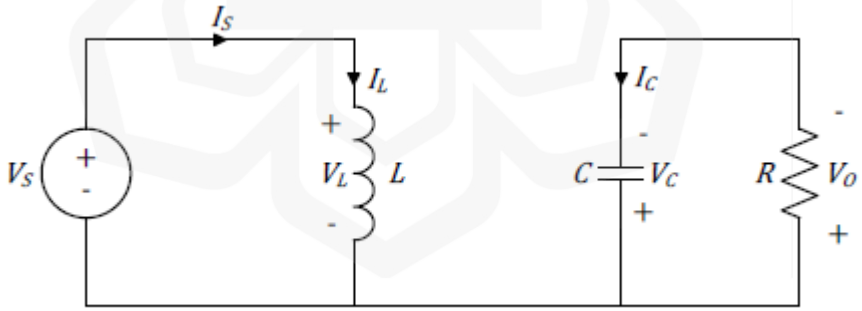

Figure 3.3 Inverting buck-boost converter (On-state) (Kabala, 2017)

Hence, when duty cycle and switching period are denoted by D and T, the current along the inductor can be formulated as:

$$V_L = L\left(\frac{dI_L}{dt}\right)$$

$$\Delta I_{L_{(on)}} = \int_0^{t_{on}} \frac{V_L}{L} dt$$

$$\Delta I_{L_{(on)}} = \left(\frac{V_s}{L}\right) DT \tag{3.2}$$

where, $t_{on} = DT$.

For off-state, as shown in Figure 3.4, the diode can play a role as a forward-biased diode, and hence, the current along the inductor drops down at a constant rate in proportion to V_o. In this state, energy moves from the inductor to the capacitor and output load. Therefore, the voltage across the inductor will be:

$$V_o = V_L \tag{3.3}$$

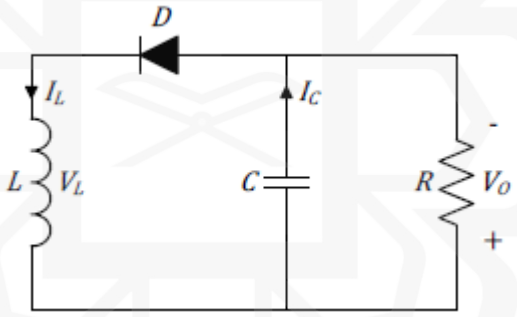

Figure 3.4 Inverting buck-boost converter (Off-state) (Kabala, 2017).

As a result, the current can be calculated as:

$$V_L = L\left(\frac{dI_L}{dt}\right)$$

$$\Delta I_{L_{(off)}} = \int_{t_{on}}^{t_{on+off}} \frac{V_L}{L} dt$$

$$\Delta I_{L_{(off)}} = \left(\frac{V_o}{L}\right)(1 - D)T \tag{3.4}$$

where, $t_{off} = (1 - D)T$.

In a steady-state condition, the inductor current and capacitor voltage repeat their values every switching cycle, and their average values have no further changes. Mathematically, the average voltage across the inductor over one period must be zero to ensure that the current returns to its initial value at the end of the cycle. If the average voltage were not zero, the current would continuously increase or decrease, indicating that the system is not in a steady state. Therefore, the inductor current can be represented as follows:

$$\Delta I_{L_{(on)}} + \Delta I_{L_{(off)}} = 0$$

$$\left(\frac{V_s}{L}\right) DT + \left(\frac{V_o}{L}\right)(1 - D)T = 0$$

$$(V_s)DT + (V_o)(1 - D)T = 0$$

$$(1 - D)V_o + DV_s = 0$$

$$V_o = -\left(\frac{D}{1 - D}\right) V_s \tag{3.5}$$

The equation implies that the output voltage can be higher when the duty cycle is more than 0.5 and lower when the duty cycle is less than 0.5 than the output. It is noted that output voltage always offers negative polarity with respect to the input voltage. Here, Figure 3.5 demonstrates the waveforms of the voltage and current of the inductor.

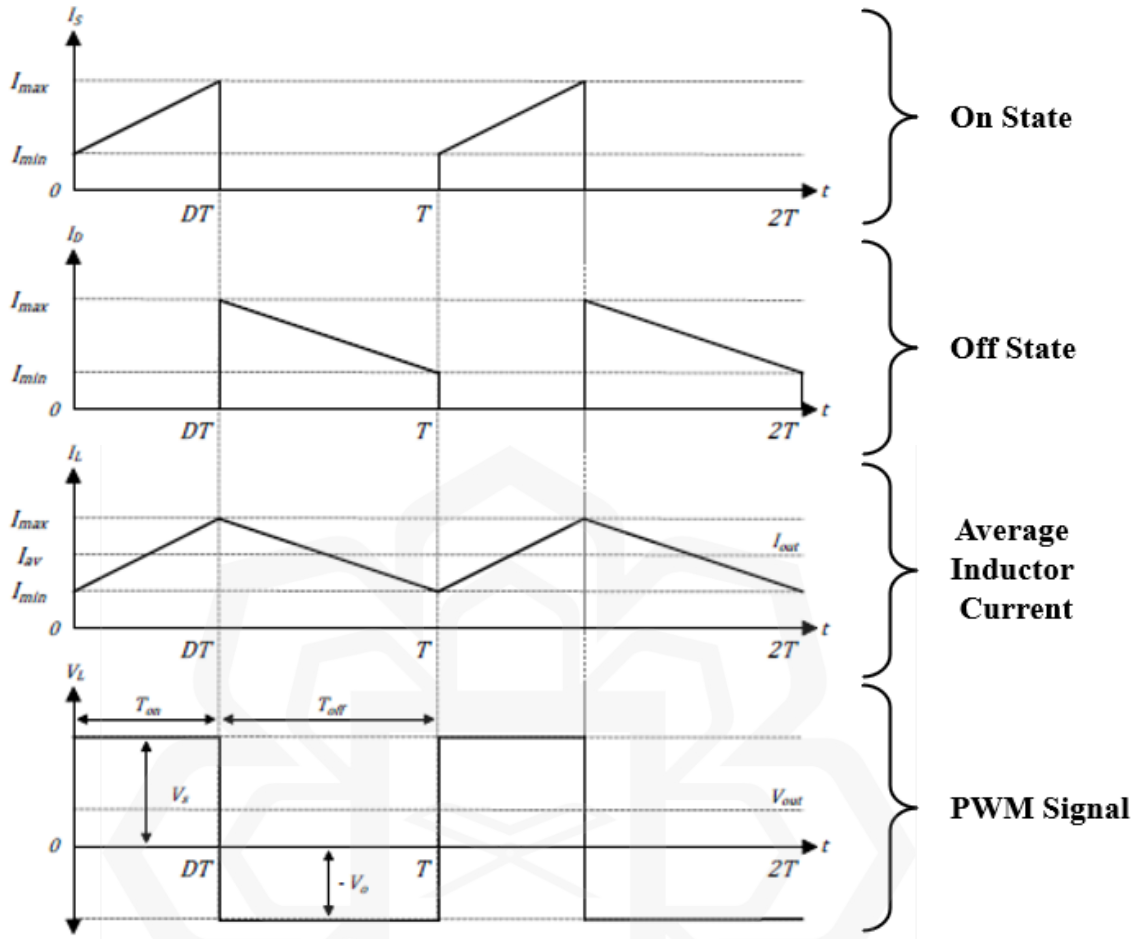

Figure 3.5 Voltage and current waveforms for buck-boost converter (Kabala, 2017).

In general, a buck-boost converter can be operated in continuous conduction mode (CCM) or discontinuous conduction mode (DCM) (Yang et al., 2016). In CCM, the inductor current waveform at a minimum level does not touch zero at any switching period. However, in DCM, the inductor current reaches zero at a minimum level. In general, for buck-boost converters, CCM is mostly considered because it is free from dead time zone and does not let the inductor current reach zero during the operational time.

3.2.2 Non-Inverting buck-boost converter

Inverting buck-boost converter is not able to provide positive output voltage and as a result, in some applications it is not suitable to be implemented. Therefore, SEPIC, Seta and double-switch buck-boost converters are introduced in order to offer positive output voltage.

In this work, both types of buck-boost converter have been used to understand the controllers robustness in different situations. In the first model, inverting buck-boost converter has been used where battery pack is considered as the only ESS. In contrary, non-inverting buck-boost converter has been implemented in the second model where the polarity has been retained considering two switches in the circuit.

3.3 BDC MODELING

For simulation plant, a representative mathematical model is needed. The convenient way to represent it is by using a state space model. The model dynamic of the plant should consider both switch-on and switch-off mode of the buck-boost converter.

3.3.1 Inverting BDC with Battery Model

As it is discussed before, a BDC works depending on the switch-on and switch-off state of insulated gate bipolar transistors (IGBTs) in a circuit. Hence, the mathematical model has been designed considering the states.

Switch-on mode

In switch-on mode, input voltage directly goes to inductor as diode is off and the current increases in inductor with a constant rate. Here, inductor voltage represents positive voltage source and therefore, $V_L = V_s$.

$$V_L = L\left(\frac{dI_L}{dt}\right)$$

$$\left(\frac{dI_L}{dt}\right) = \frac{V_s}{L} \tag{3.6}$$

At the same time, capacitor current is opposite to load current and as a result capacitor voltage decreases linearly. So, it can be represented as

$$I_C = C\left(\frac{dV_C}{dt}\right) = -I_o$$

$$\left(\frac{dV_C}{dt}\right) = -\frac{I_o}{C}$$

$$\left(\frac{dV_C}{dt}\right) = -\frac{V_o}{RC} \tag{3.7}$$

Therefore, a state space model can be derived relying on equations (3.6) and (3.7) as shown in equations (3.8) and (3.9)

$$\dot{x}(t) = A_1 x(t) + B_1 V_s \tag{3.8}$$

$$y = C_1 x \tag{3.9}$$

Here, $A_1 = \begin{bmatrix} 0 & 0 \\ 0 & -\frac{1}{RC} \end{bmatrix}$, $B_1 = \begin{bmatrix} \frac{1}{L} \\ 0 \end{bmatrix}$, $C_1 = [0 \quad 1]$, $x = \begin{bmatrix} I_L \\ V_C \end{bmatrix}$, $y = V_o$

Noted that according to Figure 3.4, the output voltage is the same as the capacitor voltage, $V_o = V_C$.

Switch-off mode

During switch-off mode, the inductor receives voltage from capacitor, and it offers negative polarity. In this period, inductor loses current with a constant rate and reach to the beginning state. Here, capacitor voltage and output voltage are same.

$$-V_o = L\left(\frac{dI_L}{dt}\right)$$

$$\left(\frac{dI_L}{dt}\right) = -\frac{V_o}{L} \tag{3.10}$$

Meanwhile, the capacitor current decreases linearly, and it becomes the subtraction of the peak of the inductor current and load current. As a result, it turns into a concave parabola. Hence, it can be represented as

$$I_C = C\left(\frac{dV_C}{dt}\right) = I_L - I_o$$

$$\left(\frac{dV_C}{dt}\right) = \frac{I_L}{C} - \frac{V_o}{RC} \tag{3.11}$$

Therefore, a similar state space model can be demonstrated as follows:

$$\dot{x}(t) = A_2 x(t) + B_2 V_s \tag{3.12}$$

$$y = C_2 x \tag{3.13}$$

Here, $A_2 = \begin{bmatrix} 0 & -\frac{1}{L} \\ \frac{1}{C} & -\frac{1}{RC} \end{bmatrix}$, $B_2 = \begin{bmatrix} 0 \\ 0 \end{bmatrix}$, $C_2 = [0 \quad 1]$, $x = \begin{bmatrix} I_L \\ V_C \end{bmatrix}$, $y = V_o = V_C$

Similar to Figure 3.4, Figure 3.5 shows that the output voltage is the same as the capacitor voltage, $V_o = V_C$.

The average state-space model can be derived as follows (Vijayalakshmi & T Raja, 2014):

$$A = DA_1 + (1-D)A_2$$

$$= \begin{bmatrix} 0 & 0 \\ 0 & -\frac{1}{RC} \end{bmatrix} D + \begin{bmatrix} 0 & -\frac{1}{L} \\ \frac{1}{C} & -\frac{1}{RC} \end{bmatrix} (1-D)$$

$$= \begin{bmatrix} 0 & \frac{D-1}{L} \\ \frac{1-D}{C} & -\frac{1}{RC} \end{bmatrix}$$

$$B = DB_1 + (1-D)B_2$$

$$= \begin{bmatrix} \frac{1}{L} \\ 0 \end{bmatrix} D + \begin{bmatrix} 0 \\ 0 \end{bmatrix} (1-D)$$

$$= \begin{bmatrix} \frac{1}{L} \\ 0 \end{bmatrix} D$$

$$C = DC_1 + (1-D)C_2$$

$$= [0 \quad 1] \text{ where, } C_1 = C_2$$

Importantly, it is a time-variant model since the duty ratio is required to design the state-space model, and thus, the change in duty ratio impacts the state-space model. Hence, the system is prone to behave as a non-linear model, though the state-space model shows

its linear characteristics. The nonlinearity of the power converter has been identified in previous works as well (Liu & Yang, 2013; Rajarshi & Maksimovic, 2008).

Figure 3.6 shows the topology of a buck–boost converter used in this work. The output voltage, V_o, at resistance, R, is regulated by the switch, S, according to the demand, where V_b is the input voltage from a Li-ion battery to the buck-boost converter. When the switch is on, the battery, input voltage and inductor are active, but while in switched-off mode, the capacitor and the resistor are active. However, there is no set switching frequency, though ideally, it is considered 50 kHz because it is determined by the voltage, which changes continuously with respect to the demand that is controlled by the controller.

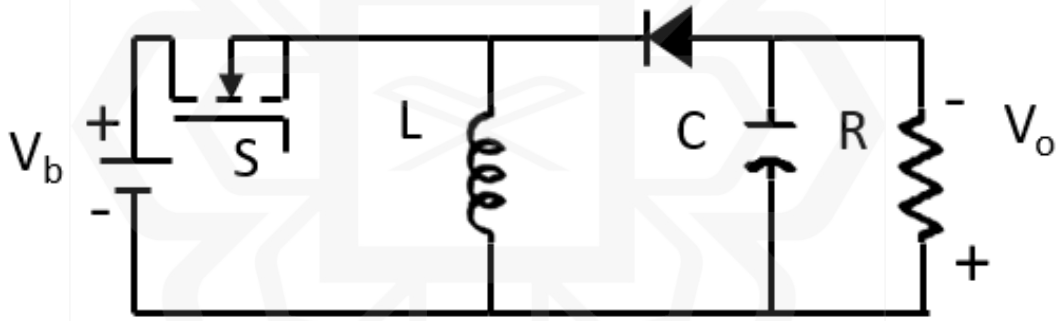

Figure 3.6 A diagram of the buck-boost converter.

The parameters of the buck-boost converter and properties of the Li-ion battery for this simulation work are shown in Table 3.1 (Bellur & Kazimierczuk, 2007; Devi Vidhya & Balaji, 2020; Lai et al., 2017; Pires et al., 2019).

Table 3.1 Properties of the buck-boost converter and lithium-ion battery.

Properties	Values
Inductance, L	5×10^{-4} H
Capacitance, C	9200×10^{-6} F
Capacitor initial voltage, VC	10 V
Resistance, R	25 Ω
Switching frequency	50 kHz
Battery nominal voltage	48 V
Battery rated capacity	14 Ah
Battery initial SOC	95%
Battery response time	0.3 s

3.3.2 Non-Inverting BDC with HESS Model

In this work, the HESS model is constructed based on the combination of SC and battery pack, where the respective BDC regulates SC power. As the primary focus of this work is on the distribution of power according to load demand using two different control algorithms, the three-phase motor and power inverter (also known as DC-AC Converter) have not been considered. However, Figure 3.7 shows all the general components of the HEV powertrain system. The buck-boost converter extracts and supplies the power to the SC, while the boost converter only extracts the power from the battery pack and, thus, plays the role of a unidirectional converter. Figure 3.8 shows the schematic circuit of the boost converter, which includes an inductor, L_1, with two insulated gate bipolar transistors (IGBTs) as S_1 and S_2. Noted that one of the IGBTs, S_2, works as a normal diode. The buck-boost converter also consists of an inductor, L_2, and two IGBTs (e.g., S_3 and S_4) that mainly deal with SC power demand. To run the three-phase BLDC electric motor, a continuous

voltage of 48 V is required, and thus, these DC-DC converters are connected in parallel to a voltage source, DC Bus (Song et al., 2017).

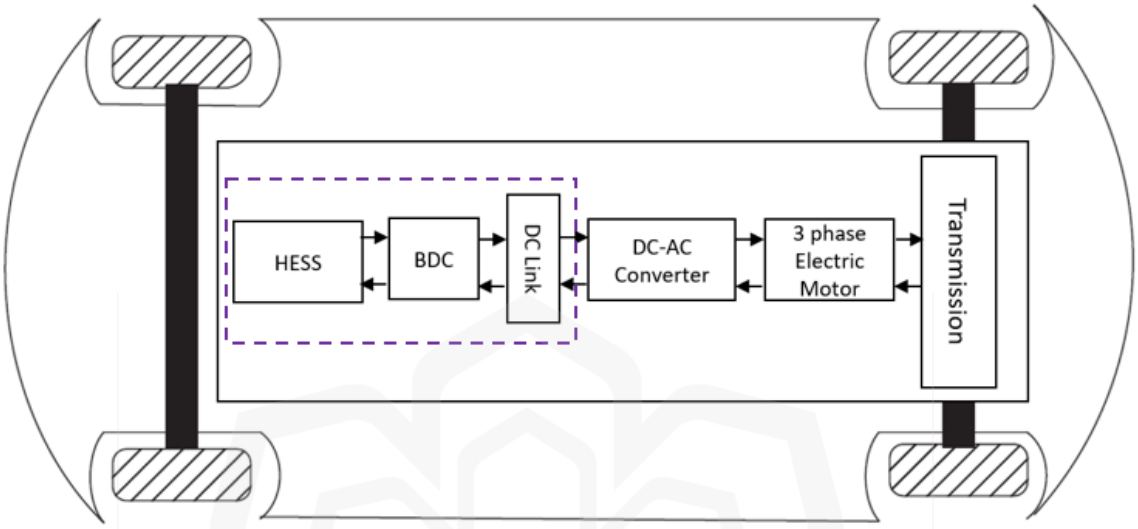

Figure 3.7 Block Diagram of an HEV powertrain.

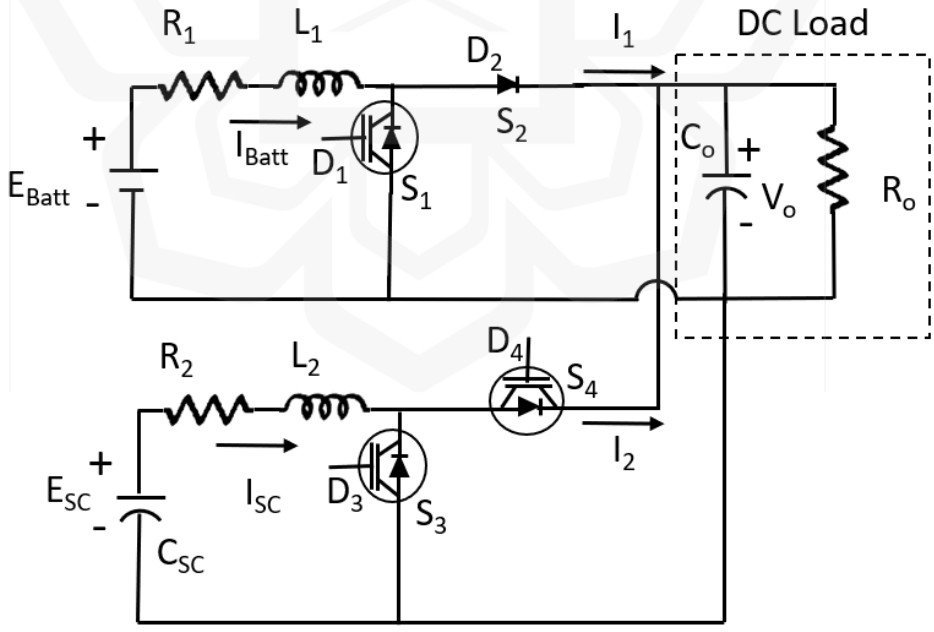

Figure 3.8 Circuit Model of the Buck-Boost Converter with a battery and Boost converter with the SC.

Noted that when the vehicle runs in traction mode, both the converters extract power from the battery pack and SC, where D_1, D_3 and D_4 are active. On the other hand, in braking mode, only D_1 is active, whereas D_3 and D_4. Here, D_1, D_3 and D_4 are the duty ratios in the respective IGBTs. Table 3.2 shows the different driving modes of the vehicle along with the IGBTs status.

Table 3.2 Driving modes and IGBTSs status.

Modes	**Active**	**Inactive**
Acceleration or Traction	D_1, D_3 and D_4	–
Brake	D_1	D_3 and D_4

In this design, a DC-DC boost converter is employed to regulate and increase the battery voltage to the DC bus voltage level. Utilizing the inductor voltage and capacitor charge balance principles, the state-space equations are derived as follows (Arslan et al., 2021) in equation (3.14) and (3.15):

$$\dot{I}_{Batt} = -\frac{R_1}{L_1} I_{Batt} + \frac{E_{Batt}}{L_1} - \frac{V_o}{L_1}(1 - D_1) \tag{3.14}$$

$$\dot{V}_o = \frac{I_{Batt}}{C_o}(1 - D_1) - \frac{I_1}{C_o} \tag{3.15}$$

where I_{Batt}, E_{Batt}, V_o, C_o and I_1 are battery current, battery voltage, DC-bus voltage, capacitance at output and output current of the boost converter, respectively. R_1 is the internal resistance of the battery, L_1 is inductance and control signal D_1 is applied at the switch S_1.

In addition, a DC-DC Buck-Boost converter is used to manage the charging and discharging operations of the SC. During discharging, it boosts the SC output voltage, while

in charging mode, it functions as a buck converter to charge the SC. The differential equation for the SC current in discharging mode can be expressed as (3.16):

$$\dot{I}_{SC} = -\frac{R_2}{L_2} I_{SC} + \frac{E_{SC}}{L_2} - \frac{V_o}{L_2}(1 - D_3) \tag{3.16}$$

where I_{SC}, E_{SC}, R_2 and L_2 are SC current, SC voltage, the internal resistance of the SC and inductance to the respective inductor. D_3 is duty ratio, which is the control input applied at the switch S_3.

Importantly, when the system is operated in boost mode, the output current from the buck-boost converter, I_2, maintains a relationship with the SC current, I_{SC} as shown in the equation (3.17):

$$I_2 = I_{SC}(1 - D_3) \tag{3.17}$$

Besides, in buck mode, D_4 becomes active, and thus, it becomes the new control input which is applied at the switch S_4. As a result, a new differential equation for the SC current can be derived during charging as (3.18):

$$\dot{I}_{SC} = -\frac{R_2}{L_2} I_{SC} + \frac{E_{SC}}{L_2} - \frac{V_o}{L_2} D_4 \tag{3.18}$$

Similar to equation (3.17), another relationship between I_{SC} and I_2 can be derived for buck mode, as shown in the equation (3.19):

$$I_2 = I_{SC} D_4 \tag{3.19}$$

Since D_3 and D_4 are nonlinear signals that are responsible for dealing with the boost and buck modes, a virtual control is necessary to maintain the complete cycle between these two modes as shown in equation (3.20) (Majeed et al., 2020):

$$D = (1 - D_3) \cdot T + D_4 \cdot (1 - T) \tag{3.20}$$

The variable T takes the value 0 or 1 depending on the operating mode of the buck-boost converter. In boost mode, the value of T is 1, since the SC supplies current from the SC to the DC bus. It implies that the current flow is positive (i.e., $I_{SC_{ref}} > 0$). Conversely, in buck mode, the value of T is 0, where the SC is charged through regenerative braking, and using the same convention, the current flow is negative (i.e., $I_{SC_{ref}} < 0$). Mathematically, T can be represented as follows:

$$T = \begin{cases} 1, I_{SC_{ref}} > 0 \\ 0, I_{SC_{ref}} < 0 \end{cases} \tag{3.21}$$

When the system runs in boost mode, according to the equation (3.20), the value of $(1 - D_3)$ can be replaced by D. Thus, equation (3.16) can be represented as shown in the equation (3.22):

$$\dot{I}_{SC} = -\frac{R_2}{L_2} I_{SC} + \frac{E_{SC}}{L_2} - \frac{V_o}{L_2} D \tag{3.22}$$

In the meanwhile, from Kirchhoff's current law, the total output current from the HESS, I_o, can be considered as:

$$I_o = I_1 + I_2$$

$$I_1 = I_o - I_2 \tag{3.23}$$

In the equation (3.23), I_2 can be substituted by the value derived in the equation (3.17). Thus, the equation (3.23) can be represented as:

$$I_1 = I_o - (1 - D_3) I_{SC} \tag{3.24}$$

Again, since the buck-boost converter is functioning in boost mode, according to the equation (3.20), the value of $(1 - D_3)$ can be substituted by D in the equation (3.24). As a result, equation (3.15) can be represented as:

$$\dot{V}_o = \frac{I_{Batt}}{C_o}(1 - D_1) + \frac{I_o}{C_o} - \frac{I_{SC}}{C_o}D \tag{3.25}$$

Finally, considering equation (3.14), (3.22) and (3.25), a globalized average model can be shown as:

$$\begin{cases} \dot{x}_1 = -\dfrac{R_1}{L_1}x_1 + \dfrac{E_{Batt}}{L_1} - \dfrac{x_3}{L_1}(1 - U_1) \\ \dot{x}_2 = -\dfrac{R_2}{L_2}x_2 + \dfrac{E_{SC}}{L_2} - \dfrac{x_3}{L_2}U_2 \\ \dot{x}_3 = \dfrac{x_1}{C_o}(1 - U_1) + \dfrac{I_o}{C_o} - \dfrac{x_2}{C_o}U_2 \end{cases} \tag{3.26}$$

where, $\begin{pmatrix} \dot{x}_1 \\ \dot{x}_2 \\ \dot{x}_3 \end{pmatrix} = \begin{pmatrix} \dot{I}_{Batt} \\ \dot{I}_{SC} \\ \dot{V}_o \end{pmatrix}$ and $\begin{pmatrix} U_1 \\ U_2 \end{pmatrix} = \begin{pmatrix} D_1 \\ D \end{pmatrix}$

Here, x stands for the states, and u represents the control inputs to the system in the form of PWM signals that are regulated by the IGBTs.

This circuit model for the BDC with HESS has been adopted from MATLAB/Simulink Supercapacitor Model example primarily (Mathworks, 2022). The parameters of the power converters and properties of the battery pack and SC for this simulation work have been shown in Table 3.3.

Table 3.3 Parameters of the power converters and properties of the battery pack and SC (Mathworks, 2022).

Components	**Properties**	**Values**
Battery Pack	Battery Nominal Voltage	26.4V
	Battery Rated Capacity	6.6Ah
	Battery Initial SOC	100%
	Battery Response Time	30s
Supercapacitor	Capacitance	500F
	Voltage	16V
	No. of series capacitors	6
	No. of series capacitors	1
Boost and Buck-Boost Converter	Inductance	1×10^{-3} H
	Switching Frequency	40×10^{3} Hz

3.4 CONTROL ALGORITHMS DEVELOPMENT

This section is dedicated to explaining the proposed control algorithms such as MRAC and PI and their design parameters for this system.

3.4.1 MRAC Design

In this work, the Model Reference Adaptive Control (MRAC) algorithm has been chosen primarily as it offers robustness to the system. As the system shows nonlinear behaviour, a linear controller may not be able to handle the nonlinearity. Hence, it is expected that MRAC can ensure a smooth response from this time-variant system that is highly influenced by the duty ratios of multiple IGBT switches. Figure 3.9 demonstrates the complete process of adaptive controller to make the process comprehensible. Here, the

plant, $\dot{x}(t)$ is updated continuously according to a reference model $\dot{x}_m(t)$ based on error, e and error dynamics, $\dot{e}$ between plant and reference models. These error and error dynamics are utilized through adjustment mechanism to generate control input, $u(t)$ of the system and hence, the complete MRAC works.

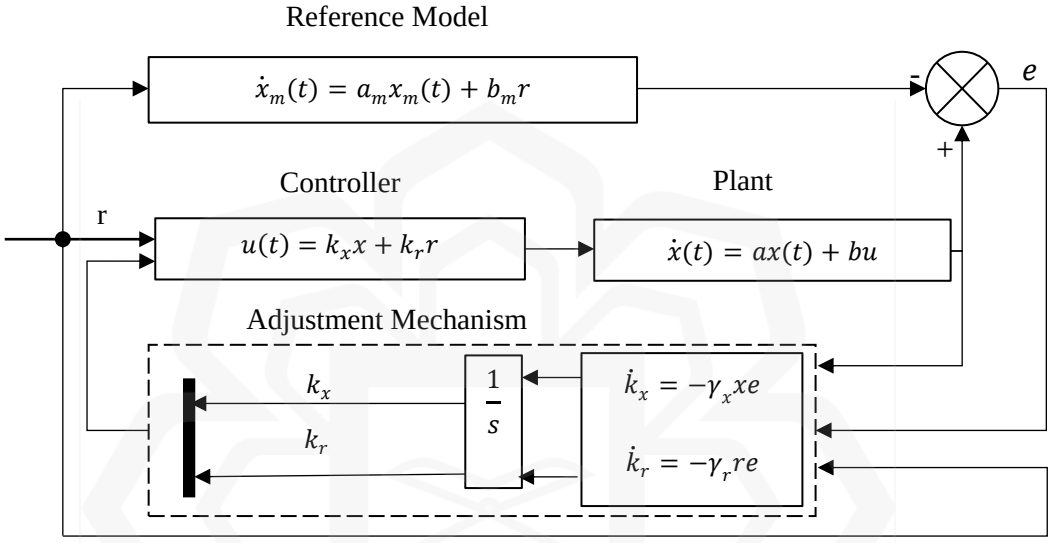

Figure 3.9 A block diagram of the adaptive controller.

To design an MRAC, a plant and a reference model are required so that the difference between the two can be used to adjust the input via an adjustment mechanism. Hence, the plant model can be represented in the state form as shown in the equation (3.27).

$$\dot{x}(t) = ax(t) + bu \tag{3.27}$$

where, $x, a, b \in R$ and $b \neq 0$. a and b are the parameters of the plant, x defines the states that are time-variant and u is the control input.

As for the reference model, although the same states are used, the parameters are constructed based on the desired specifications of a user. In general form, it can be constructed as the equation (3.28):

$$\dot{x}_m(t) = a_m x_m(t) + b_m r \tag{3.28}$$

where, $a_m, b_m, x_m \in R$, and bounded as r is also bounded. Here, a_m and b_m are the parameters of the reference model and r is defined as the reference point.

The main objective is to ensure that the system is responding as the reference model and there, $x(t)$ must behave as $x_m(t)$ does. However, this is not exactly possible because in this work a and b are considered unknown parameters. Therefore, an asymptotical approach can be considered that can lead the plant to reach the same value as the reference by computing the error term as shown in the equation (3.29):

$$e(t) = x - x_m \tag{3.29}$$

Here, to ensure the response from the plant alike reference, the error term needs to satisfy this condition $e(t) \to 0$ when $t \to \propto$. Therefore, the control law can be deduced at the same time for state feedback control as in the equation (3.30):

$$u(t) = k_x x + k_r r \tag{3.30}$$

where, k_x and k_r are considered as constant adjustable gains.

In the meanwhile, to address error dynamics, an equation can be shown as follows:

$$\dot{e}(t) = \dot{x} - \dot{x}_m$$

$$= ax + bu - (a_m x_m + b_m r)$$

$$= ax + b(k_x x + k_r r) - a_m x_m - b_m r$$

$$\dot{e}(t) = (a + bk_x)x - a_m x_m + bk_r r - b_m r \tag{3.31}$$

Importantly, to make the error dynamics zero, a_m and b_m can be derived as follows:

$$a + bk_x = a_m \tag{3.32}$$

$$bk_r = b_m \tag{3.33}$$

If the values of a_m and b_m, as derived from equations (3.32) and (3.33), are substituted in the equation (3.31), the error dynamics can be represented as:

$$\dot{e} = a_m(x - x_m) + b_m r - b_m r$$

$$\dot{e} = a_m(x - x_m) \tag{3.34}$$

Again, the value of $e(t)$ can be substituted in the equation (3.34) and thus the error dynamics can be derived as:

$$\dot{e} = a_m e \tag{3.35}$$

Notwithstanding the error, e, depends on a and b where both the parameters are unknown. Therefore, a new control law is introduced that can estimate the error between the plant and reference model according to the sample time and finally ensure the error, e as zero. The control law can be addressed as follows in the equation (3.36):

$$u = \hat{k}_x(t)x + \hat{k}_r(t)r \tag{3.36}$$

where $\hat{k}_x(t)$ and $\hat{k}_r(t)$ are the estimated value of k_x and k_r respectively.

Hence, a_m and b_m can be newly defined from the equations (3.32) and (3.33) and thus, these parameters become time-varying, as shown in the equations (3.37) and (3.38).

$$a + b\hat{k}_x(t) = a_m \tag{3.37}$$

$$b\hat{k}_r(t) = b_m \tag{3.38}$$

As a result, the closed-loop error dynamics can be demonstrated by replacing the values of a_m and b_m as follows in the equation (3.39):

$$\dot{e}(t) = (a + bk_x)x - a_m x_m + bk_r r - b_m r$$

$$= \left[(a_m - b\hat{k}_x) + bk_x\right]x - a_m x_m + bk_r r - b\hat{k}_r r$$

$$= a_m(x - x_m) - b\left(\hat{k}_x - k_x\right)x - b\left(\hat{k}_r - k_r\right)r$$

$$\dot{e}(t) = a_m e - b\tilde{k}_x x - b\tilde{k}_r r \tag{3.39}$$

where, $\left(\hat{k}_x - k_x\right) = \tilde{k}_x$ and $\left(\hat{k}_r - k_r\right) = \tilde{k}_r$

In order to ensure the system stability, a Lyapunov function candidate is required to be considered, and as a result, it can be expressed finally in the equation (3.40):

$$V\left(e, \tilde{k}_x, \tilde{k}_r\right) = \frac{1}{2}e^2 + \frac{1}{2\gamma_x}\tilde{k}_x{}^2 + \frac{1}{2\gamma_r}\tilde{k}_r{}^2$$

$$\frac{\partial V}{\partial t} = e\dot{e} + \frac{1}{\gamma}\tilde{k}_x\dot{\tilde{k}}_x + \frac{1}{\gamma}\tilde{k}_r\dot{\tilde{k}}_r$$

$$\dot{V} = e\left(a_m e - b\tilde{k}_x x - b\tilde{k}_r r\right) + \frac{1}{\gamma}\tilde{k}_x\left(-\dot{\hat{k}}_x\right) + \frac{1}{\gamma}\tilde{k}_r\left(-\dot{\hat{k}}_r\right)$$

$$\dot{V} = a_m e^2 - b\tilde{k}_x xe - b\tilde{k}_r re - \frac{1}{\gamma}\tilde{k}_x\dot{\hat{k}}_x - \frac{1}{\gamma}\tilde{k}_r\dot{\hat{k}}_r \tag{3.40}$$

where, γ_x and γ_r are the adaptation gains.

In this circumstance, $\dot{V}$ should be negative semi-definite to ensure the system's stability (Nguyen & Nguyen, 2018). So, $\dot{\hat{k}}_r$ and $\dot{\hat{k}}_x$ can be defined as equations (3.41) and (3.42) respectively in order to ensure $\dot{V} < 0$ where $b > 0$:

$$\dot{\hat{k}}_r = -\gamma bre \tag{3.41}$$

$$\dot{\hat{k}}_x = -\gamma bxe \tag{3.42}$$

Now, the values of $\dot{\hat{k}}_r$ and $\dot{\hat{k}}_x$ can be substituted to equation (3.40) to obtain the value of $\dot{V}$ as:

$$\dot{V} = a_m e^2 \tag{3.43}$$

Importantly, during reference model designing, a_m has been considered as negative. Therefore, $\dot{V}$ considered as negative semi-definite, which implies that the system is stable.

3.4.2 Proportional-Integral (PI) Controller

The PI control approach is commonly used with the DC-DC converter because of its simplicity in design and ability to ensure promising performance. Since the methodology of the PI controller is already well known, only the final form is presented. Figure 3.10 represents a closed-loop control system where a PI controller is used to regulate the voltage or current of a DC-DC converter. The desired output, x_d, is compared with the actual output, x_a, to generate an error signal. This error signal is processed by the PI controller, which adjusts the control input, u based on proportional and integral actions. The DC-DC converter dynamics are described by the equation (3.27), where the control input influences the system state, x. The actual output is fed back to the input for continuous adjustment, aiming to minimize the error and achieve the desired output. The PI controller, C_{PI}, can be defined as follows:

$$C_{PI} = K_P + \frac{K_I}{s} \tag{3.44}$$

$$u(t) = \left(K_P + \frac{K_I}{s}\right) e \tag{3.45}$$

where, $e(t) = x_d - x_a$.

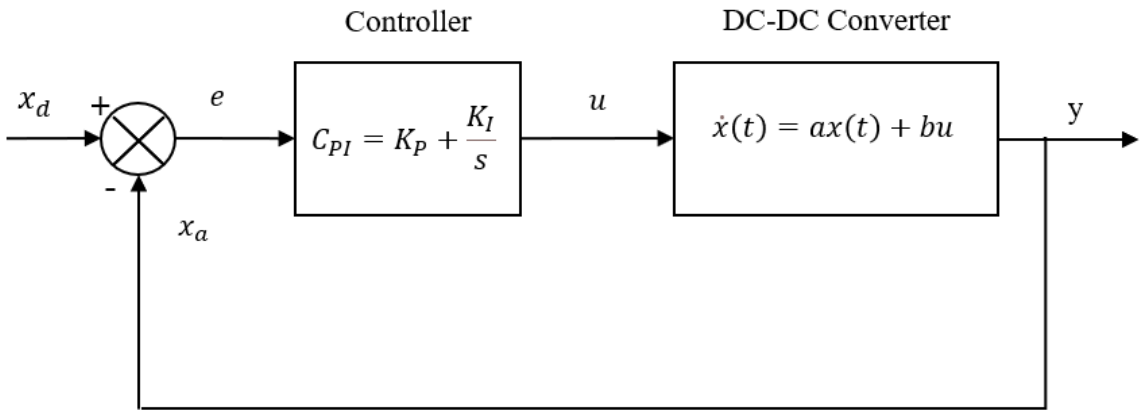

Figure 3.10 A block diagram of a DC-DC converter with a PI controller.

3.5 PROPOSED CONTROLLERS FOR INVERTING BDC

The MRAC design and PI controller design have been explained in Section 3.4.1 and 3.4.2 (Islam et al., 2021), respectively, and hence, this section will introduce the reference model for MRAC and tuning parameters for both controllers. Before that, Figure 3.9 has been introduced to explain how the controller is integrated with the system for controlling the output, V_o according to the reference voltage, V_{ref}, and supplying suitable input, u and overcoming the disturbance, d when it is added to the system. In this block diagram, the controller block can be replaced by any of the controllers. Hence, it describes the primary functions of the controllers with the system in both cases, either with disturbance or without disturbance.

3.5.1 MRAC Design

According to MRAC design requirements for a system, designing a reference model is crucial since it defines the desired behaviour of the system, serving as a benchmark for performance. It guides the adaptive controller to adjust system parameters dynamically,

ensuring the actual system output matches the desired response, thereby enhancing stability and performance.

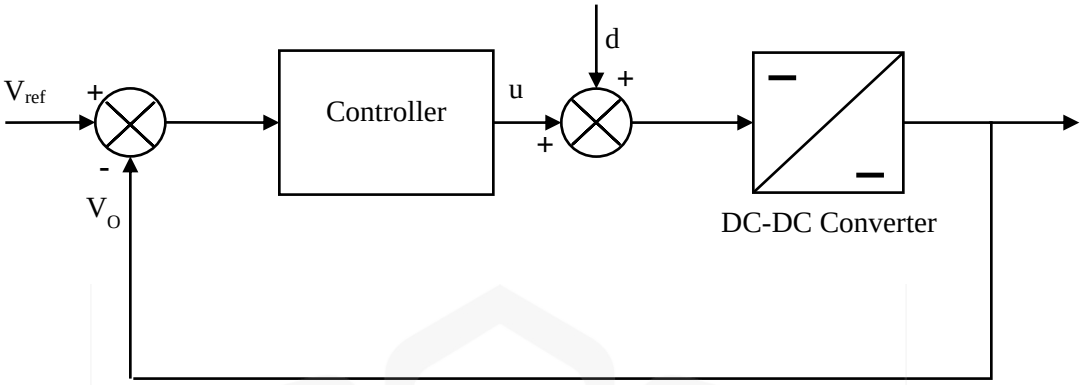

Figure 3.11 A block diagram of a DC-DC converter with a controller.

Hence, a reference model for the MRAC is designed to achieve specific output characteristics: a rise time of 0.2 seconds, a settling time of less than 0.5 seconds, and 0% overshoot. The design process has been adopted from prior studies (Modabbernia et al., 2013; Utomo et al., 2011; Zhou & He, 2015) which provided benchmarks for assessing the controller's performance. Considering the design characteristics of a system, a transfer function can be generated, which is represented as a state-space model as follows in the equation (3.46):

$$A_m = \begin{bmatrix} -720 & -8100 \\ 1 & 0 \end{bmatrix}, B_m = \begin{bmatrix} 1 \\ 0 \end{bmatrix}, C_m = [0 \quad 8100] \tag{3.46}$$

Importantly, the adaptation gains in the adjustment mechanism significantly influence system responses. Therefore, these gains must be selected meticulously to ensure that the system maintains the reference model's output characteristics. After several trials, the adaptation gains γ_x and γ_r are determined to be 2, with initial integral gains of 11 for

the states and reference input, respectively. The design analysis procedure has been discussed further in section 3.6.2 with the HESS model.

3.5.2 PI Controller Design

Unlike MRAC, PI controller designing solely relies on the fixed K_I and K_p gain and does not include a reference model. Hence, a heuristic method has been adopted for the proposed system to tune the gain of PI due to its simplicity and nonlinear characteristics. Based on the extreme system responses due to the consideration of higher K_I and K_p gain of the PI controller, the gains are bounded by 0 and 100. However, the demonstration of the system responses against the variations of the gains has been avoided since the analysis is not considered as a contribution.

3.5.3 Parameters of MRAC and PI Controller

Upon several trials, the final adaptation gains of MRAC and PI gains have been achieved, allowing the system to perform with a rise time of 0.2 seconds, a settling time of less than 0.5 seconds, and a 0% overshoot. Table 3.4 highlights the adjustable gains of MRAC and PI gains considered in this study.

Table 3.4 Parameters of MRAC and PI controller for BDC with battery model.

MRAC	PI
Adaptation gain for states, γ_x = 2 Adaptation gain for reference, γ_r = 2 Initial integral gain for states, k_{x_0} = 11 Initial integral gain for reference, k_{r_0} = 11	Proportional gain, K_P = 5 Integral gain, K_I = 8

3.6 POWER MANAGEMENT SYSTEM AND CONTROLLERS FOR HESS MODEL

Since HESS works relying on two different BDCs and they contribute to meeting the power demand separately, a suitable power management system should be designed that can designate each BDC to extract a certain amount of power from a single ESS. Hence, this section has introduced a power management system and controller design as well.

3.6.1 Power Management System

A Power Management System (PMS) is needed to distribute the necessary amount of power to the motor from the HESS. In addition, it is also used to improve battery safety, energy consumption, efficiency, and system dynamics (Song et al., 2017). There are various types of strategies that can be used for the PMS such as rule-based strategy (Song et al., 2017), filtration-based strategy (Hadartz & Julander, 2008), "all or nothing" control strategy (Allegre et al., 2009), fuzzy logic strategy (Song et al., 2014) and model predictive strategy (Hannan et al., 2012).

For the simplicity of simulation and better adaptability according to a drive cycle, the rule-based approach is adopted in this work as shown in Figure 3.12. This technique enables the battery pack to supply power if the load demand from the motor, P_d, exceeds zero. In the meantime, the SC remains constant until P_d meets the P_{min} cut-off that is considered as 1.5 kW since the total system is considered to be run for 600s only that will make the battery and SC depleted. In addition, the power fluctuation is prominently visible around 1.5 kW for this drive cycle. Noted that the cut-off power is changeable according to system run time, power storage or the rate of power discharge.

In the meantime, once P_d surpasses the P_{min} limit, the SC supplies the remaining demand of the power as $(P_d - P_{min})$. To guarantee effective power conversion, the state of charge (SOC) of the SC is closely monitored during this period. As a result, the SC voltage managed to remain between $0.5V_{SC_{max}}$ and $V_{SC_{max}}$. In this case, the operational condition for the battery pack has been considered between 20% and 90% of the SOC.

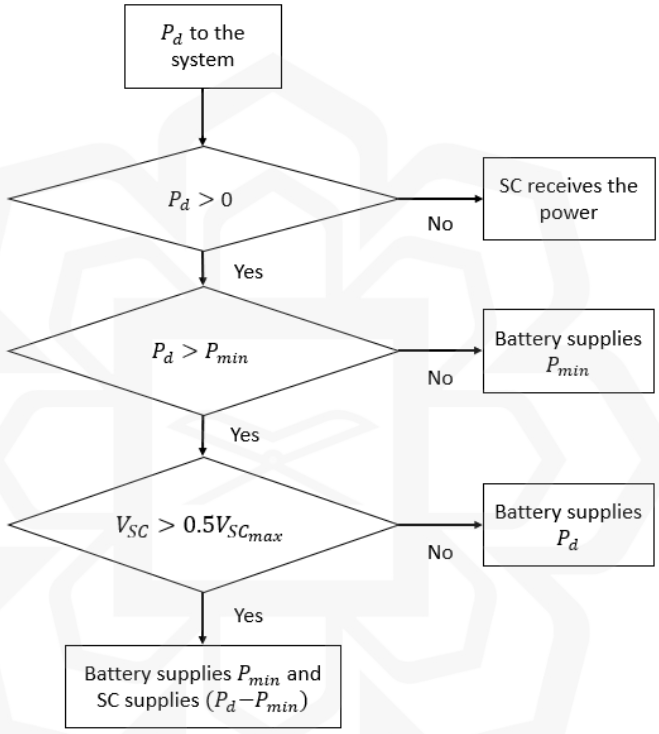

Figure 3.12 Rule-Based Energy Management System.

3.6.2 Proposed Controllers for HSS Model

This section describes the MRAC reference model and gain tuning, and PI controller gain tuning for the non-inverting BDC with HESS model. In this HESS model, the battery ensures comparatively constant power supply to the motor and is not designed for receiving regenerative power during braking, the battery current, I_{Batt} is regulated by a PI controller for simplicity. Figure 3.13 (a) depicts a control strategy where the battery power is directly

controlled using a PI controller. Hence, the power demand P_d or P_{min} is divided by the battery voltage to compute the desired current. This current is compared with the actual battery current, I_{Batt}, and the error is fed into the PI controller. The output of the PI controller is then used to regulate the boost converter, which adjusts the battery current, I_{Batt} to meet the power demand efficiently. On the other hand, SC needs to support the rest of the power demand, especially the fluctuation. Thus, it supplies the rest of the power by regulating its current, I_{SC}. Noted that both MRAC and PI controllers have been considered where their performance will be compared in this case due to its regular fluctuation. Figure 3.13 (b) shows PI control strategy for regulating SC current. Here, the difference between P_d and P_{min} is divided by the SC voltage to calculate the desired SC current. This current is compared with the actual SC current, I_{SC}, and the error is processed by a PI controller. In order to evaluate the performance of the PI controller with the presence of disturbance in the system, the controller output, u is influenced by the disturbance, d which become the input to the buck-boost converter. Similarly, Figure 3.13 (c) shows the difference between P_d and P_{min} is divided by the SC voltage to calculate the desired SC current which is controlled by MRAC algorithm. As discussed earlier, the MRAC system comprises a reference model that defines the desired system behaviour and an adjustment mechanism that tunes the controller parameters in real-time to match this behaviour. Since the robustness of this controller is a concern, a disturbance is also considered with the system input.

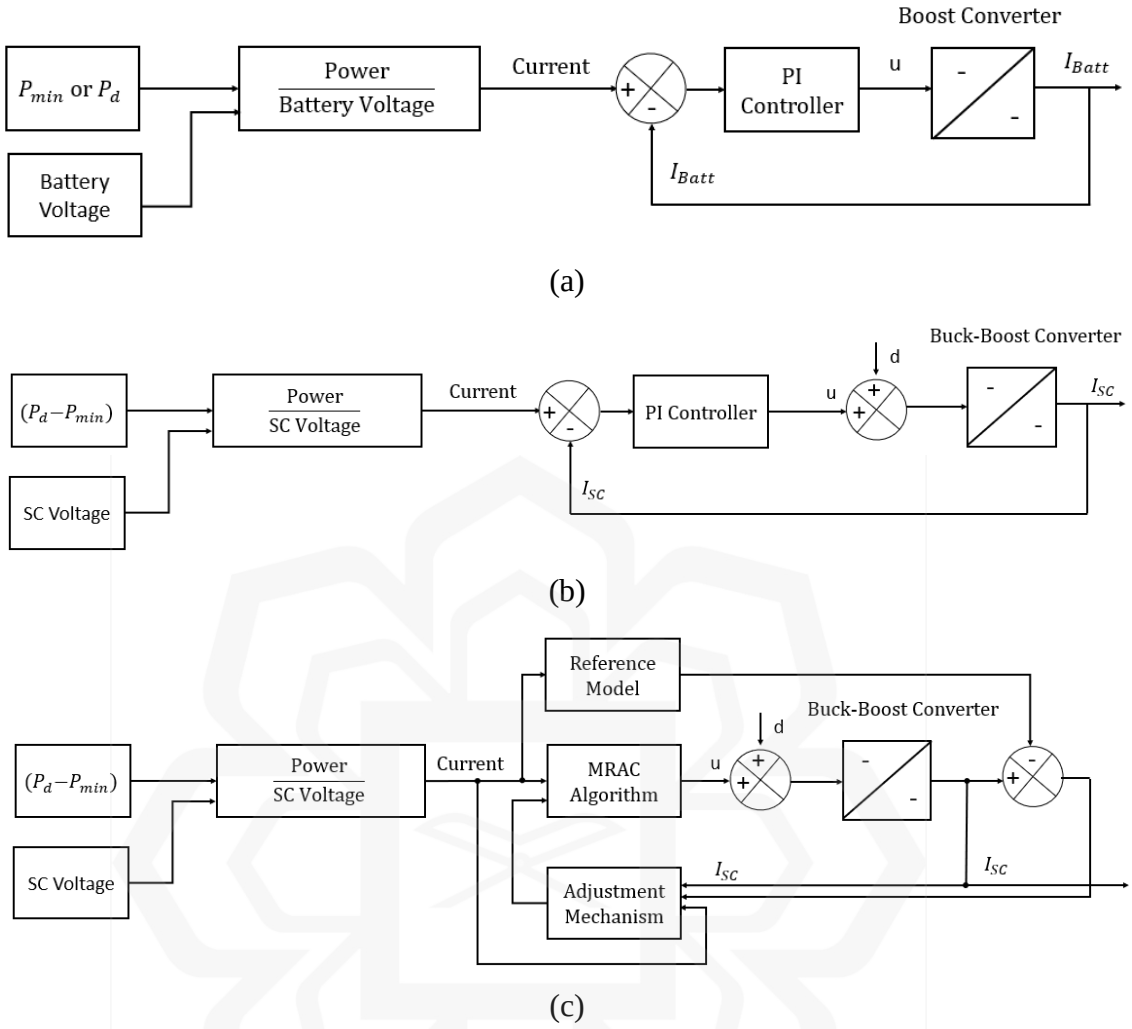

Figure 3.13 A block diagram of a (a) boost converter with PI controller that regulates I_{Batt}, and buck-boost converter with a (b) PI control and (c) DMRAC algorithm that control I_{SC}.

3.6.2.1 Lyapunov Stability

Before tuning the MRAC, ensuring the stability of the non-inverting BDC is cardinal. Hence, to analyze the Lyapunov stability of the system represented by the Equation (3.25), a few steps to be followed:

1. **System identification:** According to the Equation (3.25), the system is a set of three coupled first-order differential equations representing the dynamics of the state variables x_1, x_2, and x_3.

2. **Lyapunov function:** According to the mathematical equation as described in Equation (3.25), a Lyapunov candidate function can be proposed, such as:

$$V(x) = \frac{1}{2}(x_1^2 + x_2^2 + x_3^2) \tag{3.47}$$

This function is positive definite, meaning $V(x) > 0$ for all $x \neq 0$ and $V(0) = 0$.

3. **Derivative of the Lyapunov function:** As part of the stability analysis process, the time derivative of the proposed Lyapunov function should be computed that can be shown as:

$$\dot{V}(x) = x_1 \cdot \dot{x_1} + x_2 \cdot \dot{x_2} + x_3 \cdot \dot{x_3} \tag{3.48}$$

In Equation (3.53), the state variables and their derivatives can be substituted as follows:

$$\begin{aligned}\dot{V}(x) = -V_o \cdot (1 - D_1) \cdot I_{Batt} \cdot L_2 \cdot C_o - V_o \cdot D \cdot I_{SC} \cdot L_1 \cdot C_o + V_o \\ \cdot (1 - D_1) \cdot I_{Batt} \cdot L_2 \cdot L_1 + V_o \cdot I_o \cdot L_2 \cdot L_1 - V_o \cdot D \\ \cdot I_{SC} \cdot L_2 \cdot L_1\end{aligned} \tag{3.49}$$

Upon substituting the values of the parameters according to Table 3.3, in Equation (3.49), it can be represented as:

$$\begin{aligned}\dot{V}(x) = -(24 - 48 \cdot 10^{-6}) \cdot (1 - D_1) \cdot I_{Batt} - (24 - 48 \cdot 10^{-6}) \\ \cdot D \cdot I_{SC} + 48 \cdot 10^{-6} \cdot I_o \cdot D\end{aligned} \tag{3.50}$$

4. **Stability analysis:** Based on the sign of $\dot{V}(x)$, three scenarios can be considered as negative definite, negative semidefinite and positive, which can define the status of a system's stability. For instance, the system can be globally asymptotically stable if $\dot{V}(x)$ is identified as a negative definite, which implies $\dot{V}(x) < 0$ for all $x \neq 0$. In addition, the system can be stable only without being asymptotically stable if $\dot{V}(x)$ is identified as negative definite, which implies $\dot{V}(x) \leq 0$ for all $x \neq 0$. Furthermore, the system cannot be declared stable when $\dot{V}(x)$ is found positive or indefinite. In order to analyze the stability of the proposed system, the derivative of the proposed Lyapunov candidate function can be rewritten as:

$$\dot{V}(x) = -C_1(1 - D_1) \cdot I_{Batt} - C_1 \cdot D \cdot I_{SC} + C_2 \cdot I_o \cdot D \tag{3.51}$$

where, $C_1 = 24 - 48 \cdot 10^{-6}$ and $C_2 = 48 \cdot 10^{-6}$.

Here, C_1 is certainly greater than C_2 and therefore, the negative elements, $-C_1(1 - D_1) \cdot I_{Batt} - C_1 \cdot D \cdot I_{SC}$ is predominant over the positive elements, $C_2 \cdot I_o \cdot D$ in Equation (3.51). As a result, by no means, $\dot{V}(x)$ can be either positive or negative definite, which implies that $\dot{V}(x)$ is negative definite. Thus, according to Lyapunov stability analysis, the proposed system, the non-inverting BDC, can be declared stable.

3.6.2.2 MRAC Design for Non-Inverting BDC

Considering the previous study (Storebø, 2021), in this model, the reference model for MRAC is designed based on the second-order desired output's characteristics, such as 0.03s rise time, 0.06s settling time, and 0% overshoot where both rise time and settling time are

set faster than the previous model as described in Section 3.5. So, the state-space model of the reference model can be derived as:

$$A_m = \begin{bmatrix} -200 & -9000 \\ 1 & 0 \end{bmatrix}, B_m = \begin{bmatrix} 1 \\ 0 \end{bmatrix}, C_m = [0 \quad 9000] \tag{3.52}$$

Typically, controller performance is determined by the gains; consequently, selecting an appropriate gain is a vital step for controllers. To choose the appropriate gains for PI and MRAC, a variety of approaches can be considered. The heuristic approach has been taken into consideration in this work for both PI and MRAC control algorithms. The aim is to select the gains that will give less spike and fluctuation. For MRAC, the values both for γ_x and γ_r must be positive according to the control design method and therefore, γ_x and γ_r range [0, 10] and [0, 1] respectively. Noted that the value of γ_r should be changed in slower rate in order to allow the controller to adapt slowly and accurately.

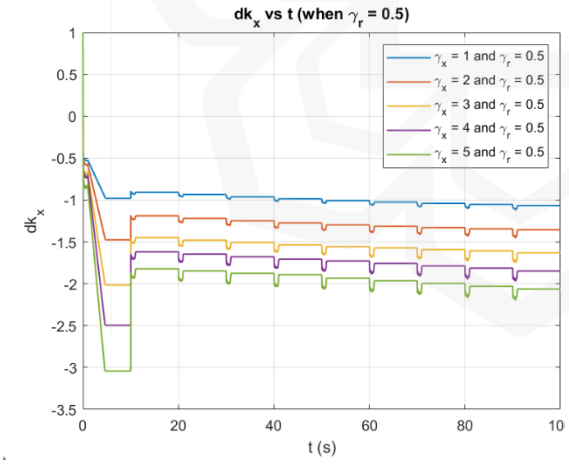

(a)

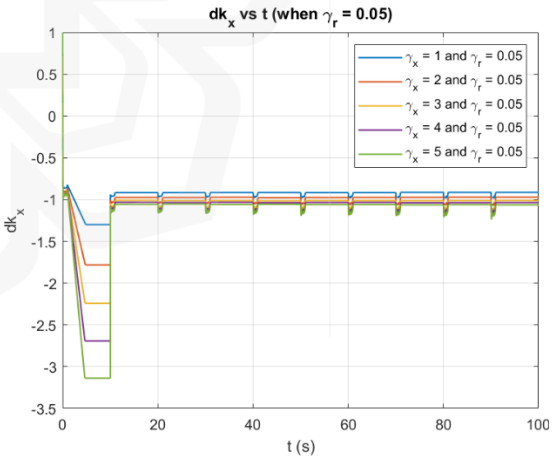

(b)

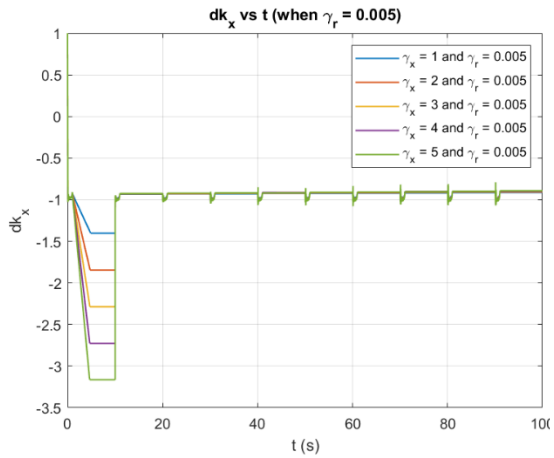

(c)

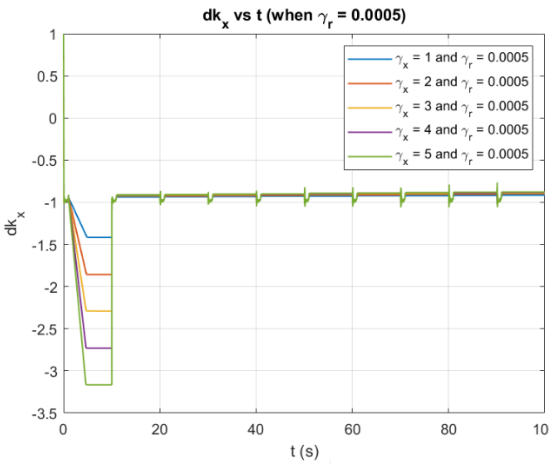

(d)

Figure 3.14 Changes of dk_x with respect to time when (a) γ_r = 0.5, (b) γ_r = 0.05, (c) γ_r = 0.005 and (d) γ_r = 0.0005.

Figure 3.14 demonstrates that both dk_x (or $\dot{k}_x$) and dk_r (or $\dot{k}_r$) in MRAC are significantly influenced by the values of γ_x and γ_r. In this case, γ_r is varied between 0.5, 0.05, 0.005, and 0.0005 since the values of γ_r lower than 0.0005 make the adaption rate extremely slow, and therefore, the system fails to follow the reference model response and track the desired SC current.

In Figure 3.14 (a), where γ_r = 0.5, it is observed that as γ_x increases from 1 to 5, $\dot{k}_x$ shows a decreasing trend in its steady-state value, with more pronounced periodic fluctuations. The system starts with a significant initial transient before stabilizing into a periodic behaviour that remains consistent over time. The magnitude of the periodic fluctuations increases with higher γ_x values, indicating greater instability in the system's adaptation process. Figure 3.14 (b) shows that with γ_r = 0.05, the overall behaviour of $\dot{k}_x$ becomes more stable compared to the first plot. The initial transient is still present, but the periodic fluctuations are less pronounced, particularly for lower γ_x values. As γ_x increases,

the periodicity in $\dot{k}_x$ persists, but the system demonstrates a faster stabilization compared to the case with γ_r = 0.5. In addition, Figure 3.14 (c), where γ_r = 0.005, shows the comparatively more stable behaviour of $\dot{k}_x$. Here, the periodic fluctuations are relatively minimal across all values of γ_x, and the system quickly settles into a steady state. The influence of γ_x on $\dot{k}_x$ is less pronounced, suggesting that a lower γ_x significantly improves the system's stability and reduces the sensitivity of $\dot{k}_x$ to changes in γ_x. Finally, when γ_r is set to 0.0005, as shown in Figure 3.14 (d), $\dot{k}_x$ exhibits a slower rate of change and lower magnitude peaks in periodic fluctuations compared to scenarios where γ_r is set to 0.5, 0.05, or 0.005. Consequently, this configuration allows the MRAC to reduce the error at a slower pace, enabling the system to track the desired SC current without producing abrupt peaks.

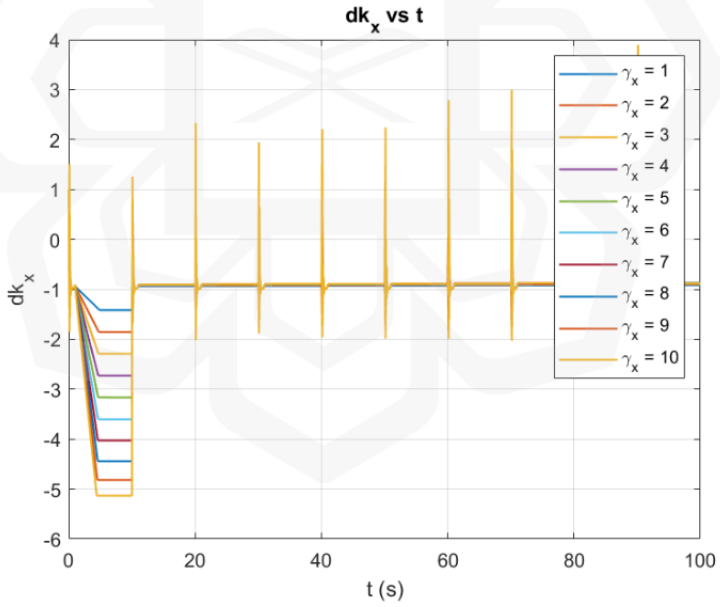

(a)

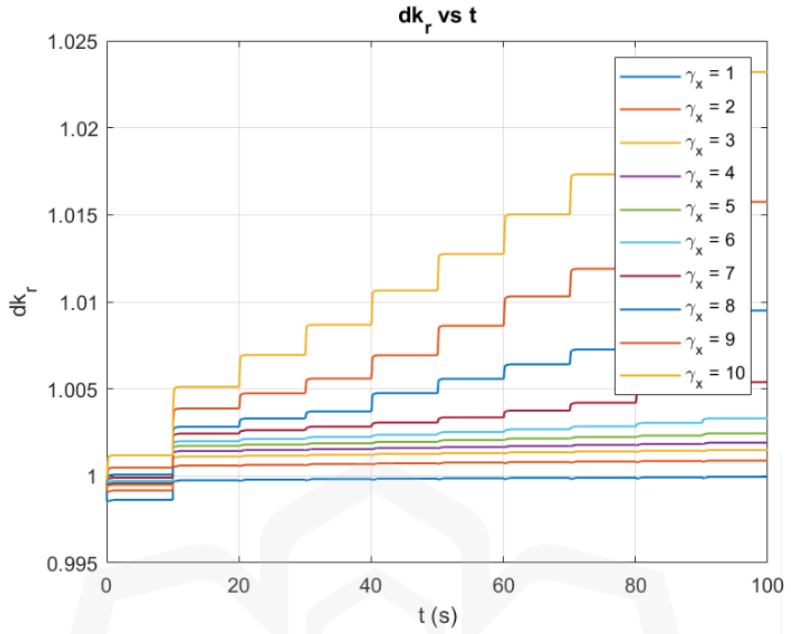

(b)

Figure 3.15 Changes of (a) dk_x and (b) dk_r with respect to the time when γ_r = 0.0005.

In addition, the behaviours of $\dot{k}_x$ and $\dot{k}_r$ across different values of γ_x are essential in understanding the stability and adaptability of the MRAC system, as shown in Figure 3.15 (a) demonstrates that as γ_x increases, the system experiences more pronounced oscillations. This behaviour indicates that larger γ_x values result in a more aggressive adaptation response, which can lead to instability. For example, when γ_x is set to 1, the system exhibits minimal oscillations, indicating stable adaptation. As a result, the response is smooth, with no significant fluctuations, reflecting a controlled and stable process. Subsequently, when γ_x is increased to 5, the oscillations become more pronounced, with visible spikes in $\dot{k}_x$. These spikes suggest that the system is overcompensating, leading to potential instability. The adaptation is comparatively faster, but the system is more prone to instability. Finally, with the increment of γ_x from 5 to 10, the oscillations reach their peak in both magnitude and frequency. The system shows signs of instability with frequent

and large fluctuations in γ_x. Hence, the aggressive adaptation can lead to excessive corrections, making the system less stable and less reliable. Besides, Figure 3.15 (b) shows a stepped increase over time of $\dot{k}_r$, with the magnitude of each step becoming more pronounced as γ_x increases. This stepped behaviour indicates a more gradual and stable adaptation process compared to $\dot{k}_x$. In order to explain the trend better in brief, three values for γ_x have been chosen as 1, 5 and 10. When γ_x = 1, the steps in $\dot{k}_r$ are found small and uniform, reflecting a stable and consistent adaptation process. The system responds slowly but steadily, ensuring stable performance. In addition, when γ_x is chosen as 1, the steps are more vivid, indicating a faster adaptation process. While the system is still relatively stable, the increased step size suggests a more aggressive adaptation, with a potential risk of overreaction. Finally, in order to comprehend a comparatively extreme situation by setting γ_x as 10, the steps are noticed become large and more spaced out, indicating a more pronounced response in $\dot{k}_r$. Although the system remains stable, the larger steps suggest that the adaptation is more forceful, which could lead to less precise control. This comparative analysis of both $\dot{k}_x$ and $\dot{k}_r$ reveals a trade-off between adaptation speed and system stability. Higher γ_x values increase the adaptation speed but introduce instability, especially in $\dot{k}_x$ which can be characterized by large oscillations and frequent spikes.

3.6.2.3 PI Controller Tuning for Non-Inverting BDC Model

Similar to the approach outlined in Section 3.5, the PI gains are tuned using a heuristic method. The initial values for the K_P and K_I gains of the PI controller were selected within the range of 0 to 100, based on the system's extreme response characteristics.

3.6.2.4 Controller Parameters

The parameters, considered for tuning both MRAC and PI controllers have been presented in Table 3.5 as follows:

Table 3.5 Parameters of MRAC and PI controller.

MRAC	PI
Rate of adaptation for states, γ_x = 1 Rate of adaptation for reference, γ_r = 0.0005 Initial gain for states, k_{x_0} = 1 Initial gain for reference, k_{r_0} = 1	Proportional gain, k_p = 1.5 Integral gain, k_i = 1

3.7 VALIDATION MODEL AND DRIVE CYCLES

The final part is to integrate the system with a validation model. This step is necessary to assess the capability of the controller for the overall EV operation. Therefore, a ready-build EV longitudinal model that is available from the MATLAB extension file (Team, 2023) is utilized with several modifications to integrate the proposed controller. Figure 3.16 demonstrates the interface of the Simulink file. This model is derived based on several assumptions, such as

- Quasi-standard model that is widely used both in academia and industry.
- Equation-based model.
- Code generation is possible from this model for any further hardware test and deployment.

This EV model has five main components: vehicle dynamics model, brake system that includes a regenerative braking system, motor dynamics model, driveline, and energy storage system, as shown in Figure 3.16. In addition, there is a driver model that is primarily a PID controller that tracks the drive-cycles certified by The Environmental Protection

Agency (EPA). Importantly, this agency uses EPA driving cycles, a set of uniform tests, to assess automobile emissions and fuel economy.

In order to calculate the official fuel economy ratings that are displayed on the window stickers of new automobiles, drive cycles that imitate real-world driving situations are used. There are various drive cycles, each of which is intended to depict a certain kind of driving pattern. These comprise the city cycle, the highway cycle, and a mixed cycle that combines driving on both highways and cities. Each cycle has its own speed, acceleration, and deceleration settings that are intended to mimic actual driving behaviour (Agency, 2022).

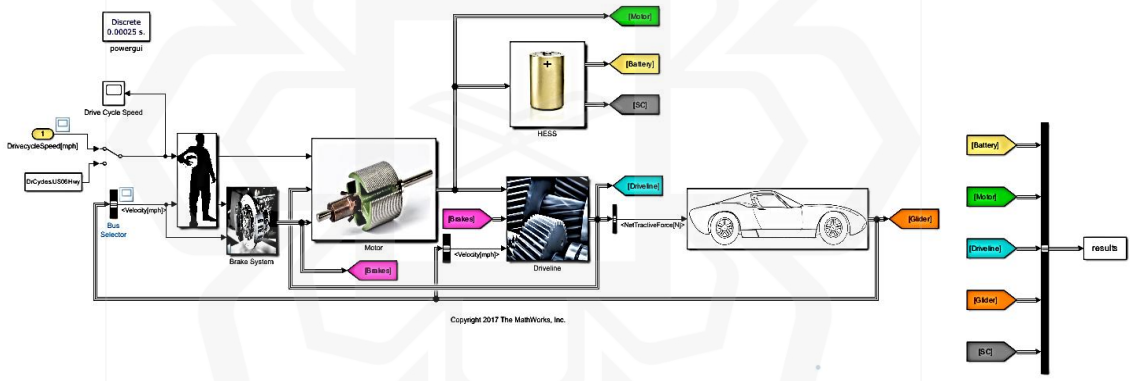

Figure 3.16 Interface of an EV model in Simulink designed by MathWorks.

The vehicle design of an electric vehicle (EV) refers to its motion and behaviour in the direction of travel, specifically concerning acceleration, deceleration, and speed control. Understanding and modelling these dynamics are essential for designing control systems, optimizing energy management, and ensuring the safe and efficient operation of EVs. There are various variations of this model with regard to its fidelity, which depends on the application. As for this work, the simple vehicle model is adopted from MATLAB (Team,

2020) which can be easily modified according to the necessity of this work. Figure 3.17 the block diagram consists of vehicle dynamics, braking dynamics, motor, driveline and HESS.

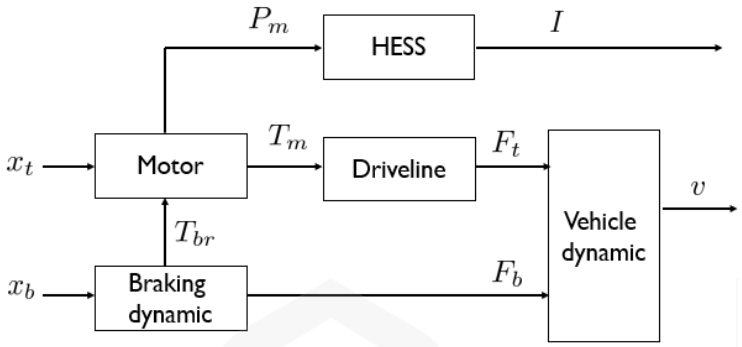

Figure 3.17 Block diagram of longitudinal dynamics of EV.

Here, x_t and x_b define the position of the acceleration pedal and brake pedal, T_{br} and T_m symbolize the braking torque and total torque to drive the car and F_t and F_b denotes the traction force and braking force. Finally, I and v are referring to the required current and vehicle speed, respectively. Noted that this current, I, is regulated by the proposed controller, and thus, it ensures that the current demand of the system accordingly.

3.7.1 Vehicle Dynamics

Vehicle dynamics consists of the motion of the body with regard to forces that are acting on it. Primarily, it deals with four different forces, such as aerodynamic drag F_a, rolling resistance F_r, grade force F_g and input tractive forces F_{tr}. By referring to Figure 3.18, the Newton's second law can be applied to calculate the acceleration and velocity of a vehicle.

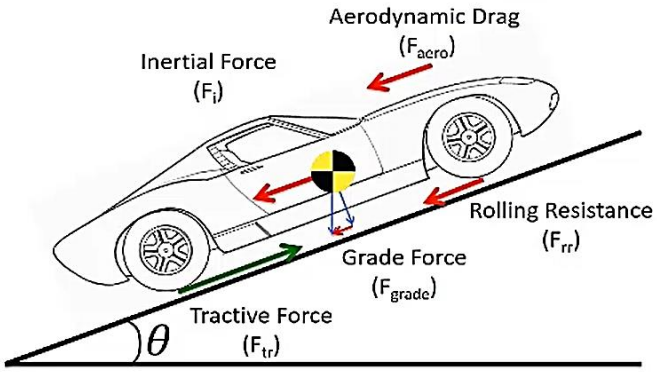

Figure 3.18 Forces acting on the vehicle body (MathWorks, 2023).

Tractive forces are required for a vehicle to move forward overcoming rest of the forces. Hence, the vehicle dynamics can be represented as:

$$F_{tr} = F_{aero} + F_i + F_{grade} + F_{rr} \tag{3.53}$$

where,

aerodynamic drag, $F_{aero} = \frac{1}{2}\rho C_d A_f V^2$,

initial force, $F_i = a \cdot m_i = 1.04 \cdot m_v \cdot a$,

grade force, $F_{grade} = m_v g \sin\theta$,

and rolling resistance, $F_{rr} = m_v g C_{rr}$.

Hence, the required acceleration for the car to move forward is

$$a_v = \frac{F_{tr} - \left(\frac{1}{2}\rho C_d A_f V^2 + m_v g \sin\theta + m_v g C_{rr}\right)}{1.04 \cdot m_v} \tag{3.54}$$

The tractive force is calculated based on the driveline dynamic, while the braking force is calculated from the brake dynamic block. Finally, the integration of equation (3.48) can help deriving the vehicle's required speed.

3.7.2 Driveline

The driveline is responsible for transferring the torque generated by a motor, T_m, to the drive wheels for generating the required tractive force to accelerate the vehicle. Since EV utilizes a motor to generate torque, τ_{motor}, no gear shifting is required since the motor can provide high torque at high angular speed. Thus, only a single gear is used in this simulation, where the gear ratio is given as G = 3.55. Nevertheless, there will be a loss in torque in real operation due to heat, friction, and other factors, which is defined as τ_{loss} in equation (3.49). The tractive force, F_{tr}, can be calculated by using this equation:

$$F_{tr} = (\tau_{motor} - \tau_{loss}) \cdot \frac{G}{r_w} - F_{Br} \tag{3.55}$$

where, r_w is the wheel radius and F_{Br} is the breaking force. This braking force is generated when the brake is pressed, and therefore, it is a type of resistive force for the vehicle to move forward.

3.7.3 Brake Model

When the brake pedal is pressed, it creates a braking force that slows the motor speed. The braking force is converted into regenerative braking torque when it is multiplied with $\frac{r_w}{G}$. Then the product of regenerative braking torque and motor rotational speed generates the energy that is stored in the battery.

3.7.4 Motor Model

The motor initially receives the acceleration-pedal position and braking-pedal position to measure the required force that should be generated according to the driver's command. Hence, it draws the required power from the ESS as per the required force and transfers it as a form of mechanical power that is considered the output of the motor. Therefore, the motor torque, τ_{motor}, and rotational speed, ω_{motor} have been considered to measure the required power as shown in equation (3.50):

$$P_{motor} = \tau_{motor} \cdot \omega_{motor} \tag{3.56}$$

During the power transformation from electric power to mechanical power, the motor has some power loss, P_{loss}. Therefore, the required power must include the power loss to make it very accurate, as discussed in (Roy, Islam, Rashid, et al., 2021; Zhang et al., 2011). To measure power loss, the system identification tool from Matlab can be utilized that consider several factors, such as motor loss constants from the reference motor (i.e., k_c, k_i, k_ω and C_{motor}), scaled base speed of the motor, ω and scaled torque, T_m. Thus, the power loss can be derived as shown in equation (3.51):

$$P_{loss} = k_c \cdot T_m^2 + k_i\omega + k_\omega\omega^3 + C_{motor} \tag{3.57}$$

Thus, the total input power, $P_{in_{motor}}$, can be calculated by adding the measured power loss, P_{loss} and the output power, P_{motor} as shown in equation (3.52):

$$P_{in_{motor}} = P_{loss} + P_{motor} \tag{3.58}$$

Table 3.6 describes the parameters and their values that have been considered for the evaluation model.

Table 3.6 Evaluation model parameters (MathWorks, 2023).

Parameters	Description	Value	Unit
ρ	Air density	1.23	kg/m^2
C_d	Drag coefficient	0.38	-
A_f	Vehicle frontal area	2.1	m^2
V	Vehicle speed	-	m/s
a_v	Vehicle acceleration	-	m/s^2
m_i	Vehicle inertial mass	2392	kg
m_v	Vehicle mass	2300	kg
g	Gravity	9.81	m/s^2
C_{rr}	Rolling resistance coefficient	0.01	-
θ	Road angle	0	° (Degree)
τ_{motor}	Motor torque	-	Nm
τ_{loss}	Torque loss	-	Nm
G	Gear multiplication	3.55	-
r_w	Wheel radius	0.34	m
ω_{motor}	Rotational speed	-	rad/s
T_m	Maximum torque of the motor to be scaled	500	Nm
ω	Base speed of the motor to be scaled		rad/s
k_c	Motor loss constant from the reference motor	0.0452	$\frac{s}{kg \cdot m^2}$
k_ω	Motor loss constant from the reference motor	5.066×10^{-5}	$kg \cdot m^2$
k_i	Motor loss constant from the reference motor	0.0167	J
C_{motor}	Motor loss constant from the reference motor	628.3	W
P_{AL}	Accessory Load	600	W

3.7.5 HESS and PMS

HESS:

HESS generates the required power, P_m to move the vehicle according to the drive cycle; hence, it incorporates the motor input power and additional load, P_{AL} which includes the inertia force etc. as shown in equation (3.53).

$$P_m = P_{in_{motor}} + P_{AL} \tag{3.59}$$

In order to make the system comprehensible, Figure 3.19 demonstrates the Simulink model of the HESS considered for the vehicle.

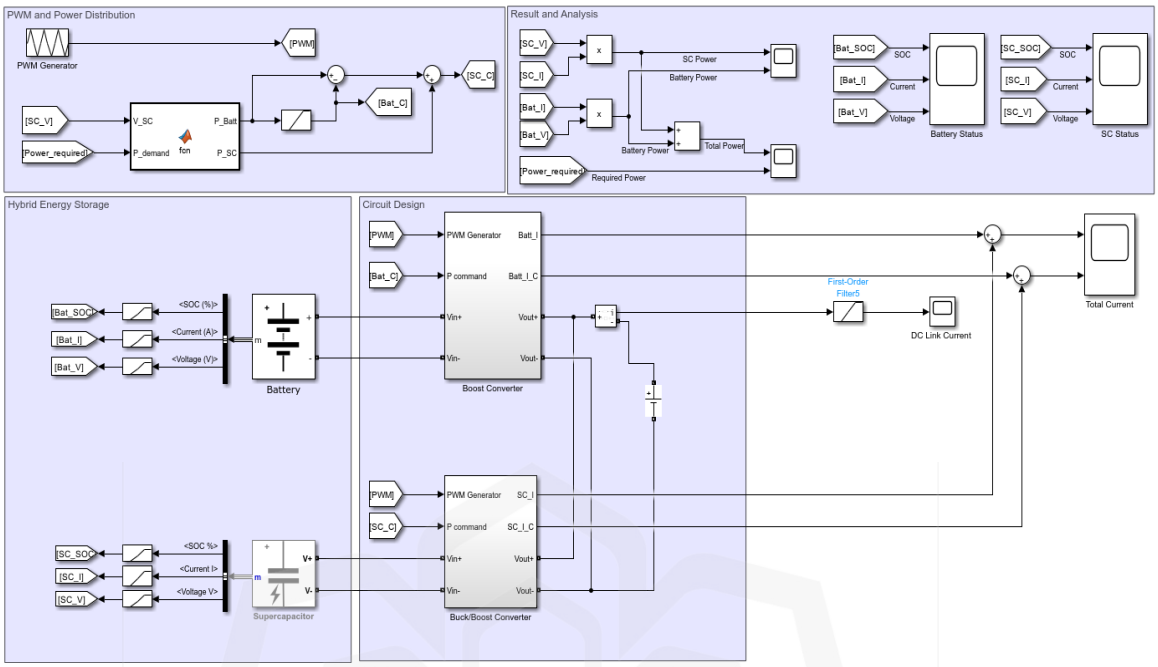

Figure 3.19 Simulink interface of the HESS Model used in the validation model.

Table 3.7 HESS component properties and power converters' parameters.

Components and their properties	Values
Battery Pack	
Rated capacity	132 Ah
Cell nominal voltage	3.3 V
No. of cell in series	60
No. of cell in parallel	1
Response time	5s
Initial SOC	100%
Supercapacitors	
Rated voltage	120 V
Initial voltage	120 V
Capacitance	1500 F
No. of parallel capacitors	1
No. of series capacitors	6
Equivalent DC series resistance	2.1 mΩ
DC Bus Voltage	350 V
Boost and Buck-Boost Converter	
Switching Frequency	40×10^{3} Hz
Inductance	1×10^{-3} H

Table 3.7 lists the power converter parameters as well as the properties of the HESS for the simulation work that represents the similar properties of other works as (Ranjan & Bodkhe, 2021).

PMS:

Due to the integration of a HESS in the proposed system, a PMS is cardinal to operate the HESS and meet the power demand accordingly. Figure 3.20 explains the PMS for the proposed HESS with a flowchart.

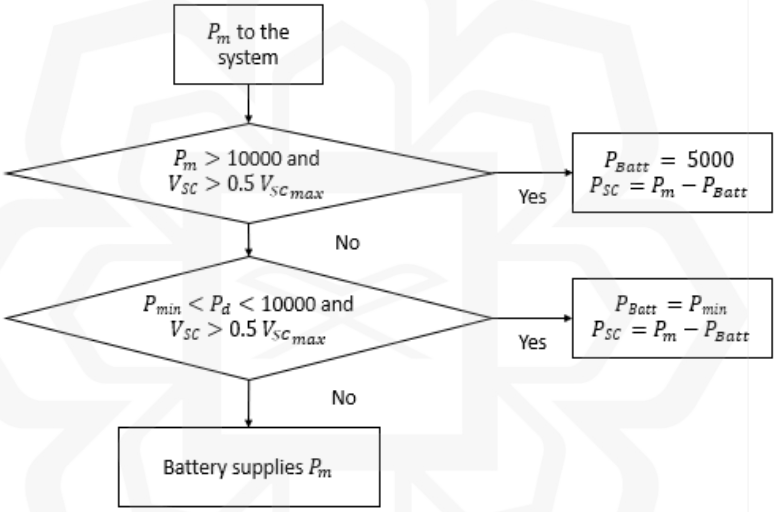

Figure 3.20 A PMS for the proposed HESS.

Figure 3.20 shows that the required power will be analyzed by the rule-based PMS if it is more than 10 kW and the SC voltage, V_{SC} is more than 50% of $V_{SC_{max}}$. If it meets the condition, battery power, P_{Batt} will assist by 5 kW, and the SC power, P_{SC}, will meet the rest of the demand. However, if the P_m is more than P_{min} (1.5kW) and below 10 kW, along with the V_{SC}, more than 50% of $V_{SC_{max}}$, P_{Batt} is set to meet P_{min} whereas P_{SC} is set to be responsible for the rest of the demand. Otherwise, P_{Batt} will be responsible for meeting the P_m.

Additionally, a first-order filter has been applied to the battery demand to ensure smooth power extraction from the battery. As a result, the filtered demand is subtracted from the battery power demand determined by the PMS, and combined with the SC power demand, also determined by the PMS.

3.7.6 Drive Cycles

This section outlines the drive cycles selected to run the evaluation model, which are widely recognized for assessing vehicle performance under various conditions. Four specific drive cycles have been considered: Highway Fuel Economy Test Cycle (HWFET), Urban Dynamometer Driving Schedule (UDDS), US06 and Federal Test Procedure (FTP). These cycles provide a comprehensive evaluation of the vehicle's performance across different driving environments.

3.7.6.1 Highway Fuel Economy Test (HWFET) Cycle

The Highway Fuel Economy Test (HWFET) cycle was developed by the U.S. Environmental Protection Agency (EPA) to assess the fuel efficiency of light-duty vehicles. Key features of the HWFET cycle include a total duration of 765 seconds, covering a distance of 10.26 miles (16.45 km), with an average speed of 77.7 km/h (48.3 mph). This test simulates highway driving conditions, characterized by steady speeds and minimal stops, making it a valuable tool for evaluating fuel economy during typical long-distance travel. It is commonly used alongside other drive cycles to provide a comprehensive assessment of a vehicle's overall efficiency (Ecopoint, 2023a).

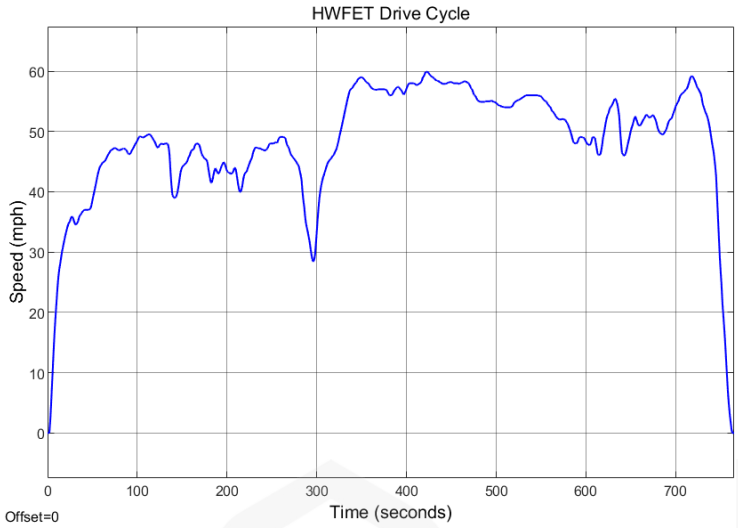

Figure 3.21 HWFET Drive Cycle.

3.7.6.2 Urban Dynamometer Driving Schedule (UDDS)

The Urban Dynamometer Driving Schedule (UDDS), also known as “the city test” or “LA4,” is designed to simulate typical city driving conditions and is primarily used for testing light-duty vehicles. This drive cycle represents an urban route covering a distance of 12.07 km (7.5 miles) with frequent stops and starts to mimic real-world traffic scenarios. The UDDS includes a maximum speed of 91.25 km/h (56.7 mph) and an average speed of 31.5 km/h (19.6 mph). Due to its stop-and-go nature, it is especially useful for evaluating a vehicle's fuel efficiency, emissions, and performance in environments where acceleration, deceleration, and idling are common. Additionally, the UDDS helps manufacturers ensure compliance with urban emissions regulations and assess the vehicle’s efficiency in short-distance driving conditions (Ecopoint, 2023b).

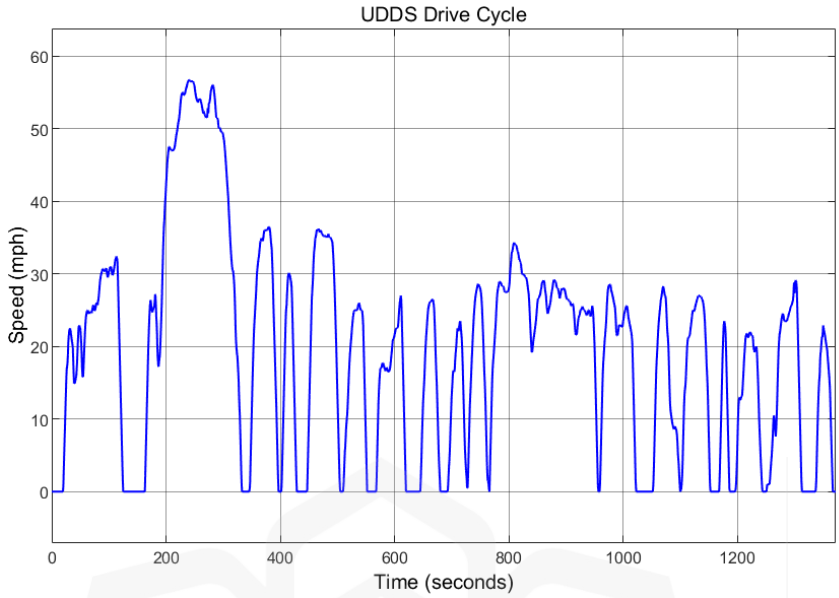

Figure 3.22 UDDS Drive Cycle.

3.7.6.3 Federal Test Procedure (FTP)

The FTP-75 is a U.S. emission certification and fuel economy test cycle for light-duty vehicles, consisting of four phases: a cold start phase (lasting 505 seconds), a stabilized phase (lasting 867 seconds), a hot soaked period (600 seconds), and a hot start phase (505 seconds). The cycle includes idling, acceleration, deceleration, and cruising to reflect typical stop-and-go traffic in cities. It measures emissions and fuel economy, with parameters like a duration of 2476 seconds, a distance of 11.04 miles (17.77 km), an average speed of 16 mph (25.8 km/h) and a maximum speed of 56.7 mph (91.2 km/h). It is part of the EPA's 5-cycle method for determining on-road fuel economy ratings considering variable vehicle speeds that simulate real-world urban driving conditions (Al-Samari, 2017).

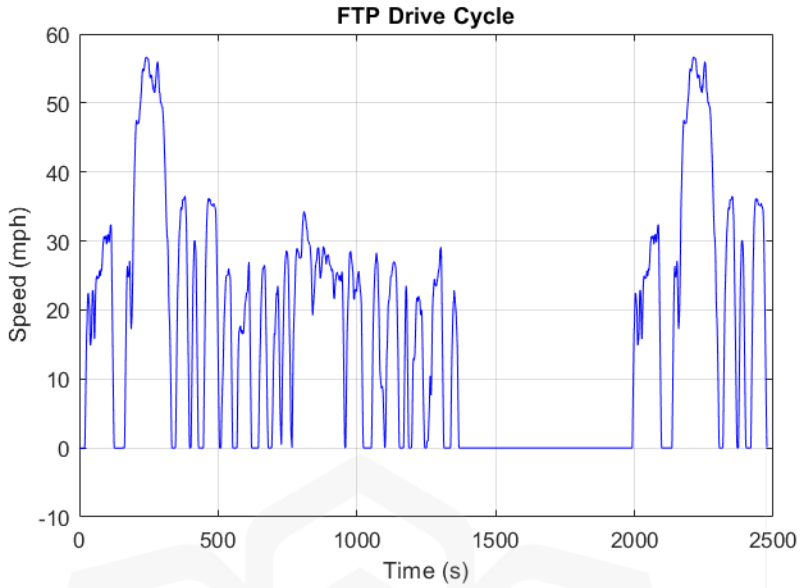

Figure 3.23 FTP Drive Cycle.

3.7.6.4 US06

In order to improve the deficiencies of another test cycle, Federal Test Procedure (FTP)-75, in terms of aggressive driving, high speed and/or high acceleration driving behaviour, fast speed fluctuations, and driving behaviour after startup, the US06 drive cycle was created. This cycle covers a distance of 8.01 miles (12.8 km), offers an average speed of 77.9 km/h or 48.4 mph, and runs for a duration of 596 seconds (DieselNet, 2023).

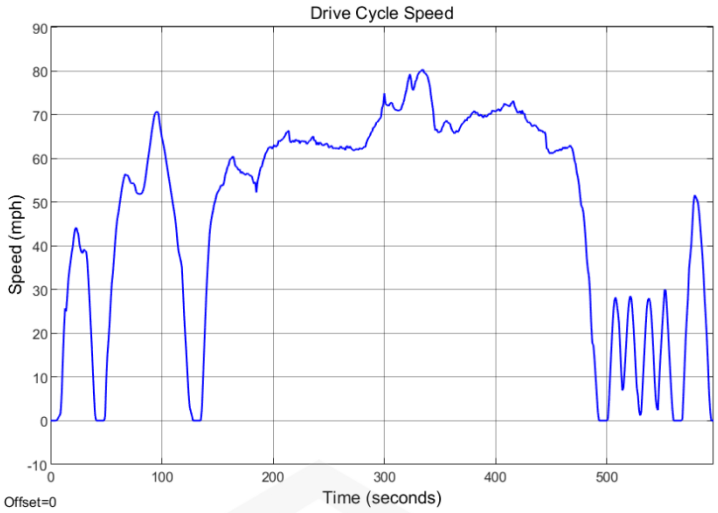

Figure 3.24 US06 Drive Cycle.

This cycle is divided into two different intervals such as:

- **US06 City** Comprises of two segments of US06 as like 1 to 130 seconds and 495 to 596 seconds.
- **US06 Highway** Interval between 130 to 495 seconds.

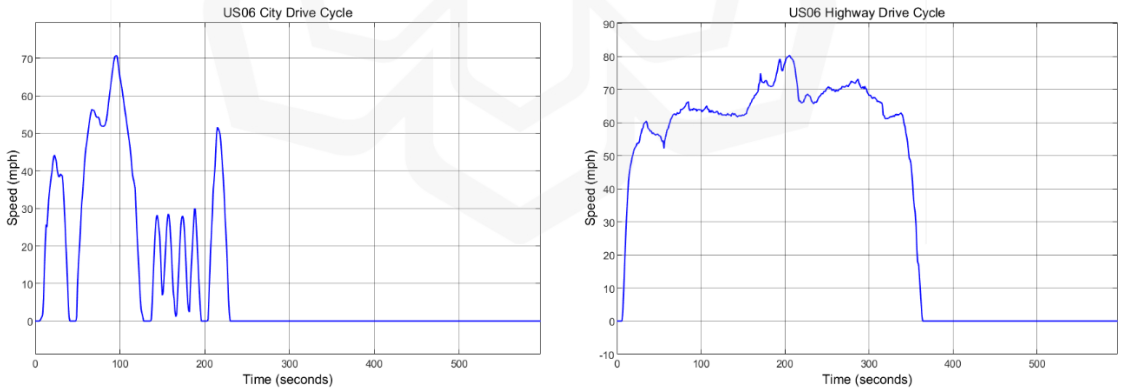

(a) (b)

Figure 3.25 (a) US06 City and (b) US06 Highway Drive Cycle.

Table 3.8 outlines different parameters of the drive cycles to offer their suitability in this application.

Table 3.8 Different drive cycles and some of their parameters.

Parameters	Drive Cycles			
	HWFET	**UDDS**	**US06**	**FTP-75**
Total Duration (s)	766	1370	596	2476
Total Distance (km)	16.5	12.07	12.8	17.77
Average Speed (km/h)	77.6	31.5	77.8	25.8
Maximum Speed (km/h)	96.5	91.2	129.2	91.2
Type of Area	Highway	Urban	Aggressive, Mixed	Urban + Suburban
Power Consumption (Wh/km)	Moderate (150 to 200)	High (200 to 300)	Very High (above 300)	Moderate (150 to 200)

3.7.7 Controller Parameters

Since the model has been changed, the parameters of the controllers should be changed in order to improve their performance. Following the heuristic approach, MRAC parameters have been updated, where PI controller parameters remain the same as discussed in Table 3.5 since the PI controller is able to ensure its best performance with the previous parameters. The parameters of the controllers for the proposed validation model have been shown in Table 3.9.

Table 3.9 Parameters of MRAC and PI controller for Validation Model.

MRAC	PI
Rate of adaptation for states, γ_x = 1.05 Rate of adaptation for reference, γ_r = 2.1155 Initial gain for states, k_{x_0} = 1 Initial gain for reference, k_{r_0} = 1	Proportional gain, k_p = 1.5 Integral gain, k_i = 1

3.8 SUMMARY

This chapter presents the methodology employed in this research, providing a structured guide for achieving the research objectives, as established by the literature review. Initially, the chapter explores the topology of a buck-boost converter and its state-space model with a battery. To meet the voltage demand of the electric vehicle (EV) motor, a proportional-integral (PI) controller is integrated into the system. Additionally, the chapter introduces the Model Reference Adaptive Control (MRAC) strategy, which is proposed to regulate the voltage according to load demand. The performance of the MRAC is compared with the PI controller in terms of root mean square error (RMSE) for voltage tracking under both disturbed and disturbance-free conditions.

Moreover, an alternative drivetrain configuration is discussed, featuring a buck-boost converter paired with a supercapacitor (SC) in a hybrid energy system (HEV). This system relies on a rule-based power management strategy (PMS) to meet the power demand of the motor. The PMS operates based on predefined thresholds: if the power demand exceeds 1.5 kW, the battery provides minimal power, with the SC supplying the remaining power. When the SC's voltage exceeds 50% of its maximum capacity, both the battery and SC share the load; otherwise, the battery alone supplies the power. Noted that the battery supplies power through a boost converter in this configuration since the regenerative braking system returns the power to the SC. As SC deals with different functionalities such as charging and discharging, the performance of the PI controller and MRAC algorithm have been compared with the configuration where the buck-boost converter plays the role of the system, and SC supplies the power according to the power demand.

During the MRAC parameter tuning process, it was observed that reducing the adaptation rate for the reference, γ_r results in more stable system behavior, with reduced sensitivity to variations in the adaptation rate for states γ_x. However, larger γ_x values, while improving adaptation speed, also increase the risk of instability, underscoring the importance of carefully selecting both γ_r and γ_x to achieve optimal system performance. After selecting the appropriate γ_r and γ_x for MRAC and and optimal gains for the PI controller, their performance was compared based on RMSE in current tracking under both disturbed and undisturbed conditions.

Finally, the chapter introduces a validation model developed by the MathWorks team, which simulates real-time EV parameters to validate the performance of the simulation model. The dynamics of the validation model are described using a block diagram and relevant equations. Moreover, the essential parameters for both the validation model and the proposed hybrid energy storage system (HESS) are discussed to ensure clarity and comprehensibility for the reader. As the HESS model is responsible for fulfilling power demands, a new rule-based PMS is also introduced alongside the model. Several drive cycles, including HWFET, FTP, UDDS, and US06, are used to test the PMS and evaluate the controllers' performance. Additionally, new controller parameters for the proposed validation model are discussed to provide a complete understanding of the system's behaviour under different operating conditions.

CHAPTER FOUR

RESULTS AND VALIDATION

4.1 INTRODUCTION

This chapter contributes to explaining the simulation results of the models designed and developed in Chapter 3. Section 4.2 analyzes the behaviour of the inverting and non-inverting BDCs through open-loop simulation. Section 4.3 extensively presents the simulation and analysis of the proposed controllers with both inverting and non-inverting BDCs. Section 4.3.1 is dedicated to analysing the simulated results where the power is extracted from the battery by controlling the voltage of the inverting BDC. Section 4.3.2 demonstrates the performance of the controllers in regulating the current through non-inverting BDC when power is distributed from the HESS, consisting of a battery pack and a supercapacitor. The presented analysis also includes the effect of unmeasured disturbances on the system in order to understand the robustness capability of the controllers. The performance is evaluated based on standard indicators such as power tracking, current tracking, voltage tracking, and control efforts. Section 4.4 validates the proposed controller by integrating and simulating it with an EV model designed by Mathworks Team, which has been modified by integrating HESS along with a PMS, BDC and the controllers. During the simulation, the EV model runs for four different standard drive cycles that significantly impact the power demand, and thus, the controller performance in tracking current, power and drive cycles can be evaluated.

4.2 OPEN LOOP SIMULATIONS

In this section, both inverting and non-inverting BDC models are run with open-loop simulation without any feedback controller since it helps to understand and validate the behaviour of a system without the influence of feedback loops. This helps diagnose potential system errors earlier, understand the system dynamics, and determine the system's response to different inputs.

4.2.1 Open-Loop Response of the Inverting BDC

Section 3.2.1 introduces an inverting BDC model with properties, and the system considers a Li-ion battery for the power of the EV. In the open-loop simulation of this system, a step response has been considered where the initial current is set to 0 A for 1s, and then the required current is set to 50 A, as shown in Figure 4.1 (a). Noted that in this case, the current at the inductor is considered as an input, while the voltage across the resistor is the output.

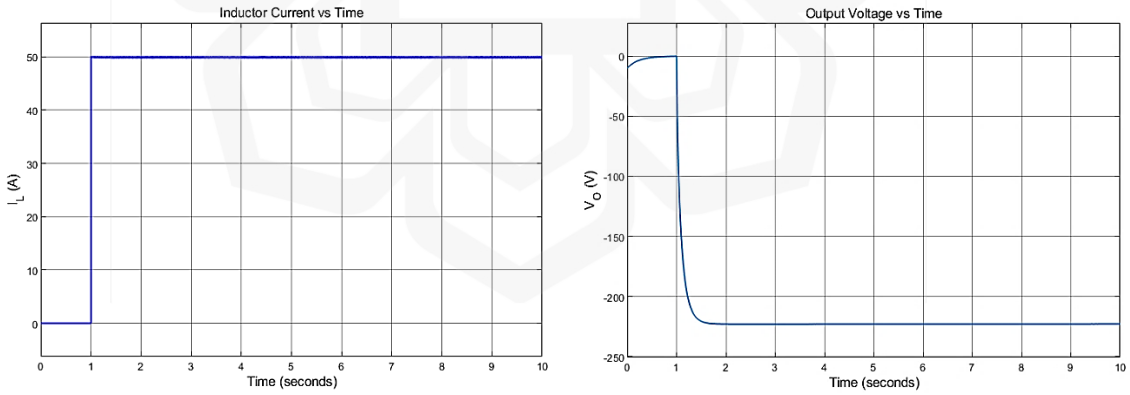

(a) (b)

Figure 4.1 (a) Input current and (b) output voltage from BDC with a battery pack.

Figure 4.1 shows the open-loop response of the BDC. Figure 4.1 (b) shows the output voltage starts from -10 V since the capacitor's initial voltage is considered 10 V.

Exponentially, it then tries to 0 V since the supplied current is 0 A. As the step response is provided as 50 A to input after 1 s, the output voltage reaches -222 V at 1.5 s. Noted that the BDC utilizes almost the complete duty ratio of the PWM signals since no controller has been considered with the system. The output voltage is monitored for 10 s and it is found as stable at -222 V which indicates its stability.

Based on the output voltage, it can be concluded that system behaves as linear system since it becomes stable at -222 V. However, due to the fluctuation of duty ratio that is regulated by the controller, the BDC starts to behave nonlinear as it is discussed in Section 3.2.1.

4.2.2 Open-Loop Response of the Non-Inverting BDC

Section 3.3.2 addresses the HESS model, including a non-inverting buck-boost converter with the SC and a boost converter with the battery pack. Since the SC power is regulated by both PI and MRAC alternatively for the purpose of comparative analysis, the open-loop simulation response is shown only for the buck-boost converter with SC.

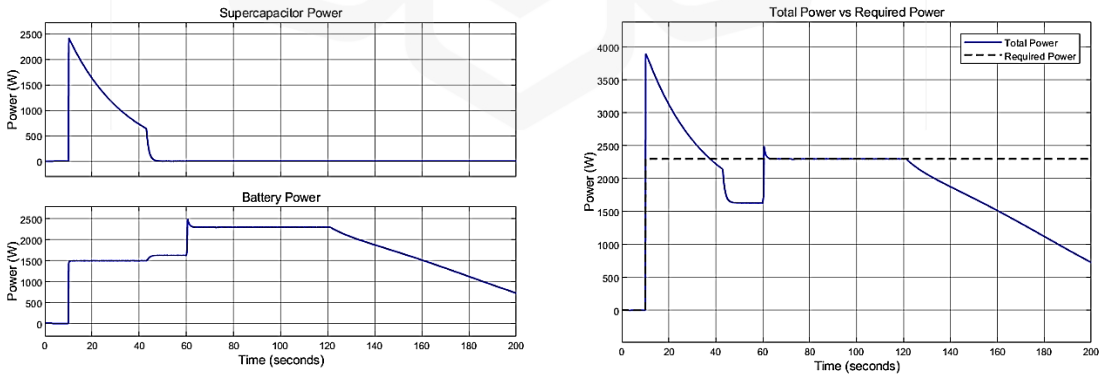

(a) (b)

Figure 4.2 (a) SC and battery power output, and (b) total power output from the open loop BDC with HESS (that receives constant power demand).

To analyze the plant's response, a unit response of 2.3 kW is introduced after 10 seconds into the simulation, which is subsequently run for a duration of 200 seconds. It is important to note that during this simulation, the PMS is active, which limits the battery pack's power supply to a maximum of 1.5 kW, while the SC is expected to replenish the system with an additional 800 W. However, as depicted in Figure 4.2 (a), the SC delivers 2.4 kW of power after 10 seconds, while the battery pack supplies 1.5 kW. Consequently, Figure 4.2 (b) illustrates that the total power delivered reaches 4.8 kW, despite the actual power demand being only 2.3 kW. This discrepancy arises because the buck-boost converter operates at the full duty cycle of the PWM in the absence of a controller, as discussed in Section 4.2.1, leading to its complete discharge within 35 seconds, as shown in Figure 4.2 (a). Around 45 seconds into the simulation, when the SC can no longer support the required power, the battery pack compensates for the deficit. By approximately 60 seconds, when the SC is fully discharged and unable to supply further power, the battery pack maintains a continuous power supply to meet the demand. Crucially, the boost converter extracting power from the battery pack is regulated by a PI controller, ensuring that the power supply aligns with the power demand.

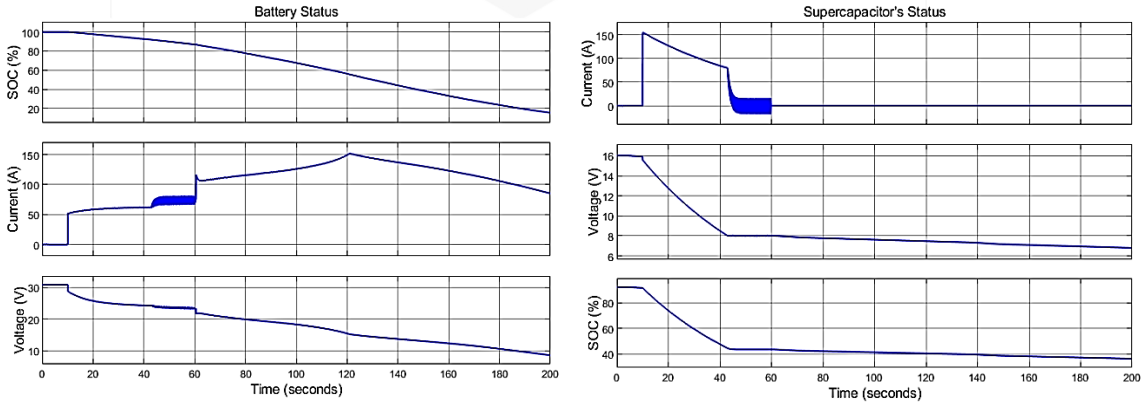

(a) (b)

Figure 4.3 (a) Battery and (b) SC status in the open loop BDC with HESS (that receives constant power demand).

Meanwhile, Figure 4.3 (a) and (b) illustrate the current, State of Charge (SOC), and voltage profiles of the battery and SC during the transient period, providing insight into their operational dynamics. For instance, starting at 10 seconds, the current drawn from the battery progressively increases as the battery voltage declines due to discharge, as depicted in Figure 4.3 (a). Conversely, the SC experiences a rapid decrease in both voltage and current due to an uncontrolled power supply, leading to near depletion within 35 seconds. It is noteworthy that the battery pack is unable to sustain a 2.3 kW power output beyond 120 seconds, as both current and voltage decrease concurrently due to the depletion of battery charge, as shown in Figure 4.2 (a) and Figure 4.3 (a).

This open-loop simulation highlights that the buck-boost converter extracts power from the ESSs at an almost maximal duty cycle when unregulated by any controller. Notably, the SC continues to provide power without restriction, indicating the system's nonlinearity. Despite the system's behaviour aligning with the linear model described in Section 3.2.2, the variation in the duty cycle introduces nonlinear characteristics into the system.

4.3 SYSTEM RESPONSES WITH THE CONTROLLERS

This section presents a comparative analysis of the performance of two control strategies—PI and MRAC—when applied to the systems, such as inverting and non-inverting BDC. Therefore, a few performance indicators have been considered that will be explained in the next sub-section.

4.3.1 Simulation Results of Inverting BDC

This section is dedicated to analyze the performance of the controllers with the inverting BDC, as discussed in Section 3.2.1 based on performance indexes such as voltage tracking accuracy, control effort and controller characteristics. In addition, the performance of the controllers has been evaluated when the system is affected by the disturbance to evaluate their suitability in real-life applications.

4.3.1.1 Fixed Voltage Tracking

Figure 4.4 presents the output voltage from the BDC, V_O, during the transient period of 2 seconds when the system receives a command to track 100 V with the help of the controllers. Noted that due to its being an inverting BDC, it changes the polarity of the voltage from positive to negative and vice-versa. Here, BDC responses with PI control and MRAC strategies are shown in a blue dashed line and a red dash-dotted line, respectively. The reference trajectory is labelled as “Desired” with a black line in the graph. In this figure, the MRAC-regulated responses are denoted as DMRAC, representing the Direct Model Reference Adaptive Control algorithm since in this MRAC strategy, control law is directly manipulated by the adjustment mechanism.

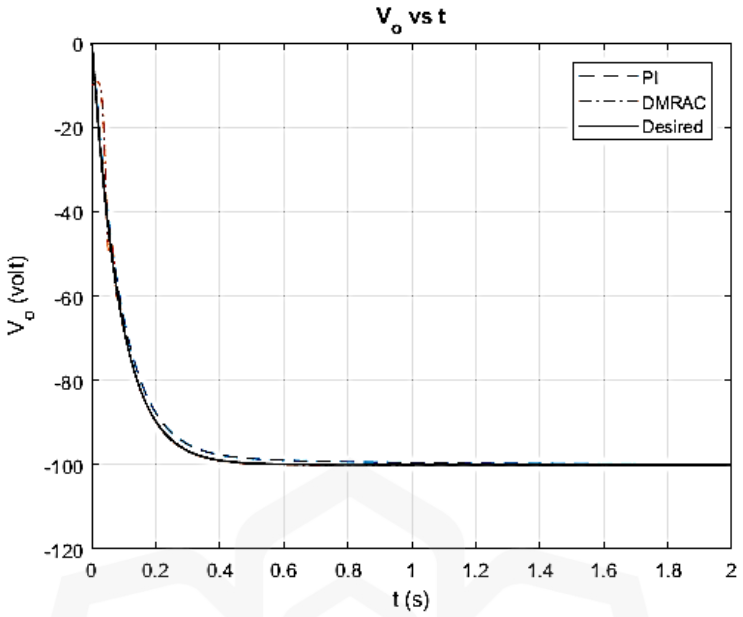

(a)

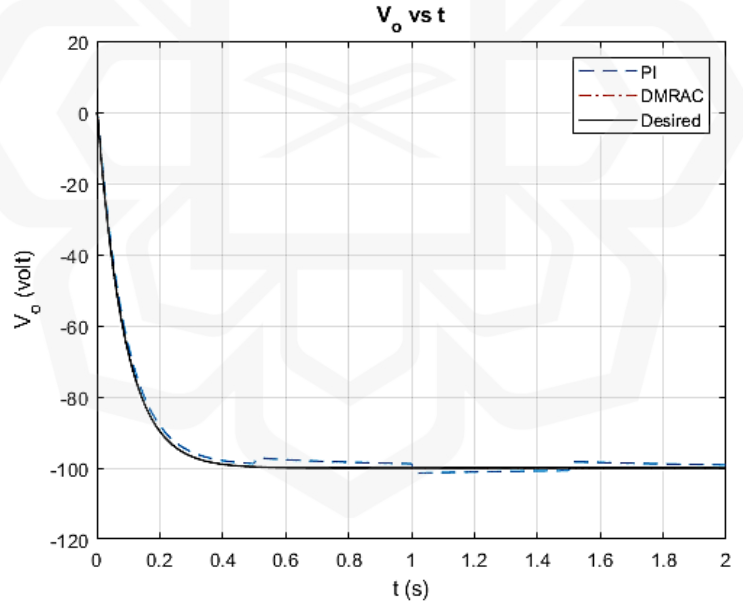

(b)

Figure 4.4 Constant voltage tracking (a) in the absence of disturbance and (b) in the presence of disturbance.

Figure 4.4 (a) portrays that both the PI and MRAC are able to track the voltage as per the reference when the system is free from any disturbances. However, MRAC supersedes PI in terms of its accuracy, and hence, no gap is vividly visible between the reference and MRAC responses. In addition, Figure 4.4 (b) shows that in the presence of disturbance to the system, PI-controlled response appears with some small fluctuations (of below ± 5% overshoot) during tracking, while MRAC maintains almost similar accuracy in the presence of disturbances. To consider the disturbance to the system, white Gaussian noise of 20 W noise power and 0.5 s sample time has been applied to the controller output for every 5 s.

4.3.1.2 Variable Voltage Tracking

In real-life applications, EV voltage demand changes according to the driving modes. Hence, a load demand trajectory is proposed based on variable voltage, which varies with respect to time. Figure 4.5 displays the output voltage, V_O, from the BDC along with the reference voltage, V_{ref}, for a 2-second transient period as the system tracks the load demand using PI and MRAC controllers. Thus, Figure 4.5 explains the load demand trajectory where voltage demand increases from 0 V to -100 V within 0.7 s to represent the acceleration mode and immediately drops at -55 V within 0.5 s which introduces the braking mode. Then, for a 0.2 s period, the voltage demand remained constant and then immediately dropped down again to make the car stop completely within a 0.5 s period. Therefore, this trajectory describes the three driving modes, such as acceleration mode, steady-state mode and breaking mode to analyze the controllers' performance in tracking the voltage. The BDC responses under PI control and MRAC algorithms are represented

by the blue dashed line and red dash-dotted line, respectively, with the reference trajectory labelled "Desired" shown as a black line.

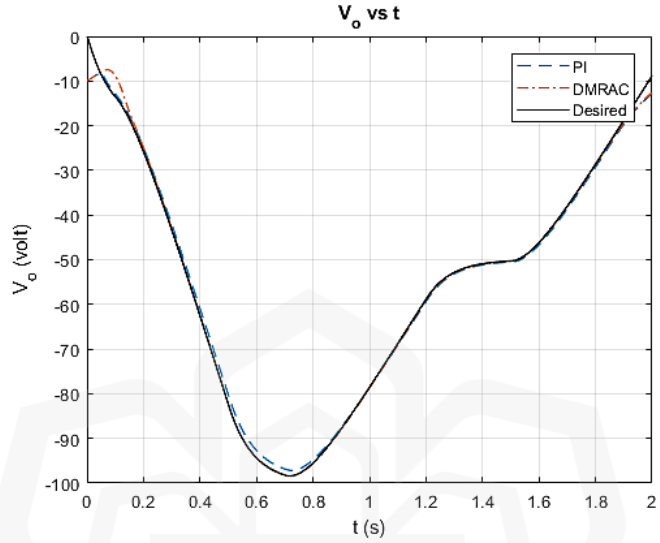

(a)

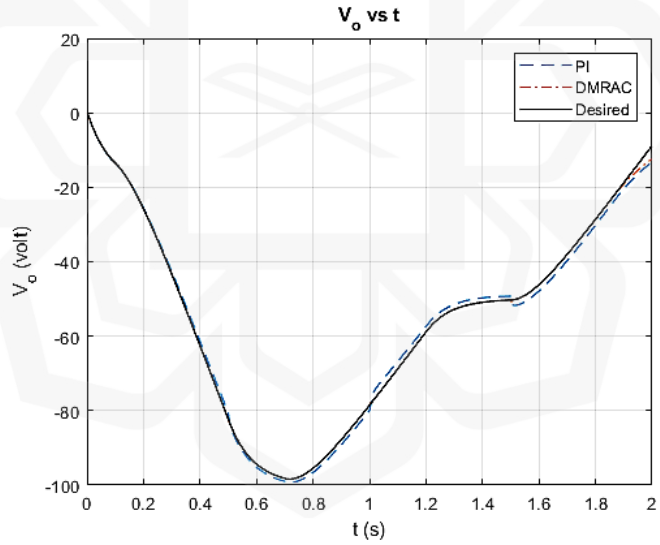

(b)

Figure 4.5 Variable voltage tracking (a) in the absence of disturbance and (b) in the presence of disturbance in the system.

Figure 4.5 (a) illustrates the variable voltage tracking of the BDC under disturbance-free conditions, comparing the performance of PI and MRAC-controlled systems. The PI controller exhibits some deviations, especially during the acceleration mode of trajectory tracking, whereas the MRAC-controlled system shows higher accuracy, and thus, no gap

is vividly visible between the reference and MRAC responses. Similarly, Figure 4.6 (b) shows the impact of disturbances on the performance of both controllers, with the PI-controlled system deviating more than the MRAC-controlled system, which appears during the steady-state and braking mode. Noted that the system is introduced with the same disturbance that has been discussed in Section 4.3.1.1.

4.3.1.3 Control Effort during Fixed Voltage Tracking

Figure 4.6 illustrates the system input, specifically the inductor current, under both disturbance-free and disturbed conditions. The inductor current responses from the MRAC and PI control algorithms are represented by the blue dashed line and the red dash-dotted line, respectively. Figure 4.6 (a) indicates that the MRAC algorithm demands a higher control effort compared to the PI controller to maintain the constant voltage, as evidenced by a 3.3% higher overshoot in the inductor current. Figure 4.6 (b) exhibits a similar pattern, where the MRAC algorithm continues to exert greater control effort—approximately 3.3% more—compared to the PI controller, as seen in Figure 4.6 (a). It is important to note that the allowable overshoot limit is set to a ±5% variation.

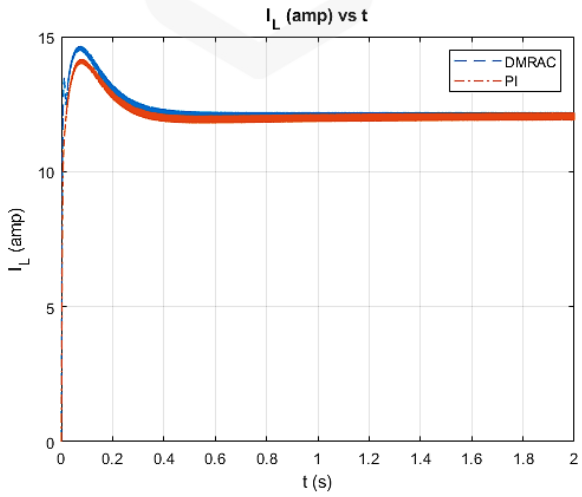

(a)

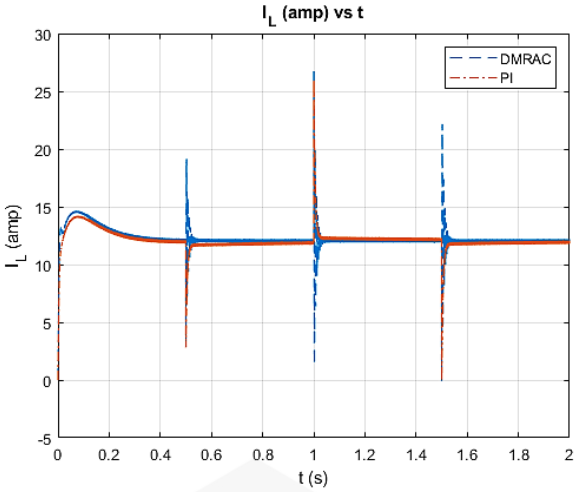

(b)

Figure 4.6 Inductor current (a) without the disturbance and (b) in the presence of the disturbance in constant voltage tracking.

4.3.1.4 Control Effort during Variable Voltage Tracking

Similar to Section 4.3.1.3, the inductor current is monitored when the BDC tracks the variable voltage with the help of the controllers. In Figure 4.7, the inductor current responses from the MRAC and PI control algorithms are represented by the blue dashed line and the red dash-dotted line, respectively. Figure 4.7 (a) shows that both PI and MRAC-controlled responses show similar traits when the system tracks the load demand, and their difference is significantly minute, below 3%. Figure 4.7 (b) describes the controlled system responses with disturbances during variable voltage tracking. Since the same disturbance has been considered in this scenario, discussed in Section 4.3.1.1, the disturbances appear in the system input every 0.5 s, as shown in Figure 4.7 (b). Notably, despite the presence of disturbances, the control efforts of both controllers display no significant differences, with their responses nearly aligning with each other. This suggests that the controllers do not show any comparable performance under these conditions.

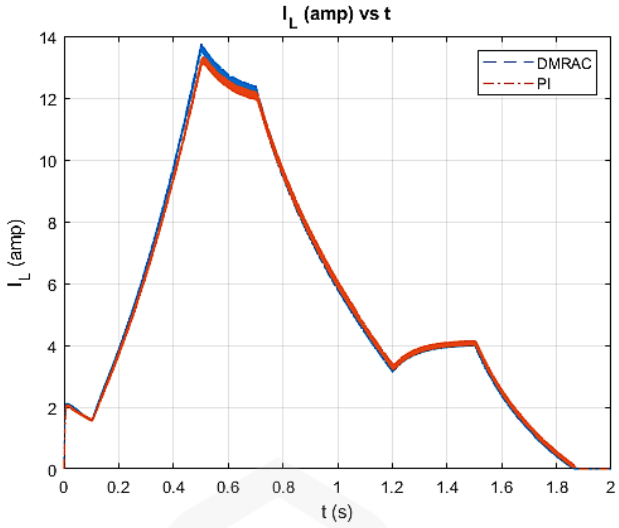

(a)

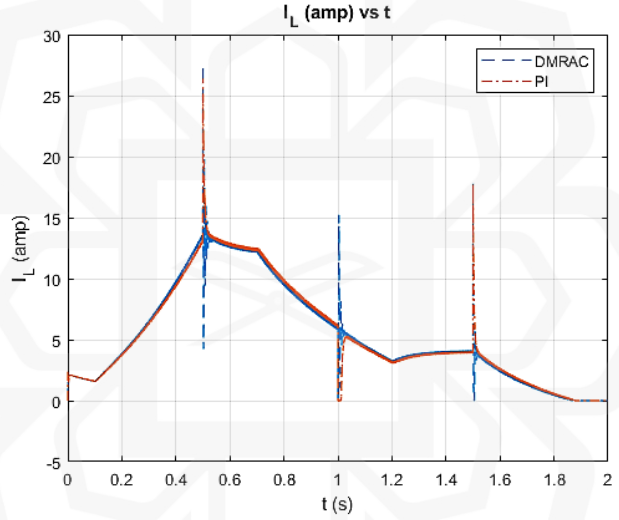

(b)

Figure 4.7 Inductor current (a) without the disturbance and (b) in the presence of the disturbance in the system during variable voltage tracking.

4.3.1.5 Quantitative Analysis

To quantitatively evaluate the performance of both controllers, the Root Mean Square Error (RMSE) method is utilized. This method offers a detailed assessment of the controllers' effectiveness by measuring the discrepancy between the desired and actual trajectories at each time step. RMSE provides a comprehensive metric that reflects the average error

magnitude throughout the tracking period, allowing for a direct comparison of how accurately each controller follows the desired trajectory.

A lower RMSE value indicates a closer alignment with the desired trajectory, suggesting superior performance. In contrast, a higher RMSE value denotes greater deviations from the target path, indicating reduced accuracy and less effective control. Therefore, RMSE analysis enables the identification of the controller that achieves greater precision and stability in tracking the desired output. RMSE can be demonstrated as the following equation (Islam et al., 2019):

$$RMSE = \sqrt{\frac{\sum(y_a - y_d)^2}{length\ of\ y}} \tag{4.1}$$

where y_a represents the actual values of y, and y_d symbolizes the desired values of y.

Table 4.1 RMSE of MRAC and PI controllers in different cases.

Cases	RMSE of the Controllers	
	MRAC	**PI**
Constant voltage	**0.04**	0.98
Constant voltage with disturbance	**0.05**	1.53
Variable voltage	**0.43**	0.97
Variable voltage with disturbance	**0.43**	1.41

Table 4.1 presents a comparative analysis of the RMSE percentages for MRAC and PI controllers with the BDC in voltage tracking under the four different cases that have been discussed in Section 4.3.1.1 and 4.3.1.2 such as constant voltage, constant voltage with disturbance, variable voltage, and variable voltage with disturbance.

For the case of constant voltage tracking, the MRAC controller achieves an RMSE of 0.04, indicating perfect tracking with no deviation from the desired trajectory, while the

PI controller exhibits a slight error of 0.98. Similarly, during constant voltage tracking in the presence of disturbance in the system, MRAC maintains an RMSE of 0.05, demonstrating its robustness to disturbances. In contrast, the PI controller's RMSE increases to 1.53, reflecting its accuracy reduced to 36% in the presence of disturbances.

When the load demand is variable, the MRAC controller shows a minimal RMSE of 0.43, while the PI controller records a higher RMSE of 0.97, indicating that MRAC provides better tracking performance under changing conditions. In the final scenario, with variable load demand and disturbed system, the MRAC algorithm again maintains an RMSE of 0.43, while the PI controller's RMSE increases to 1.41, implying worse performance under these conditions but still inferior to MRAC. Overall, the table highlights MRAC's superior performance across all scenarios, particularly its ability to handle disturbances and maintain low RMSE values.

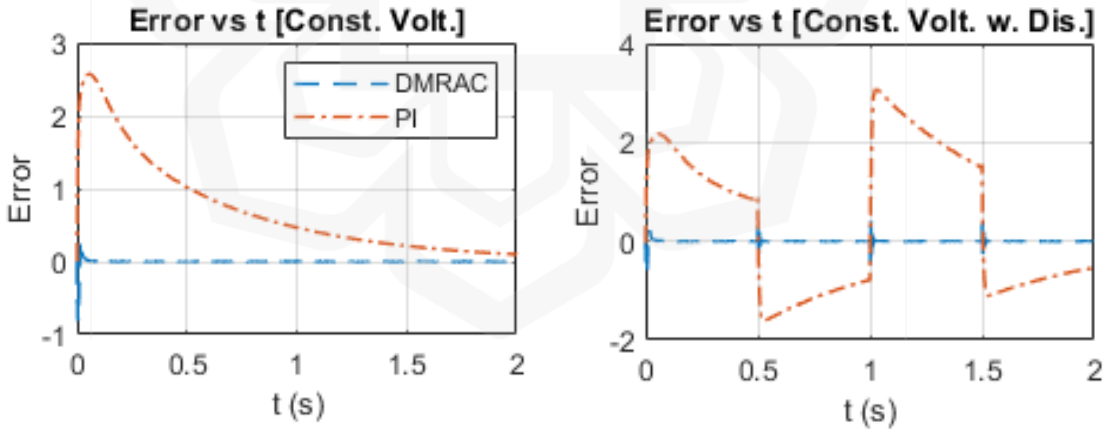

(a) (b)

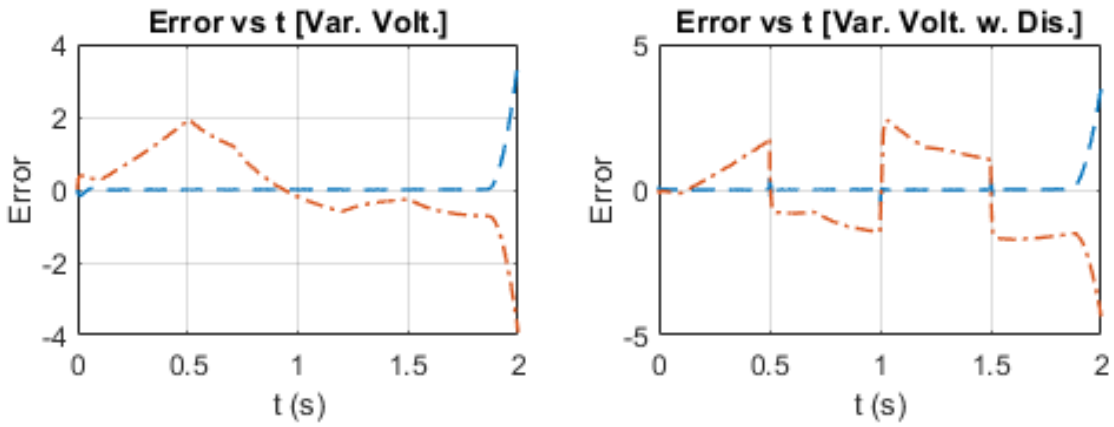

(c) (d)

Figure 4.8 Controllers' error at (a) constant voltage, (b) constant voltage with disturbance, (c) variable voltage and (d) variable voltage with disturbance.

Figure 4.8 provides the plots of tracking errors for each controller in the four different cases. Each graph shows error versus time for both controllers, with distinct scenarios: (a) constant voltage, (b) constant voltage with disturbance, (c) variable voltage, and (d) variable voltage with disturbance.

In the first scenario, as shown in Figure 4.8 (a), where the load demand is a constant voltage, both controllers effectively reduce the error over time, but the MRAC stabilizes the error faster with minimal oscillations, while the PI controller exhibits a slight overshoot before converging. In the presence of disturbances with constant voltage, as demonstrated in Figure 4.8 (b), MRAC maintains a nearly steady error close to zero, indicating strong disturbance rejection, while the PI controller shows periodic fluctuations in error. In addition, when the voltage varies, as portrayed in Figure 4.8 (c), MRAC consistently holds the error close to zero, albeit with minor fluctuations towards the end, whereas the PI controller experiences significant oscillations, particularly at the onset. Finally, in the most challenging scenario, as shown in Figure 4.8 (d), involving variable voltage with disturbances, MRAC demonstrates superior robustness, keeping the error within a narrow

band, while the PI controller shows pronounced oscillations and struggles to stabilize the error. Overall, these graphs indicate that MRAC outperforms PI in terms of stability and robustness, particularly under varying conditions and disturbances.

4.3.1.6 Controllers' Properties

Figure 4.9 visualizes the responses of the controllers to offer their characteristics with a unit response. In addition, Table 4.2 has been shared to analyze the characteristics quantitatively.

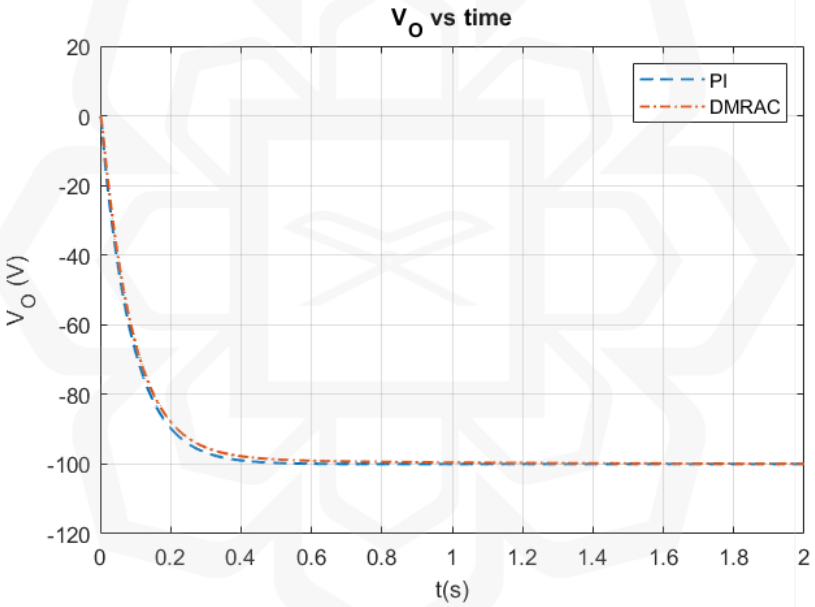

Figure 4.9 Controllers' responses on unit load demand.

Table 4.2 Controllers' characteristics for both MRAC and PI controllers.

Properties	**Controllers**	
	MRAC	**PI**
Settling time (s)	0.41	**0.34**
Overshoot (%)	0.0	0.0
Rise time (s)	0.2	**0.19**
Peak time (s)	2	**1.5**

Table 4.2 compares the performance of two control systems, MRAC and PI control, with BDC. The analysis shows that both controllers deliver almost similar performance across key dynamic properties. The settling time, which indicates how quickly the system stabilizes, is slightly longer for MRAC at 0.41 seconds compared to PI's 0.34 seconds, a negligible difference. Both controllers exhibit zero overshoot, meaning they reach the desired value without exceeding it, highlighting their stability. The rise time is nearly identical, with MRAC at 0.2 seconds and PI at 0.19 seconds, showing comparable responsiveness. The peak time, or the time to reach the maximum value, is also very close, with MRAC at 2 seconds and PI at 1.5 seconds. These results suggest that MRAC performs almost on par with PI, offering a reliable and stable control solution with only slight differences in timing metrics.

4.3.2 Simulation Results of Non-Inverting BDC

The proposed non-inverting BDC, a buck-boost converter, as discussed in Section 3.2.2, extracts power from the SC. Importantly, only the SC current is being controlled with the help of controllers since the SC is the auxiliary ESS and is responsible for supporting the power demand after a threshold. Hence, this section contributes to analyzing the performance of MRAC and PI control strategies in regulating SC current with the non-inverting BDC, based on several performance indexes such as (i) controllers' characteristics, (ii) SC current and total power tracking in a disturbance-free system, (iii) SC current and total power tracking in the presence of disturbances, and (iv) control efforts.

4.3.2.1 Controllers' Properties

To understand the controllers' characteristics, a unit response of 2.3 kW has been set as the load demand in two different environments of the system: (i) disturbed and (ii) non-disturbed. Noted that to create a disturbed system, the same disturbances have been introduced with this system, as discussed in Section 4.3.1.1. Figure 4.10 shows the disturbance to the system during the unit response load demand tracking of the controllers. This figure shows that the added disturbance changes continuously, which makes the current tracking challenging for the controllers.

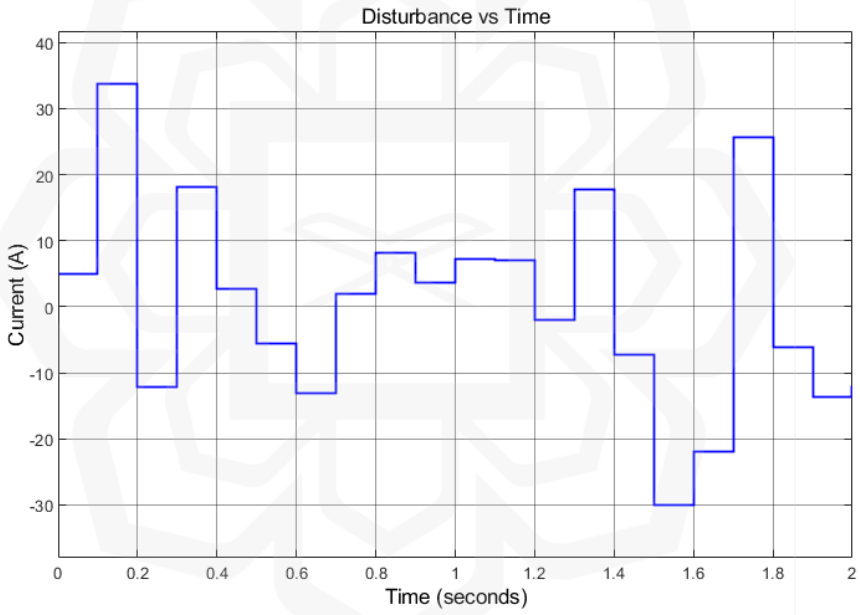

Figure 4.10 Disturbance to the non-inverting BDC.

Figure 4.11 demonstrates the SC current tracking of the controllers for 2 s where the reference, MRAC-controlled, and PI-controlled currents are shown in the blue, red dashed and yellow dash-dotted lines. In Figure 4.11 (a), both MRAC and PI show their efficacy with similar accuracies in tracking the constant SC current with a view to ensuring 800 W power from the SC. In contrast, Figure 4.11 (b) shows a significant deviation in PI-

controlled SC current tracking, whereas MRAC maintains stability in ensuring 50 A continuously with minor spikes. Hence, to understand the controllers' performance, their characteristics can be analyzed from a step response perspective and thus, Table 4.3 has been introduced.

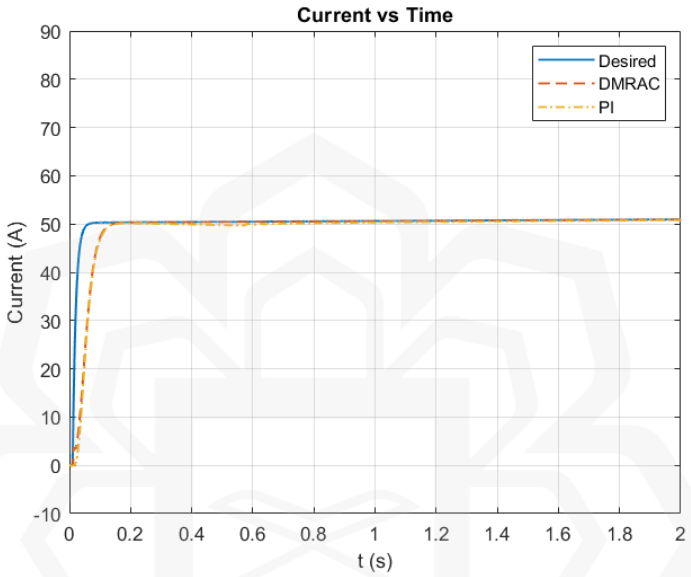

(a)

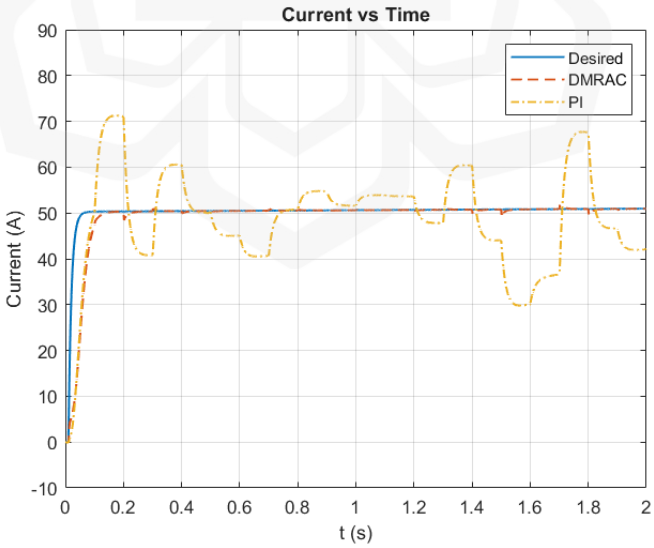

(b)

Figure 4.11 SC Current tracking in (a) disturbance-free and (b) disturbed system.

Table 4.3 explains the performance of MRAC and PI controllers under disturbed and disturbance-free conditions, which is compared based on several criteria: settling time, rise time, peak time, overshoot, and undershoot. In the disturbed BDC, MRAC shows better performance in a settling time of 1.8 s and overshoot of 1.62% compared to the PI controller with a settling time of 1.92 s and overshoot of 69.16%, suggesting a quicker and more stable response. However, it has a higher peak time of 1.7 s and a rise time of 0.07 s, which indicates a delay in reaching the maximum response. In this aspect, PI is found faster in reaching the maximum step response. Along with the higher overshoot, PI exhibits higher undershoot, which indicates instability and a higher risk of system oscillation under disturbance. Subsequently, MRAC outperforms PI in terms of settling time (0.14s vs. 0.58s), while in terms of rise time, peak time, overshoot and undershoot, they show almost the same performance, especially when the non-inverting BDC is free from any disturbance. Therefore, MRAC generally provides more stability and adaptability, especially under disturbances, while PI is faster in reaching peak time but prone to overshoot and instability in disturbed conditions.

Table 4.3 Controllers characteristics.

Properties	**Controllers with disturbed BDC**		**Controllers with disturbance-free BDC**	
	MRAC	**PI**	**MRAC**	**PI**
Settling Time (s)	**1.8**	1.92	**0.14**	0.58
Rise Time (s)	0.07	**0.04**	0.07	**0.06**
Peak Time (s)	1.7	**0.17**	1.99	**1.98**
Overshoot (%)	**1.62**	69.16	0.03	**0.02**
Undershoot (%)	**0.27**	0.32	0.27	0.27

4.3.2.2 SC Current and Total Power Tracking in the Disturbance-Free System

In order to estimate the suitability of the controllers, a power demand trajectory has been introduced where power demand changes with respect to time. Hence, this power demand trajectory requires the contribution from both the battery pack and SC, where the battery pack is delimited at 1.5 kW by the PMS and thus, the rest of the power demand must be fulfilled by the SC.

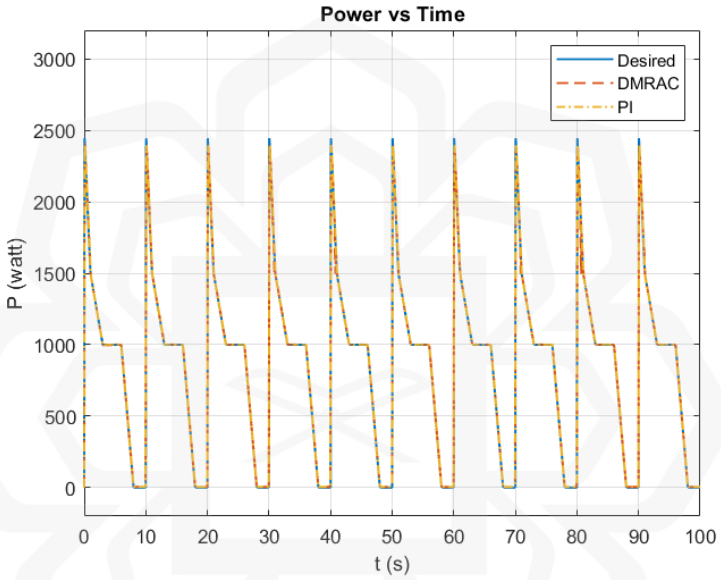

(a)

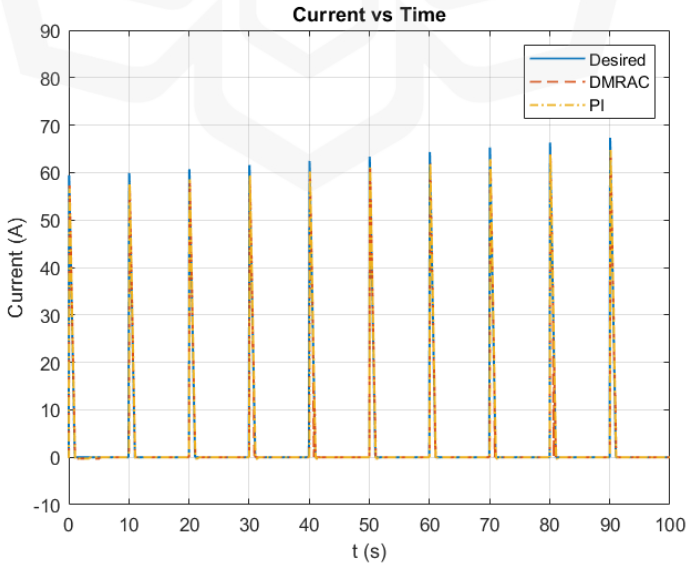

(b)

Figure 4.12 (a) Total power and (a) SC current tracking in the absence of the disturbance.

Figure 4.12 (a) describes the trajectory of the power demand that initially starts at 2.44 kW, which defines the acceleration mode of the vehicle. After 1 s, the power drops to 1.51 kW, and then, at 3 s, it drops to 1 kW, and thus, this power demand trajectory includes the vehicle's braking mode. It remains at 1 kW for 3 s, which defines the steady mode of driving. Then the power demand drops from 1 kW to 0 kW by 2s and remains there for another 2 s. Thus, this power demand trajectory of 10 s includes all three modes that have been explained earlier. Noted that the simulation is run for 100 s and thus, Figure 4.12 (a) demonstrates 10 cycles of the trajectory as explained. Importantly, the current demand changes according to the power demand, as shown in Figure 4.12 (b). This current demand increases with respect to time while power demand repeats every 10 s during the simulation. Therefore, it explains that the voltage drops in the SC due to its discharge, leading to its depletion, which requires the increment of current demand to support the power demand. Hence, the current demand starts from 60 A at 0.1 s, and finally, it reaches 67 A at 90 s, as shown in Figure 4.12 (b), while the initial power demand is set at 2.44 kW at 0.1 s and remains the same at 90.1 s, as shown in Figure 4.12 (b). This depletion of the SC also implies the continuous decrease of SC’s SOC, as shown in Figure 4.13.

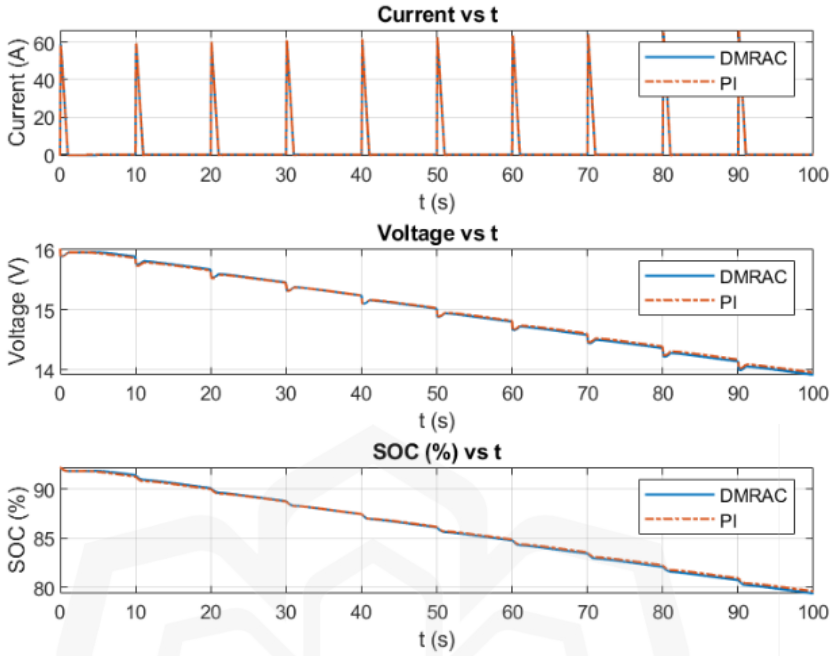

Figure 4.13 SC status in the disturbance-free system.

During the simulation, both the controllers show promising performance in tracking the current demand, and thus, they manage to meet the power demand as well. In order to understand the performance of the controllers, the transient response between 40 s and 40.3 s has been zoomed in, as shown in Figure 4.14. This figure shows that both controllers have failed to track the current accurately, though they maintain precision in tracking, and thus, any significant discrepancies have not been noticed between the controllers' response in tracking the desired current. Therefore, to understand their accuracy in tracking during the complete trajectory of 100 s, a qualitative analysis should be performed, and in that case, RMSE can be considered as one of the options.

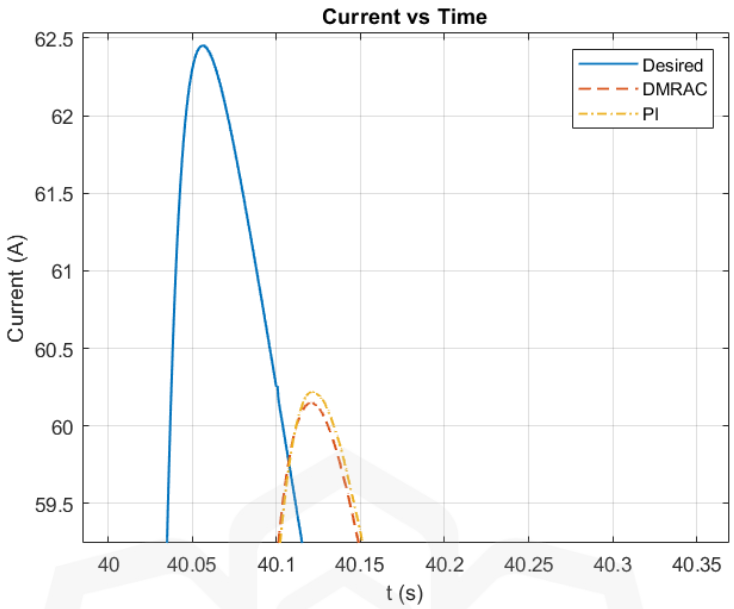

Figure 4.14 Transient response between 40 s and 40.3 s in the absence of the disturbance to the non-inverting BDC.

4.3.2.3 SC Current and Total Power Tracking in the Presence of Disturbance to the System

This section is dedicated to explaining the controller's performance when the BDC is introduced to disturbance. Therefore, the same power demand trajectory for 100 s, as discussed in Section 4.3.2.2, has been considered for the BDC to meet utilizing the MRAC and PI control strategies in the presence of the disturbance. Figure 4.15 portrays the disturbance that has been considered with the BDC, primarily affecting the SC current.

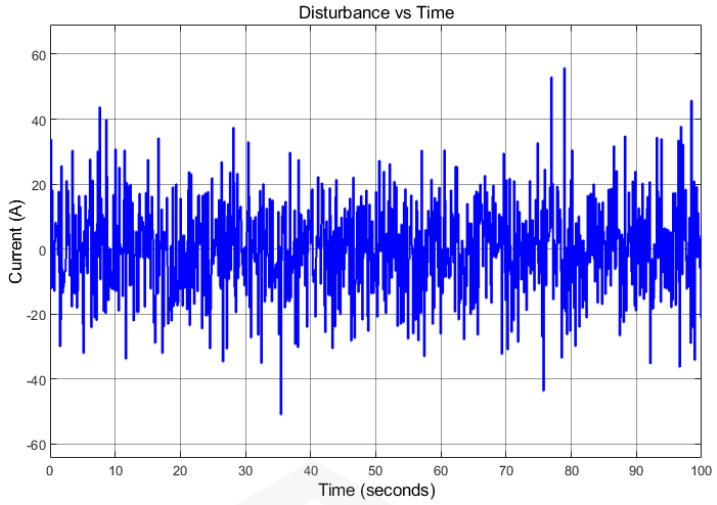

Figure 4.15 Disturbance to the power demand trajectory.

Figure 4.16 shows the controllers' power and SC current tracking when the disturbance affects the system. Between MRAC (the red dashed line) and PI (the yellow dash-dotted line) control strategies, MRAC shows more accuracy in tracking the power, as shown in Figure 4.16 (a). It indicates that MRAC outperforms PI controller during the current tracking, as illustrated in Figure 4.16 (b).

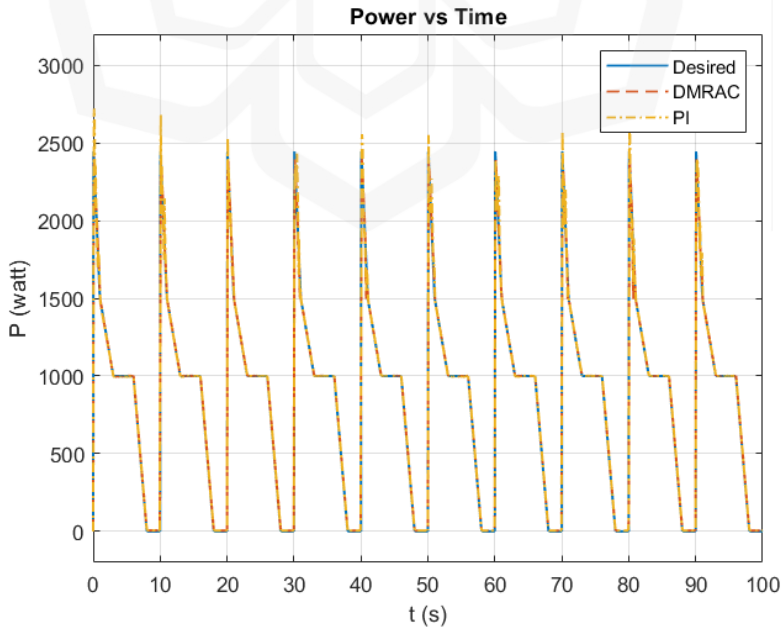

(a)

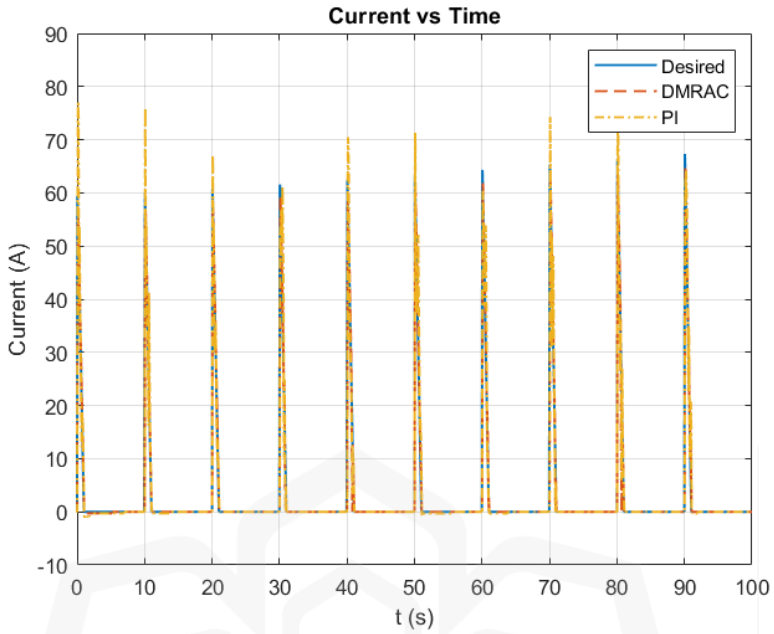

(b)

Figure 4.16 (a) Total power and (b) SC current tracking in the presence of disturbance.

To understand their inaccuracies during the tracking of SC current in presence of system disturbance, a transient response between 40 s and 40.4 s has been shown, as portrayed in Figure 4.17. The desired current, shown as the blue line, peaks at around 63 A. The MRAC tracks the desired current with better precision compared to the PI controller. While MRAC overshoots slightly, it stabilizes more quickly, maintaining closer proximity to the desired value after the peak. The PI controller, however, exhibits a significant overshoot, reaching over 70 A, far exceeding the desired current. This larger overshoot is followed by a slower decay, showing that the PI controller struggles with stability and takes longer to settle. Hence, it demonstrates that the MRAC provides superior control in tracking the desired current with minimal deviation, faster settling, and reduced overshoot compared to the PI controller. The PI controller's large overshoot suggests it may introduce higher energy consumption and instability in practical applications, especially under disturbance. In contrast, MRAC adapts more effectively to achieve a smoother, more

stable response, making it more suitable for systems where precision and stability are critical.

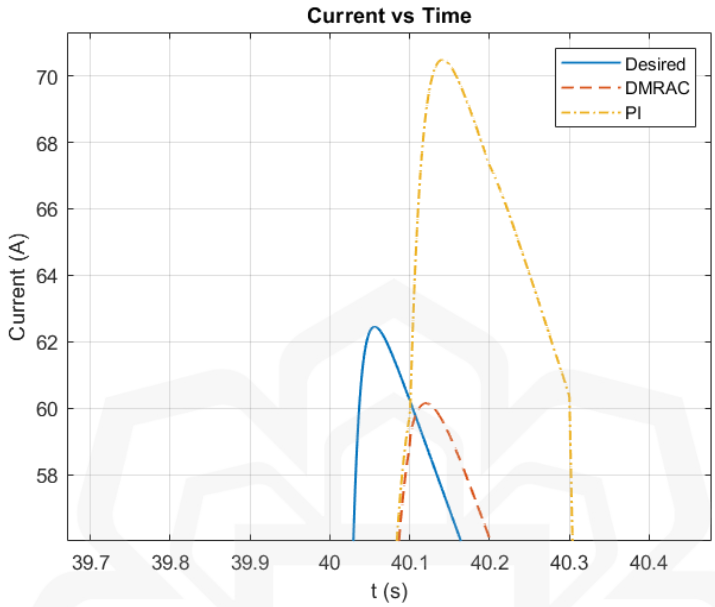

Figure 4.17 Transient response between 40 s and 40.4 s in the presence of disturbance.

4.3.2.4 Qualitative Analysis

Similar to Section 4.3.1.5, the performance of the controllers can be evaluated based on the RMSE of SC current and total power tracking when the system is free from any disturbance and influenced by disturbances. Hence, Table 4.4 has been introduced to outline the performance of the controllers based on RMSE.

Table 4.4 RMSE of MRAC and PI controllers in different scenarios.

Cases	**RMSE of the Controllers**	
	MRAC	**PI**
Power Tracking without Disturbance	**60.37**	80.29
Power Tracking with Disturbance	**78.75**	83.38
Current Tracking without Disturbance	**2.44**	3.36
Current Tracking with Disturbance	**3.38**	3.95

Table 4.4 shows that when the system is free from any disturbance, MRAC achieves an RMSE of 2.44, outperforming PI's 3.36, confirming that MRAC is more precise. However, when the disturbance affects the non-inverting BDC, both controllers experience an increase in RMSE, but MRAC remains superior with a value of 3.38 versus PI's 3.95. Along with that, MRAC demonstrates superior performance in total power tracking with a lower RMSE of 60.37 compared to PI's 80.29 when the system is free from disturbance. Note that the performance of both controllers deteriorates significantly when it is measured from the aspect of power. Since power is the product of current and voltage and thus, the error in current tracking impacts on the power. Subsequently, when the system encounters the disturbance, both controllers' performance declines, but MRAC (78.75) still outperforms PI (83.38), showing that it handles disturbances more effectively. Moreover, it is important to highlight that none of the controllers directly play a role in controlling the power tracking and, thus, in reality, power tracking does not reflect the controllers' performance accurately.

In summary, MRAC consistently outperforms the PI controller in both power and current tracking scenarios, showing better accuracy and adaptability, especially in the presence of disturbances. This demonstrates MRAC's robustness, making it a better choice for systems where precise tracking is essential. The PI controller, while capable, struggles with higher error rates, particularly under disturbed conditions.

4.3.3 Discussion on the Performance of the Controllers

To comprehend the performance of the controllers with inverting and non-inverting BDC, multiple environments have been considered through simulation. Despite disturbances

being introduced to the inverting BDC, MRAC efficiently tracks voltage with a minimal RMSE of 0.04 for constant voltage and 0.05 for variable voltages under disturbances. Meanwhile, the fixed-gain PI controller also performs satisfactorily, showing minor fluctuations and RMSE errors of 0.97% for constant voltage and 1.53% for variable voltage when disturbances are present. A similar trait is noticed in tracking the current of disturbance-free non-inverting BDC, where MRAC with a RMSE of 2.44 outperforms PI with a RMSE of 3.36. Moreover, when the system is affected by the disturbance, MRAC shows its superiority over the PI controller, maintaining lower RMSE for a period of 100 seconds. MRAC's continuous adaptation of its gain over time provides a significant advantage, whereas PI lacks the ability to adapt in uncertain conditions, leading to less smooth performance.

MRAC and PI controllers exhibit similar performance in inverting BDC systems, with negligible differences in settling time, rise time, and peak time. Both controllers maintain stability with zero overshoot, highlighting their reliability in disturbance-free scenarios. However, when operating with non-inverting BDC systems under disturbed conditions, MRAC shows superior performance. MRAC has a faster settling time (1.8s vs. 1.92s) and significantly lower overshoot (1.62% vs. 69.16%) compared to PI, ensuring better stability. Although PI reaches the peak response quicker, it suffers from higher overshoot and undershoot, leading to instability and oscillation risk. In disturbance-free conditions, MRAC and PI show nearly identical performance in most metrics, but MRAC generally provides better stability and adaptability under disturbances, making it more suitable for systems requiring precision and control, while PI is faster but more prone to instability.

From a design perspective, MRAC is more complex than PI, requiring an appropriate reference model and ensuring Lyapunov stability, a challenging aspect for any system. In contrast, PI is more straightforward, with easier gain selection. Choosing the right controller ultimately involves balancing these trade-offs and considering the application. Given the need to meet voltage and current demand swiftly, with uncertainty, MRAC is a suitable choice for this application.

4.4 PERFORMANCE VALIDATION USING AN EV MODEL

A key motivation of this study is to assess the performance of the controllers with a BDC across various electric vehicle (EV) driving modes, including acceleration, constant speed, and braking. Therefore, in this section, appropriate drive cycles are used to evaluate the controllers by employing a standard EV longitudinal dynamics model. This approach provides deeper insight into how the designed controllers respond to the different demands of each driving mode. Hence, SC current and total HESS power tracking in different drive cycles have been considered when the system is affected by disturbances and free from disturbance.

In this study, current and power tracking errors are considered important performance indexes to measure the efficacy of the controllers, which have been explained in Section 4.3. Similarly, to evaluate the controllers' performance, RMSE has been adopted, especially how accurately they can track the current demand and fulfil the total HESS power demand according to the drive cycles.

4.4.1 Performance in HWFET Drive Cycle

This section explains how both controllers perform when the HWFET drive cycle has been considered with the proposed EV model both in the absence and presence of disturbance. Figure 4.18 demonstrates speed (in miles per hour) tracking of both PI and MRAC control approaches where the blue line indicates the reference speed cycle (HWFET), the red dash-dot line defines the MRAC-controlled response, and the golden dashed line shows the PI-controlled response. Noted that the system has been interfered with by an unknown disturbance frequently, as discussed in Section 4.3.1.1, when the controllers are employed to track the reference speed. Figure 4.18 portrays that both controllers are able to track the speed accurately even when the system is disturbed.

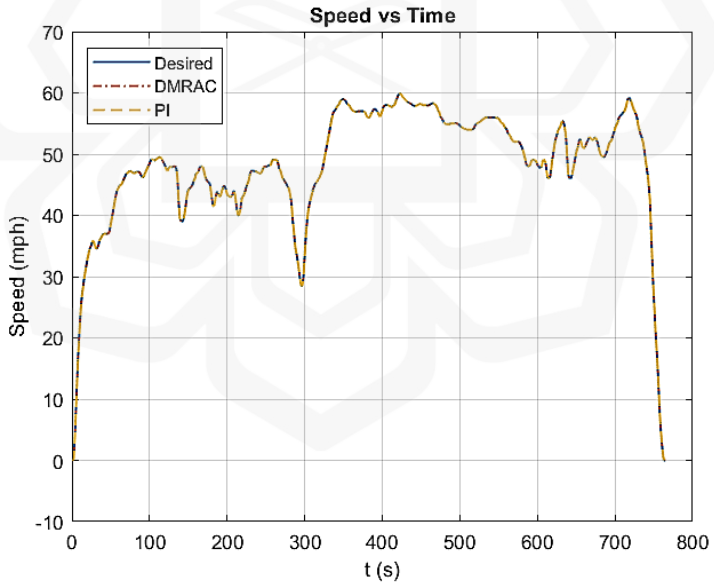

Figure 4.18 HWFET drive cycle tracking when the system is affected by the disturbance.

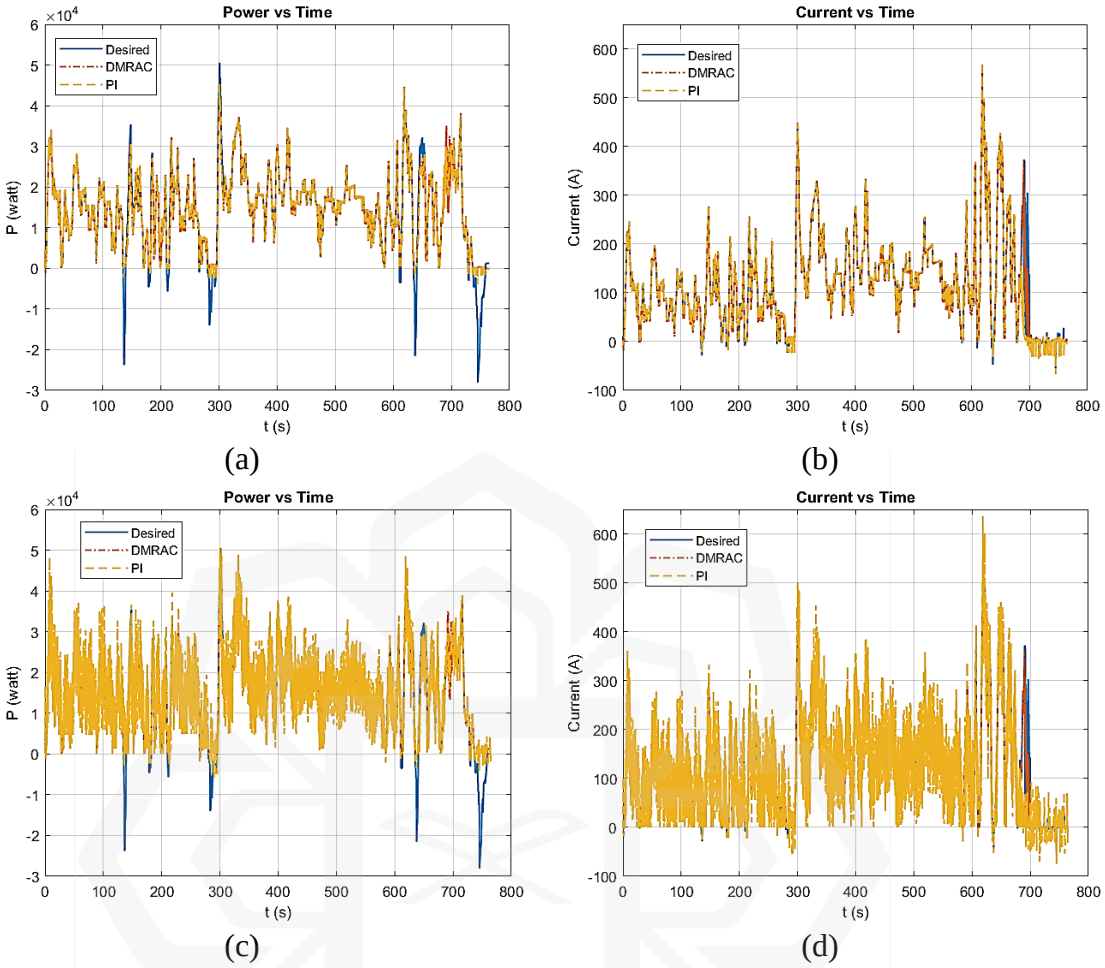

Figure 4.19 (a) Power and (b) SC current tracking in the absence of disturbance; (c) power and (d) SC current tracking in the presence of disturbance with HWFET drive cycle.

Figure 4.19 (a) and Figure 4.19 (c) demonstrate the HESS power tracking when the system is free from disturbance and affected by the disturbance, respectively. Here, HESS power tracking defines the extraction of battery and SC power to meet the vehicle power demand to track the HWFET drive cycle. In both Figure 4.19 (a) and Figure 4.19 (c), it is noticed that when the power demand (blue line) reaches below zero, which is regenerative braking mode, both the controllers are unable to track since the PMS is designed for any power above zero. In this mode, SC is charged and thus, the controllers are not responsible

for it since they are employed for the power discharge tracking only. Besides, at certain points, it is prominent that the controllers fail to track power demand at some points. In addition, Figure 4.19 (c) shows that due to the presence of system disturbance, the PI controller (golden dashed line) overshadows the MRAC technique's response (red dash-dot line). Thus, it defines that the PI controller shows a significant deviation in power tracking when the system is disturbed. Noted that this deviation has sprouted from the SC current tracking, as shown in Figure 4.19 (d), whereas MRAC shows a relatively smoother response, as shown in Figure 4.19 (c).

In order to explain the tracking error of the SC current, drive cycle and HESS power, from a quantitative perspective, RMSE has been considered, which has been discussed in Table 4.5.

Table 4.5 MRAC and PI controllers' tracking performance in HWFET drive cycles.

Parameters	**RMSE of the controllers**			
	In the absence of disturbance		**In the presence of disturbance**	
	MRAC	**PI**	**MRAC**	**PI**
Current tracking	13.22	**8.15**	**13.16**	39.74
Drive Cycle tracking	0.05	0.05	0.05	0.05
HESS Power tracking	$\mathbf{3.15\times10^3}$	3.23×10^3	$\mathbf{3.15\times10^3}$	4.85×10^3

Table 4.5 compares the tracking performance of MRAC and PI controllers in HWFET drive cycles, analyzing three key parameters: current tracking, drive cycle tracking, and HESS power tracking. RMSE is used as the performance metric both in the absence and presence of disturbances. For current tracking, MRAC consistently performs better than the PI controller, especially in the presence of disturbances, where PI's RMSE significantly increases from 8.15 to 39.74, indicating poor disturbance handling. Both controllers perform equally well in drive cycle tracking with negligible error (0.05 RMSE). However, for HESS power tracking, MRAC maintains a lower error (3.15×10^3) in both

scenarios, while PI shows a slightly higher error, particularly in the presence of disturbances, where the RMSE increases to 4.85×10^{3}. Overall, MRAC demonstrates superior robustness, especially under disturbance conditions in the HWFET drive cycle.

4.4.2 Performance in UDDS Drive Cycle

In this section, the performance of controllers has been evaluated considering the same three parameters current tracking, drive cycle tracking, and HESS power tracking when the vehicle tracks UDDS drive cycle.

Figure 4.20 illustrates the UDDS drive cycle tracking performance of the proposed EV model using HESS power, where both MRAC and PI controllers are responsible for current regulation primarily. Throughout the tracking process, both controllers closely follow the desired reference trajectory, with no noticeable deviations from the target speed in either the MRAC or PI controller responses.

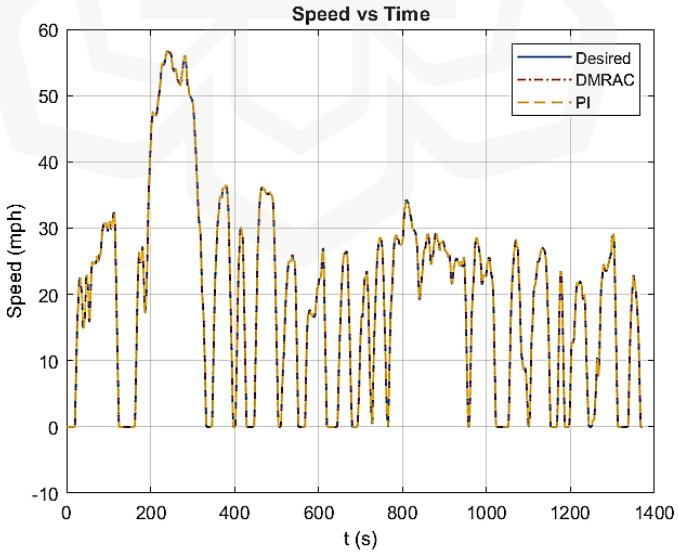

Figure 4.20 UDDS drive cycle tracking when the system is affected by the disturbance.

Figure 4.21 presents a comparative analysis of MRAC and PI controllers in tracking power and SC current over time, both in the absence and presence of disturbances within the UDDS drive cycle. Subfigures Figure 4.21 (a) and Figure 4.21 (b) demonstrate the power and SC current tracking under disturbance-free conditions, where both controllers follow the desired reference closely. MRAC exhibits slightly smoother tracking performance, with fewer oscillations and deviations compared to PI, particularly in current tracking. In contrast, subfigures Figure 4.21 (c) and Figure 4.21 (d) depict the same tracking metrics when disturbances are introduced. While both controllers are affected, MRAC shows greater resilience, maintaining more stable power and current tracking with fewer large deviations, especially in periods of high demand. PI, however, exhibits more noticeable fluctuations, indicating its vulnerability to disturbances. Overall, Figure 4.21 highlights MRAC's superior adaptability and robustness under dynamic and uncertain conditions, while PI, though effective in undisturbed scenarios, struggles to maintain precision in the presence of disturbances.

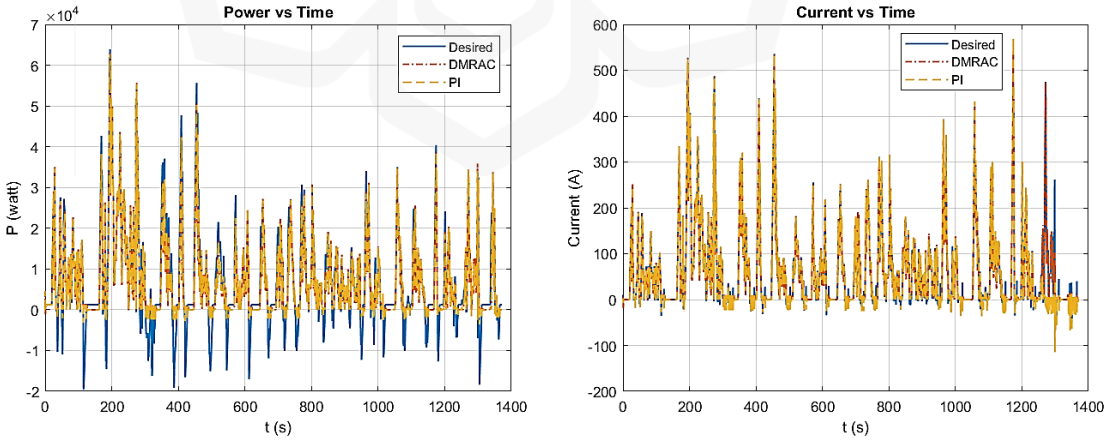

(a) (b)

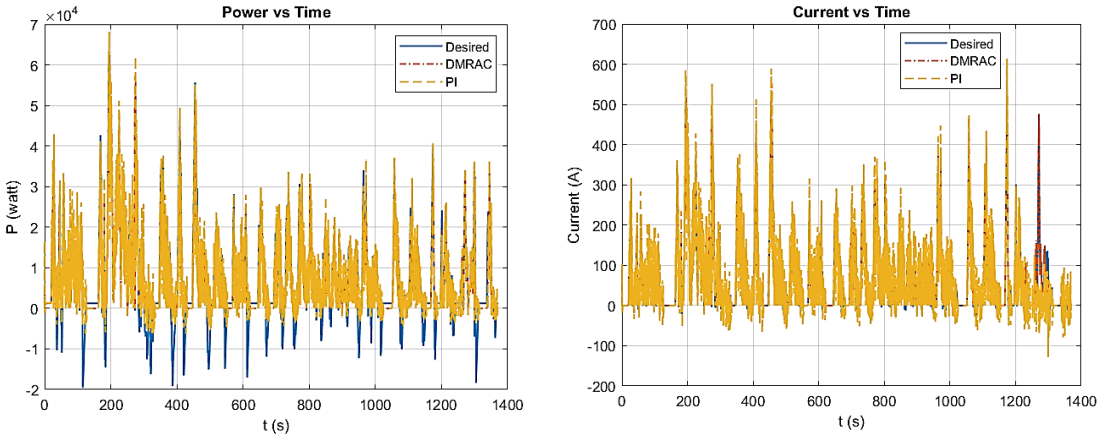

(c) (d)

Figure 4.21 (a) Power and (b) SC current tracking in the absence of disturbance; (c) power and (d) SC current tracking in the presence of disturbance with UDDS drive cycle.

In order to comprehend the performance of the controllers with higher accuracy, Table 4.6 has been introduced. Table 4.6 presents a comparison between MRAC and PI controllers based on their RMSE performance for current tracking, drive cycle tracking, and total power tracking under both disturbance and no-disturbance conditions. For current tracking, the PI controller shows a lower error than MRAC in the absence of disturbance (6.19 vs. 7.27), but its performance significantly degrades in the presence of disturbance, with an RMSE of 31.97, compared to 7.4 for MRAC. This suggests that PI is less robust to disturbances. Drive cycle tracking has negligible differences between the two controllers, both maintaining a low error of around 0.09-0.1 in all conditions. For total HESS power tracking, MRAC consistently exhibits slightly lower RMSE values in both disturbance and non-disturbance scenarios (3.6×10^3 to 3.76×10^3), while PI has higher errors in the presence of disturbance (4.71×10^3). Overall, MRAC demonstrates more stable and robust performance across all parameters, particularly in the presence of disturbances, making it a more reliable controller in dynamic environments.

Table 4.6 MRAC and PI controllers' tracking performance in UDDS drive cycles.

Parameters	**RMSE of the controllers**			
	In the absence of disturbance		**In the presence of disturbance**	
	MRAC	**PI**	**MRAC**	**PI**
Current tracking	7.27	**6.19**	**7.4**	31.97
Drive Cycle tracking	**0.09**	0.1	0.1	0.1
HESS Power tracking	$\mathbf{3.6\times10^3}$	3.71×10^3	$\mathbf{3.76\times10^3}$	4.71×10^3

4.4.3 Performance in FTP Drive Cycles

Figure 4.22 describes the FTP drive cycle tracking of the EV model utilizing the HESS power where the MRAC and PI controller control the current. During the tracking, significant deviations from the reference points are not visible in the MRAC and PI controller response.

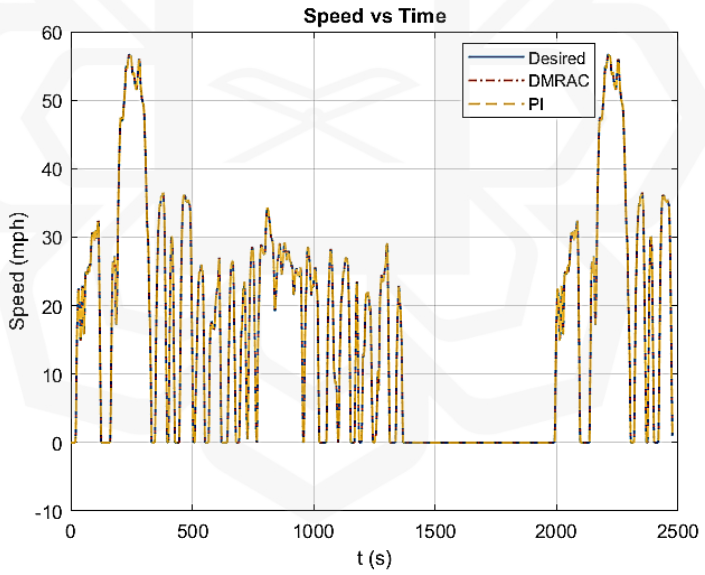

Figure 4.22 FTP drive cycle tracking when the system is affected by the disturbance.

Figure 4.23 illustrates the HESS power and SC current tracking performance of MRAC and PI controllers in the FTP drive cycle, under both undisturbed and disturbed conditions. Figure 4.23 (a) and Figure 4.23 (b) show power and current tracking without

disturbance, whereas Figure 4.23 (c) and Figure 4.23 (d) depict the tracking with disturbance. During the simulation, both the PI and MRAC controller show some deviation from the desired trajectory, particularly during rapid power changes, since minute deviation in current tracking, appears in a larger form in the power tracking as power is the product of voltage and current. Similar to the PI controller attitude in the HWFET and UDDS drive cycle, in the FTP drive cycle, PI shows higher deviation than MRAC when the system is affected by the disturbance.

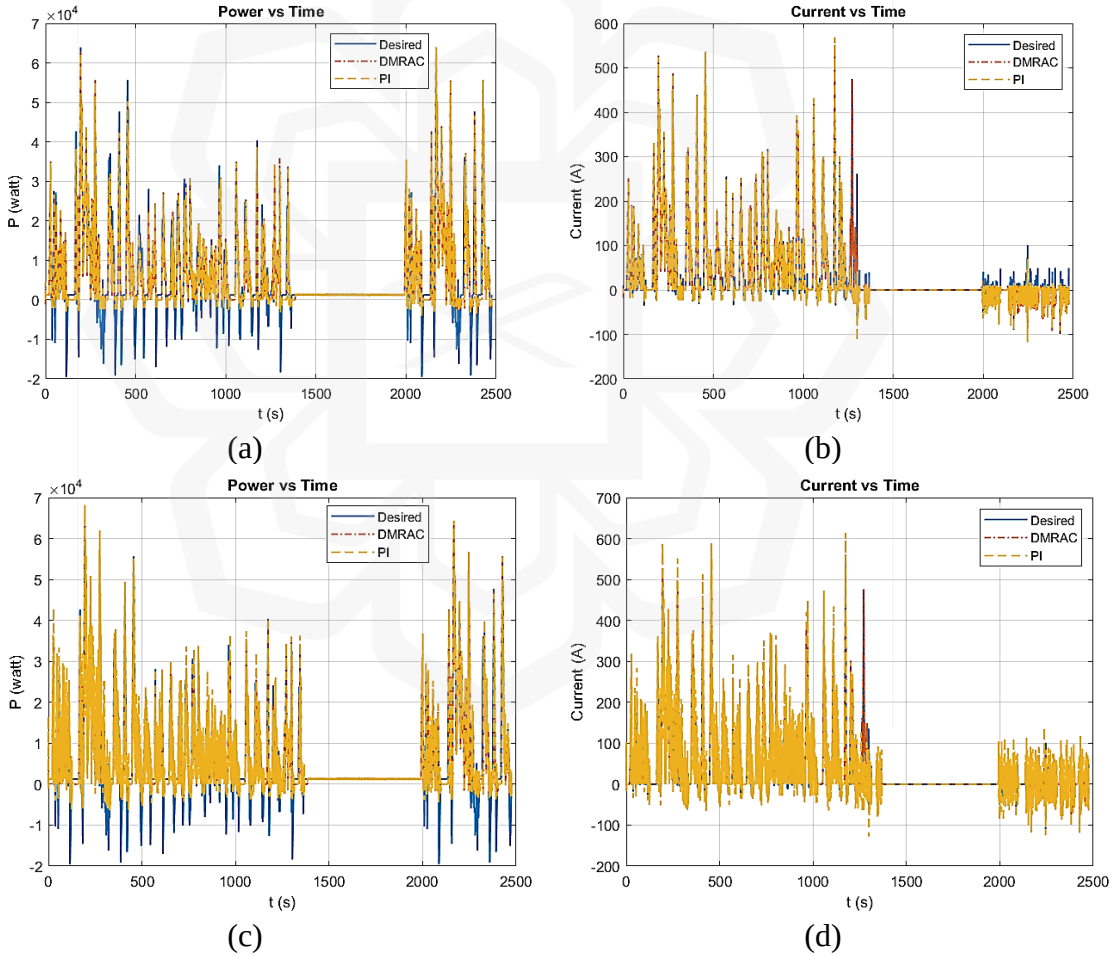

Figure 4.23 (a) Power and (b) SC current tracking in the absence of disturbance; (c) power and (d) SC current tracking in the presence of disturbance with FTP drive cycle.

To evaluate and compare the tracking performance of MRAC and PI controllers within the FTP drive cycle under varying conditions, namely in the presence and absence of disturbances, Table 4.7 has been introduced. Similar to Section 4.4.1 and Section 4.4.2, the assessment is conducted using the RMSE for current tracking, drive cycle tracking, and total power tracking to determine the efficacy of each controller in achieving the desired system outputs.

Table 4.7 shows that in current tracking, PI shows better performance in the absence of disturbances (4.13 RMSE) compared to MRAC (6.32 RMSE). However, in the presence of disturbances, the PI controller's performance significantly worsens (24.89 RMSE), indicating poor disturbance handling, while MRAC maintains a stable performance (6.34 RMSE). Drive cycle tracking is consistent across both controllers and scenarios, with negligible differences (0.07-0.08 RMSE), suggesting both are equally effective in this area. In total HESS power tracking, PI performs slightly better without disturbance (3.04×10^3 vs. MRAC's 3.56×10^3 RMSE), but its performance degrades in the presence of disturbances (4.22×10^3), while MRAC remains more stable (3.64×10^3). Overall, MRAC demonstrates superior robustness in handling disturbances across all parameters, while PI, despite initially stronger performance in undisturbed conditions, struggles significantly when disturbances are introduced.

Table 4.7 MRAC and PI controllers' tracking performance in FTP drive cycles.

Parameters	**RMSE of the controllers**			
	In the absence of disturbance		**In the presence of disturbance**	
	MRAC	**PI**	**MRAC**	**PI**
Current tracking	6.32	**4.13**	**6.34**	24.89
Drive Cycle tracking	0.08	**0.07**	0.08	0.08
HESS Power tracking	3.56×10^3	$\mathbf{3.04\times10^3}$	$\mathbf{3.64\times10^3}$	4.22×10^3

4.4.4 Performance in US06 Drive Cycle

Figure 4.24 illustrates the performance of the MRAC and PI controllers in tracking the US06 drive cycle when the system is subjected to disturbances. Both controllers closely follow the desired speed profile, with only minor deviations visible.

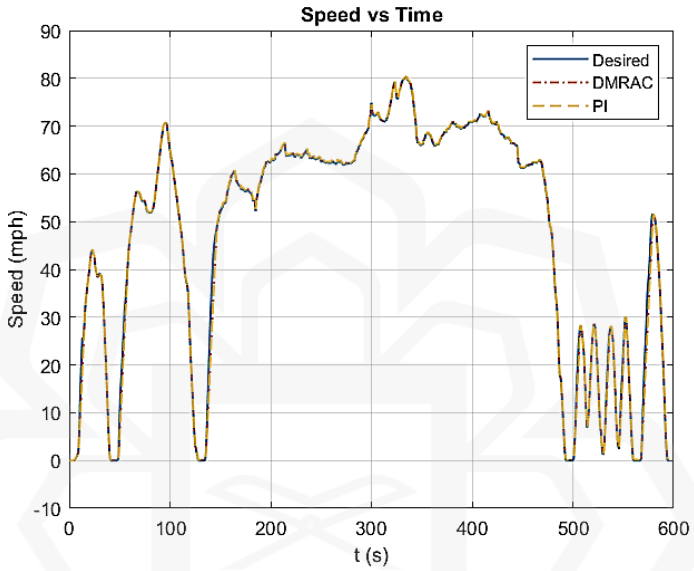

Figure 4.24 US06 drive cycle tracking when the system is affected by the disturbance.

Figure 4.25 shows the tracking performance of MRAC and PI controllers for power and SC current in the US06 drive cycle, both in the absence and presence of disturbance. Figure 4.25 (a) and Figure 4.25 (b) represent power and current tracking without disturbance, respectively, while Figure 4.25 (c) and Figure 4.25 (d) show the same metrics with disturbance. In both power and current tracking, both PI and MRAC controllers show similar responses during the simulation. However, around the 330th second, a significant deviation of MRAC is noticed, whereas the PI controller manages to tackle the moment, as shown in Figure 4.25 (b) and Figure 4.25 (d). Importantly, in the presence of disturbance, the PI controller also struggles with maintaining accurate current tracking, while MRAC

tends to retain its performance even though the system is affected by the disturbance. The analysis suggests that MRAC outperforms the PI controller in terms of dynamic response and adaptability, especially under disturbance, demonstrating its superiority in handling complex, transient scenarios typical in real-world driving conditions.

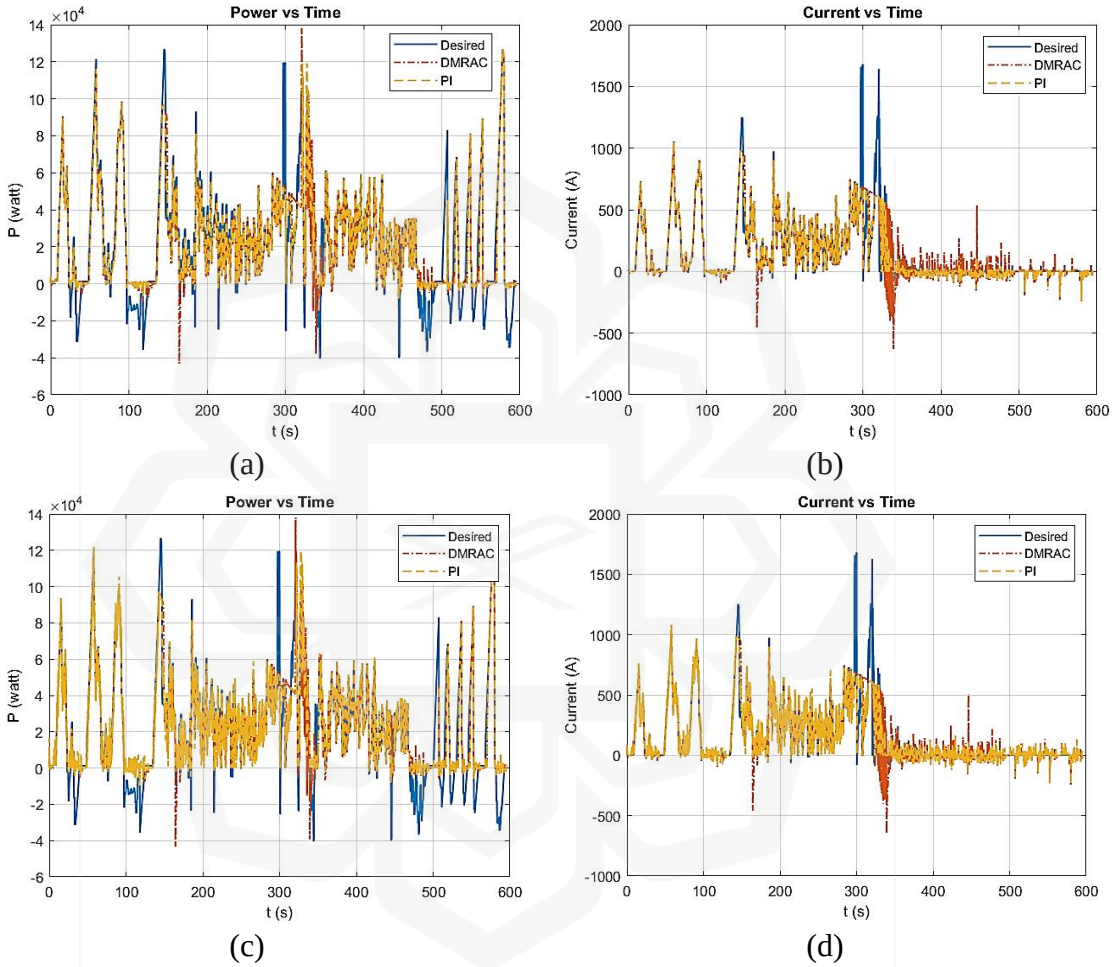

Figure 4.25 (a) Power and (b) SC current tracking in the absence of disturbance; (c) power and (d) SC current tracking in the presence of disturbance with US06 drive cycle.

Table 4.8 MRAC and PI controllers' tracking performance in US06 drive cycles.

Parameters	**RMSE of the controllers**			
	In the absence of disturbance		**In the presence of disturbance**	
	MRAC	**PI**	**MRAC**	**PI**
Current tracking	117.39	**106**	117.4	**114.47**
Drive Cycle tracking	**1.34**	1.37	1.34	**1.33**
HESS Power tracking	1.27×10^3	$\mathbf{1.25\times10^3}$	$\mathbf{1.27\times10^3}$	1.28×10^3

Table 4.8 presents the tracking performance of MRAC and PI controllers in the US06 drive cycle, evaluated through RMSE in both the absence and presence of disturbance. For current tracking, the PI controller performs slightly better than MRAC, having lower RMSE values both without disturbance (106 vs. 117.39) and with disturbance (114.47 vs. 117.4), unlike its performance in HWFET, UDDS and FTP drive cycle. It should be noted that the US06 drive cycle simulation runs for 576 seconds, leading to a relatively lower number of data points, which impacts the RMSE results. This is further substantiated by the PI controller's response, as illustrated in Figure 4.25 (c) and Figure 4.25 (d). For drive cycle tracking, both controllers exhibit similar performance, with RMSE values close to each other (1.34 for MRAC and 1.37/1.33 for PI). In terms of total HESS power tracking, the differences between MRAC and PI controllers are negligible, with RMSE values around 1.27×10^3 to 1.28×10^3 in both scenarios. Overall, the PI controller shows marginally better current tracking performance, while both controllers demonstrate comparable drive cycle and power tracking performance, indicating no significant advantage of MRAC over PI in these aspects.

4.5 SUMMARY

This chapter contributes to demonstrating the performance of MRAC and PI controllers within inverting and non-inverting Bidirectional DC-DC Converters (BDC) across varying conditions. According to the evaluation, MRAC demonstrates superior tracking capabilities, particularly in the presence of disturbances, with a minimal RMSE (Root Mean Square Error) of 0.04 for constant voltage and 0.05 for variable voltage, outperforming the fixed-gain PI controller, which shows higher RMSEs of 0.97% and 1.53%, respectively. For current tracking in non-disturbed non-inverting BDCs, MRAC also surpasses PI with

an RMSE of 2.44 compared to PI's 3.36. MRAC's adaptive gain provides better performance over time, especially in disturbed conditions, where it maintains lower RMSE for a longer period. While both controllers exhibit comparable performance in inverting BDC systems, particularly in terms of stability, settling time, and overshoot under disturbance-free conditions, MRAC stands out in non-inverting BDC systems under disturbances. It achieves faster settling times, significantly lower overshoot, and better overall stability, whereas PI, though quicker in peak response, suffers from higher overshoot, leading to instability and oscillations.

From a design standpoint, MRAC's complexity, due to the need for a well-defined reference model and the assurance of Lyapunov stability, presents challenges that PI avoids with its simpler gain selection. However, MRAC's adaptability makes it more suitable for applications requiring precision and robustness under uncertain conditions, while PI's faster response time is offset by its susceptibility to instability. Ultimately, the choice between MRAC and PI should be driven by the specific demands of the application. In environments where quick voltage and current adjustments are critical, particularly under unpredictable disturbances, MRAC emerges as the more appropriate solution due to its superior adaptability and control stability.

To further evaluate the performance of these controllers, an electric vehicle (EV) model was introduced, wherein the energy storage system (ESS) is modified from a battery-only configuration to a hybrid energy storage system (HESS) comprising a battery and supercapacitor (SC), integrated with a new power management system (PMS) which has been discussed in Section 3.7. This EV model is simulated under four different drive cycles—HWFET, UDDS, FTP, and US06—with and without system disturbances. Based on performance metrics such as current tracking, drive cycle tracking, and HESS power

tracking, the controllers' performance has been analyzed and summarized in Table 4.5 to Table 4.8. The analysis of the, reveals a clear pattern: MRAC consistently outperforms PI in conditions involving disturbances, particularly in the areas of current and power tracking. In the HWFET and FTP drive cycles (as demonstrated in Table 4.5 and Table 4.7), MRAC demonstrates stable performance with minimal increases in RMSE, whereas PI's performance significantly declines, especially in current tracking, where its RMSE escalates substantially in the presence of disturbances. Conversely, PI exhibits slightly better performance in disturbance-free scenarios, particularly in FTP drive cycles (as discussed in Table 4.7) and US06 (as portrayed in Table 4.8) for current tracking. Drive cycle tracking shows negligible differences between the two controllers across all cycles, indicating no significant advantage for either. While PI occasionally performs better in the absence of disturbances, MRAC's superior robustness in handling disturbances consistently positions it as the more reliable option, particularly in dynamic environments where disturbances are prevalent. Importantly, during drive cycle tracking, the controllers' performance does not demonstrate significant differences, indicating that the impact of distance over time on controller performance may be inconclusive. From a practical application perspective, this analysis underscores the resilience of MRAC, highlighting its suitability for systems requiring stability amid variable conditions.

CHAPTER FIVE

CONCLUSION

5.1 INTRODUCTION

The increasing shift from internal combustion engine vehicles to electric vehicles (EVs) has prompted significant advancements in energy storage systems (ESS) and power management. In this research, an adaptive control strategy was developed and evaluated for bidirectional DC-DC converters (BDC) to improve the performance of ESS in hybrid electric vehicles (HEVs), addressing the key driving modes—acceleration, cruising, and braking. This chapter concludes the research by summarizing the major contributions, achievements according to the research objectives, limitations of the study, and potential areas for future improvement.

5.2 SUMMARY OF ACHIEVEMENTS

The primary objectives of this research were to design an adaptive controller for a BDC, evaluate its performance, analyze its effectiveness in a hybrid energy storage system (HESS), and validate its performance under realistic EV conditions through simulations. A Model Reference Adaptive Control (MRAC) was chosen and implemented as the adaptive controller, while the performance was compared to a conventional proportional-integral (PI) controller. Table 5.1 presents a summary of the achievements corresponding to the research objectives.

Table 5.1 Research objectives and achievements.

Objectives	Achievements
Objective 1: To design an adaptive controller for a simple BDC supplying a constant and variable battery pack voltage for satisfying the three driving modes in EV: acceleration, cruising, and braking.	**Controller Design**: Developed a Model Reference Adaptive Control (MRAC) system capable of regulating voltage effectively for the three driving modes such as acceleration, cruising, and braking.
Objective 2: To evaluate the performance of the controller based on performance indexes such as control effort and tracking error.	**Comparison with PI Controller**: Evaluated MRAC performance against the PI controller in terms of Root Mean Square Error (RMSE) for voltage and current tracking and control effort. **Superior Performance**: MRAC consistently outperformed PI with lower RMSE values, particularly under disturbed conditions. For example: • In the inverting BDC, the MRAC approach achieves an RMSE of 0.05 for tracking constant voltage with disturbance, and 0.43 for variable voltage with disturbance, whereas the PI controller produces RMSE values of 1.53 and 1.41 for these respective scenarios. • In the non-inverting BDC, the MRAC method also demonstrates greater accuracy than the PI controller in tracking current and power with system disturbances, showing RMSEs of 3.38 and 78.75, compared to the PI controller's RMSEs of 3.95 and 83.38. However, MRAC approach shows that it requires comparatively higher control effort with inverting BDC. Importantly, this control effort is interpreted by PWM signals, and thus, the higher control effort is unable to contribute to higher energy consumption.
Objective 3: To analyze the performance of an adaptive controller with the BDC for a Hybrid Energy Storage System (HESS) where the current supply is	**Hybrid System Integration**: Designed a HESS of Li-ion battery and supercapacitor, along with the rule-based power management system (PMS), utilizing MRAC to regulate power transitions between sources. For example: The non-inverting BDC employs a rule-based PMS to fulfill the motor's power demand. The PMS functions based on set thresholds: if the demand surpasses 1.5 kW, the battery

switched between a battery pack and a supercapacitor.	supplies minimal power, while the SC delivers the remainder. When the SC's voltage exceeds 50% of its maximum capacity, the load is shared between the battery and SC; otherwise, the battery handles the power supply on its own. **Smooth Power Supply**: Validated that MRAC ensures a seamless switch between battery and supercapacitor, leading to a stable power supply with the help of PMS.
Objective 4: To validate the adaptive controller performance from the aspect of performance indexes such as control effort, power, and current tracking accuracy according to the demand from an electric vehicle longitudinal dynamic model based on different drive cycles.	**Drive Cycle Validation**: Tested MRAC under different driving cycles (HWFET, FTP, UDDS, US06) with and without disturbances. The results can be outlined as: • **HWFET Drive Cycle**: MRAC outperforms PI in current tracking under disturbance conditions, with an RMSE of 8.15 compared to PI's significantly higher RMSE of 39.74. • **UDDS Drive Cycle**: In current tracking with disturbances, MRAC maintains a stable RMSE of 7.4, while PI's RMSE increases drastically to 31.97, highlighting PI's poor disturbance handling. • **FTP Drive Cycle**: MRAC shows consistent performance with an RMSE of 6.34 under disturbances, while PI's RMSE jumps to 24.89, indicating weaker performance. • **US06 Drive Cycle:** The PI controller slightly outperforms MRAC in current tracking, with RMSE values of 106 vs. 117.39 without disturbance and 114.47 vs. 117.4 with disturbance. This difference can be attributed to the shorter simulation duration (576 seconds), which results in fewer data points and affects the accuracy of the RMSE calculation. Consequently, MRAC's typical advantage in handling disturbances is not as prominent in this scenario. Additionally, both controllers perform similarly in drive cycle and HESS power tracking, showing no significant advantage for MRAC in these metrics. **Robust Tracking Accuracy**: MRAC exhibited superior tracking accuracy and robustness compared to the PI controller, especially in disturbed scenarios.

5.3 KEY FINDINGS

The results of the study highlighted several important insights into the performance of MRAC compared to the PI controller:

1. **Controller Design and Voltage or Current Regulation**: The MRAC is designed to effectively control the voltage or current for different driving modes, including acceleration, cruising, and braking. The MRAC shows adaptability in providing the necessary voltage regulation to meet the demands of these driving modes, showcasing a marked improvement over traditional control methods.

2. **Performance Comparison and Evaluation**: The performance of the MRAC is assessed against the conventional PI controller using metrics such as RMSE for voltage and current tracking. The MRAC consistently outperforms the PI controller, achieving lower RMSE values, particularly in disturbances scenarios. This demonstrates the robustness of MRAC in maintaining stability and precision in tracking, even under challenging conditions.

3. **Hybrid Energy Storage System Integration**: The study explores the integration of a hybrid energy storage system (HESS) consisting of a Li-ion battery and a supercapacitor. The MRAC ensured smooth power regulation between the battery and supercapacitor, facilitating stable and reliable power delivery. The use of the hybrid system enables efficient energy management, particularly during regenerative braking and high-power demand conditions.

4. **Drive Cycle Validation**: The MRAC's performance is validated through simulations involving four different drive cycles: HWFET, FTP, UDDS, and US06.

The controller is tested with and without disturbances to evaluate its robustness in real-world driving conditions. The MRAC demonstrates superior current and power tracking accuracy, maintaining stable performance across all driving cycles, especially in the presence of disturbances. The PI controller, although exhibiting slightly better performance in some disturbance-free scenarios, struggled to maintain stability under disturbed conditions.

5.4 CONTRIBUTIONS OF THE RESEARCH

This research made several contributions to the field of EV power management and adaptive control:

1. **Development of adaptive control strategy**: The MRAC has successfully been developed and implemented to regulate the BDC in EV applications, providing an adaptive and robust solution for voltage and current tracking. This controller addresses the shortcomings of traditional controllers such as PID or PI, especially in nonlinear and uncertain environments.

2. **Performance evaluation under realistic conditions**: The MRAC is evaluated not only in a simple battery-based ESS but also in a hybrid system involving a supercapacitor, under real-world driving conditions. The detailed comparison between MRAC and PI controllers provides valuable insights into the advantages of adaptive control for EV power management.

3. **HESS implementation**: The integration of a hybrid energy storage system (battery and supercapacitor) with the BDC and MRAC enables efficient power

management, demonstrating the potential for improved energy efficiency and performance in EVs.

5.5 LIMITATIONS OF THE RESEARCH

While the research achieved its stated objectives and demonstrated the potential of MRAC in EV power management, several limitations should be acknowledged:

1. **Simulation-based analysis**: The performance of the MRAC and PI controllers has been validated through simulations only. No hardware implementation or real-time hardware-in-the-loop (HIL) testing is conducted. As a result, the practical feasibility of the controllers in real-world scenarios remains to be demonstrated.
2. **Limited environmental factors**: The study has not considered extreme environmental conditions, such as varying temperatures or other factors that could affect battery and supercapacitor performance. Evaluating the controller's performance under different temperature profiles and environmental stressors is crucial for assessing its robustness in real-world applications.
3. **Parameter sensitivity of MRAC**: The MRAC design requires the careful selection of adaptation gains to ensure system stability and performance. The sensitivity of the MRAC to parameter variations presents a challenge in tuning the controller, particularly in real-time implementations where changes in system dynamics can occur.

5.6 FUTURE IMPROVEMENTS

To build on the achievements of this research and address its limitations, several areas for future work are proposed:

1. **Optimization of MRAC parameters**: Future work can focus on enhancing the MRAC design to minimize computational complexity, making the controller more feasible for real-time applications. Introducing optimization algorithms, such as genetic algorithms or machine learning techniques, to automatically determine the best adaptation rates and parameters would further improve system performance.
2. **Reference Model Design**: The reference model for MRAC must be appropriately selected to enhance system performance regarding settling time, rise time, peak time, and overshoot.
3. **Expansion of HESS**: Expanding the HESS to include other types of energy sources, such as fuel cells or flywheels, can provide further optimization of energy usage and extend the range of EVs. Additionally, incorporating predictive control strategies that consider future energy demands based on drive cycle predictions could lead to better energy management.
4. **Hardware-in-the-Loop (HIL) validation**: Testing the adaptive controller in a real-time hardware-in-the-loop (HIL) environment may validate the simulation results and provide practical insights into implementation challenges. This will help in refining the controller for real-world applications and assessing its feasibility for mass production.

5. **Evaluation Under Extreme Conditions**: Evaluating the controller's performance under extreme environmental conditions, such as high-temperature variations or different terrain profiles, would further demonstrate its robustness and adaptability, ensuring reliable performance across a wide range of real-world scenarios.

5.7 SUMMARY

This research has successfully developed and validated an MRAC for a BDC in electric vehicle applications. The MRAC demonstrates superior performance compared to the PI controller in terms of voltage and current tracking, particularly in disturbed conditions. The use of a HESS comprising a battery and supercapacitor further enhanced the performance of the system, allowing for efficient power management under different driving scenarios. The findings of this research underscore the potential of adaptive control strategies to enhance the efficiency, stability, and reliability of electric vehicle power management systems.

The work presented here contributes significantly to the field of EV power management, offering an adaptive solution for voltage and current regulation in BDCs. With future improvements focused on optimization, appropriate reference model design, and real-time validation, this research lays a strong foundation for the development of more efficient, adaptive, and robust power management systems in the evolving landscape of electric mobility.

REFERENCES

Adkins, E., & Taylor Jr, L. (1964). Adaptive flight control systems-pro and con.

Agency, E. P. (2022). *Dynamometer Drive Schedules*. U.S. Environmental Protection Agency.

Akter, P., Uddin, M., Mekhilef, S., Tan, N. M. L., & Akagi, H. (2015). Model predictive control of bidirectional isolated DC–DC converter for energy conversion system. *International journal of electronics*, *102*(8), 1407-1427.

Al-Samari, A. (2017). Study of emissions and fuel economy for parallel hybrid versus conventional vehicles on real world and standard driving cycles. *Alexandria Engineering Journal*, *56*(4), 721-726.

Al Hysam, M. A., Haque, M. Z. U., Saifullah, K., Asif, S., & Sarowar, G. (2017). New topologies of Cuk PFC converter with switched capacitor for low power applications. 2017 IEEE Region 10 Humanitarian Technology Conference (R10-HTC),

Albiol-Tendillo, L., Vidal-Idiarte, E., Maixé-Altés, J., Bosque-Moncusí, J., & Valderrama-Blavi, H. (2012). Design and control of a bidirectional DC/DC converter for an Electric Vehicle. 2012 15th International Power Electronics and Motion Control Conference (EPE/PEMC),

Ali, M. U., Zafar, A., Nengroo, S. H., Hussain, S., Junaid Alvi, M., & Kim, H.-J. (2019). Towards a smarter battery management system for electric vehicle applications: A critical review of lithium-ion battery state of charge estimation. *Energies*, *12*(3), 446.

Allaoua, B., Asnoune, K., & Mebarki, B. (2017). Energy management of PEM fuel cell/supercapacitor hybrid power sources for an electric vehicle. *International journal of hydrogen energy*, *42*(33), 21158-21166.

Allaoua, B., & Laoufi, A. (2011). Application of a robust fuzzy sliding mode controller synthesis on a buck-boost DC-DC converter power supply for an electric vehicle propulsion system. *Journal of Electrical Engineering and Technology*, *6*(1), 67-75.

Allegre, A.-L., Bouscayrol, A., & Trigui, R. (2009). Influence of control strategies on battery/supercapacitor hybrid energy storage systems for traction applications. 2009 IEEE Vehicle Power and Propulsion Conference,

Amjadi, Z., & Williamson, S. S. (2009). Power-electronics-based solutions for plug-in hybrid electric vehicle energy storage and management systems. *IEEE Transactions on industrial electronics*, *57*(2), 608-616.

Arce, P., Medrano, M., Gil, A., Oró, E., & Cabeza, L. F. (2011). Overview of thermal energy storage (TES) potential energy savings and climate change mitigation in Spain and Europe. *Applied energy*, *88*(8), 2764-2774.

Ardhenta, L., & Subroto, R. K. (2020). Application of direct MRAC in PI controller for DC-DC boost converter. *International Journal of Power Electronics and Drive Systems*, *11*(2), 851.

Argentim, W. C. R., Paulo E. Santos, Renato A. Aguiar. (2013). PID, LQR and LQR-PID on a Quadcopter Platform. *IEEE*.

Arslan, M., Ahmad, I., Azeem, M. K., & Liaquat, M. (2021). Dual-stage adaptive control of hybrid energy storage system for electric vehicle application. *Journal of Energy Storage*, *43*, 103165.

Åström, K. J. (1983). Theory and applications of adaptive control—a survey. *Automatica*, *19*(5), 471-486.

Åström, K. J., & Wittenmark, B. (2013). *Adaptive control*. Courier Corporation.

Azidin, F. A., Hannan, M. A., & Mohamed, A. (2013). Renewable energy technologies and hybrid electric vehicle challenges. *PRZEGLĄD ELEKTROTECHNICZNY (Electrical Review)*, *89*(8), 150-156.

Bai, Z., Yan, Z., Wu, X., Xu, J., & Cao, B. (2019). H∞ Control for Battery/Supercapacitor Hybrid Energy Storage System Used in Electric Vehicles. *International Journal of Automotive Technology*, *20*(6), 1287-1296.

Bartolini, G., Ferrara, A., Usai, E., & Utkin, V. I. (2000). On multi-input chattering-free second-order sliding mode control. *IEEE transactions on automatic control*, *45*(9), 1711-1717.

Basri, M., Ariffanan, M., Danapalasingam, K. A., & Husain, A. R. (2014). Design and optimization of backstepping controller for an underactuated autonomous quadrotor unmanned aerial vehicle. *Transactions of FAMENA*, *38*(3), 27-44.

Belik, S., Dreißigacker, V., Dieterich, M., & Kraft, W. (2017). Thermal Energy Storage Systems: Power-to-Heat Concepts in Solid Media Storage for High Storage Densities. *Journal of Traffic and Transportation Engineering*, *5*, 285-294.

Bellur, D. M., & Kazimierczuk, M. K. (2007). DC-DC converters for electric vehicle applications. 2007 Electrical Insulation Conference and Electrical Manufacturing Expo,

Bendaas, I., & Naceri, F. (2013). A new method to minimize the chattering phenomenon in sliding mode control based on intelligent control for induction motor drives. *Serbian journal of electrical engineering*, *10*(2), 231-246.

Bierling, T. (2014). *Comparative Analysis of Adaptive Control Techniques for Improved Robust Performance* Technischen Universität München]. Germany.

Bindra, H., & Revankar, S. (2018). *Storage and Hybridization of Nuclear Energy: Techno-economic Integration of Renewable and Nuclear Energy*. Academic Press.

Boiko, I., & Fridman, L. (2005). Analysis of chattering in continuous sliding-mode controllers. *IEEE transactions on automatic control*, *50*(9), 1442-1446.

Boskovich, B., & Kaufmann, R. (1966). Evolution of the honeywell first-generation adaptive autopilot and its applications to F-94, F-101, X-15, and X-20 vehicles. *Journal of Aircraft*, *3*(4), 296-304.

Bouffard, P. (2012). *On-board Model Predictive Control of a Quadrotor Helicopter: Design, Implementation, and Experiments* University of California]. Berkeley.

Brando, G., Del Pizzo, A., & Meo, S. (2018). Model-reference adaptive control of a dual active bridge dc-dc converter for aircraft applications. 2018 International Symposium on Power Electronics, Electrical Drives, Automation and Motion (SPEEDAM),

Buckles, W., & Hassenzahl, W. V. (2000). Superconducting magnetic energy storage. *IEEE Power Engineering Review*, *20*(5), 16-20.

Burke, A., & Miller, M. (2011). The power capability of ultracapacitors and lithium batteries for electric and hybrid vehicle applications. *Journal of Power Sources*, *196*(1), 514-522.

Cano, Z. P., Banham, D., Ye, S., Hintennach, A., Lu, J., Fowler, M., & Chen, Z. (2018). Batteries and fuel cells for emerging electric vehicle markets. *Nature Energy*, *3*(4), 279-289.

Carsalesbase. (2018). *Toyota Mirai*. http://carsalesbase.com/us-car-sales-data/toyota/toyota-mirai/

Chakraborty, S., Hasan, M. M., & Razzak, M. A. (2017). Transformer-less single-phase grid-tie photovoltaic inverter topologies for residential application with various filter circuits. *Renewable and Sustainable Energy Reviews*, *72*, 1152-1166.

Chakraborty, S., Reza, S. S., & Hasan, W. (2015). Design and analysis of hybrid solar-wind energy system using CUK & SEPIC converters for grid connected inverter application. 2015 IEEE 11th International Conference on Power Electronics and Drive Systems,

Chakraborty, S., Vu, H.-N., Hasan, M. M., Tran, D.-D., Baghdadi, M. E., & Hegazy, O. (2019). DC-DC converter topologies for electric vehicles, plug-in hybrid electric vehicles and fast charging stations: state of the art and future trends. *Energies*, *12*(8), 1569.

Chan, C., & Wong, Y. (2004). Electric vehicles charge forward. *IEEE Power and Energy Magazine*, *2*(6), 24-33.

Chan, R., Kim, J.-c., Baek, J., Kim, N., & Kwak, S. (2017). Model predictive current control method with constant switching frequency for single-phase voltage source inverters. 2017 19th European Conference on Power Electronics and Applications (EPE'17 ECCE Europe),

Chau, K., Wong, Y., & Chan, C. (1999). An overview of energy sources for electric vehicles. *Energy Conversion and Management*, *40*(10), 1021-1039.

Chen, Y. T., Lin, W. C., & Liang, R. H. (2015). An interleaved high step-up DC-DC converter with double boost paths. *International Journal of Circuit Theory and Applications*, *43*(8), 967-983.

Choudhury, S. (2021). Flywheel energy storage systems: A critical review on technologies, applications, and future prospects. *International transactions on electrical energy systems*, *31*(9), e13024.

Chung, C.-W., & Chang, Y. Design of Adaptive Backstepping controller for Systems with Mismatched Perturbations to Achieve Asymptotical Stability.

Chung, L. W., Siam, M. F. M., Ismail, A. B., & Hussien, Z. F. (2004). Modeling and simulation of sodium sulfur battery for battery-energy storage system and custom power devices. PECon 2004. Proceedings. National Power and Energy Conference, 2004.,

Ciccarelli, F., & Lauria, D. (2010). Sliding-mode control of bidirectional dc-dc converter for supercapacitor energy storage applications. SPEEDAM 2010,

Creutzig, F., Papson, A., Schipper, L., & Kammen, D. M. (2009). Economic and environmental evaluation of compressed-air cars. *Environmental Research Letters*, *4*(4), 044011.

Das, R., & UddinChowdhury, M. A. (2016). PI controlled bi-directional DC-DC converter (BDDDC) and highly efficient boost converter for electric vehicles. 2016 3rd International Conference on Electrical Engineering and Information Communication Technology (ICEEICT),

David, L., & Thomas, B. R. (2001). Handbook of batteries. In: McGraw-Hill Professional.

Dennehy, C. J., Orr, J. S., Barshi, I., & Statler, I. C. (2014). A comprehensive analysis of the X-15 Flight 3-65 accident.

Devi Vidhya, S., & Balaji, M. (2020). Hybrid fuzzy PI controlled multi-input DC/DC converter for electric vehicle application. *Automatika*, *61*(1), 79-91.

Dhand, A., & Pullen, K. (2015). Review of battery electric vehicle propulsion systems incorporating flywheel energy storage. *International Journal of Automotive Technology*, *16*(3), 487-500.

DieselNet. (2023). *SFTP-US06* https://dieselnet.com/standards/cycles/ftp_us06.php

Dinçer, İ., & Zamfirescu, C. (2014). *Advanced power generation systems*. Academic Press.

Dixon, J., Nakashima, I., Arcos, E. F., & Ortúzar, M. (2009). Electric vehicle using a combination of ultracapacitors and ZEBRA battery. *IEEE transactions on industrial electronics*, *57*(3), 943-949.

Djebbri, S., Ladaci, S., Metatla, A., & Balaska, H. (2018). Robust MRAC Supervision of a Multi-source Renewable Energy System Using Fractional-Order Integrals. 2018 International Conference on Electrical Sciences and Technologies in Maghreb (CISTEM),

Douglas, H., & Pillay, P. (2005). Sizing ultracapacitors for hybrid electric vehicles. 31st Annual Conference of IEEE Industrial Electronics Society, 2005. IECON 2005.,

Du, Y., Lukic, S., Jacobson, B., & Huang, A. (2011). Review of high power isolated bi-directional DC-DC converters for PHEV/EV DC charging infrastructure. 2011 IEEE Energy Conversion Congress and Exposition,

Dydek, Z. T. (2010). *Adaptive control of unmanned aerial systems* Massachusetts institute of Technology].

Dydek, Z. T., Annaswamy, A. M., & Lavretsky, E. (2008). Adaptive control and the NASA X-15 program: a concise history, lessons learned, and a provably correct design. 2008 American Control Conference,

Dydek, Z. T., Annaswamy, A. M., & Lavretsky, E. (2010). Adaptive control and the NASA X-15-3 flight revisited. *IEEE Control Systems Magazine*, *30*(3), 32-48.

Ebad, M., & Song, B.-M. (2012). Accurate model predictive control of bidirectional DC-DC converters for DC distributed power systems. 2012 IEEE Power and Energy Society General Meeting,

Ecopoint. (2023a). *EPA Highway Fuel Economy Test Cycle (HWFET)* https://dieselnet.com/standards/cycles/hwfet.php

Ecopoint. (2023b). *EPA Urban Dynamometer Driving Schedule (UDDS) for Heavy-Duty Vehicles* https://dieselnet.com/standards/cycles/udds.php

Elsayad, N., Moradisizkoohi, H., & Mohammed, O. A. (2019). A Single-Switch Transformerless DC--DC Converter With Universal Input Voltage for Fuel Cell Vehicles: Analysis and Design. *IEEE transactions on Vehicular Technology*, *68*(5), 4537-4549.

Emadi, A., Lee, Y. J., & Rajashekara, K. (2008). Power electronics and motor drives in electric, hybrid electric, and plug-in hybrid electric vehicles. *IEEE Transactions on industrial electronics*, *55*(6), 2237-2245.

Erzberger, H. (1967). Analysis and design of model following control systems by state space techniques.

Expresswire, T. (2019). *Ever-increasing Global Energy Requirements Driving The Growth Of Superconducting Magnetic Energy Storage Market*

Faisal, M., Hannan, M. A., Ker, P. J., Hussain, A., Mansor, M. B., & Blaabjerg, F. (2018). Review of energy storage system technologies in microgrid applications: Issues and challenges. *IEEE access*, *6*, 35143-35164.

Fatah, B., Chokri, M., Hamed, Y., Naceur, H., & Hassan, H. (2012). Hybrid modelling of energy management system in electric traction. International Conference on Control, Engineering & Information Technology,

Forouzesh, M., Siwakoti, Y. P., Gorji, S. A., Blaabjerg, F., & Lehman, B. (2017). Step-up DC–DC converters: a comprehensive review of voltage-boosting techniques, topologies, and applications. *IEEE Transactions on Power Electronics*, *32*(12), 9143-9178.

Garcia, P., Fernandez, L. M., Garcia, C. A., & Jurado, F. (2009). Energy management system of fuel-cell-battery hybrid tramway. *IEEE Transactions on Industrial Electronics*, *57*(12), 4013-4023.

Ghorbani, R., Bibeau, E., & Filizadeh, S. (2010). On conversion of hybrid electric vehicles to plug-in. *IEEE transactions on Vehicular Technology*, *59*(4), 2016-2020.

Gong, K., Shi, J., Liu, Y., Wang, Z., Ren, L., & Zhang, Y. (2016). Application of SMES in the microgrid based on fuzzy control. *IEEE Transactions on Applied Superconductivity*, *26*(3), 1-5.

Goodwin, G. C., & Mayne, D. Q. (1987). A parameter estimation perspective of continuous time model reference adaptive control. *Automatica*, *23*(1), 57-70.

Hadartz, M., & Julander, M. (2008). *Battery-supercapacitor energy storage*. Chalmers University of Technology Gothenburg, Sweden.

Hadjipaschalis, I., Poullikkas, A., & Efthimiou, V. (2009). Overview of current and future energy storage technologies for electric power applications. *Renewable and sustainable energy reviews*, *13*(6-7), 1513-1522.

Hannan, M., Azidin, F., & Mohamed, A. (2012). Multi-sources model and control algorithm of an energy management system for light electric vehicles. *Energy Conversion and Management*, *62*, 123-130.

Hannan, M., Hoque, M., Mohamed, A., & Ayob, A. (2017). Review of energy storage systems for electric vehicle applications: Issues and challenges. *Renewable and Sustainable Energy Reviews*, *69*, 771-789.

Hannan, M. A., Lipu, M. H., Hussain, A., & Mohamed, A. (2017). A review of lithium-ion battery state of charge estimation and management system in electric vehicle applications: Challenges and recommendations. *Renewable and Sustainable Energy Reviews*, *78*, 834-854.

Hasnain, S. (1998). Review on sustainable thermal energy storage technologies, Part I: heat storage materials and techniques. *Energy conversion and management*, *39*(11), 1127-1138.

Hawlader, M., Uddin, M., & Khin, M. M. (2003). Microencapsulated PCM thermal-energy storage system. *Applied energy*, *74*(1-2), 195-202.

He, Y., & Luo, F. (2005). Analysis of Luo converters with voltage-lift circuit. *IEE Proceedings-Electric Power Applications*, *152*(5), 1239-1252.

Hedlund, M. (2010). Design and construction of a bidirectional DCDC converter for an EV application. In.

Hedlund, M., Lundin, J., De Santiago, J., Abrahamsson, J., & Bernhoff, H. (2015). Flywheel energy storage for automotive applications. *Energies*, *8*(10), 10636-10663.

Hegazy, O., Van Mierlo, J., & Lataire, P. (2011). Control and analysis of an integrated bidirectional DC/AC and DC/DC converters for plug-in hybrid electric vehicle applications. *Journal of power electronics*, *11*(4), 408-417.

Holleman, E. C. (1966). Summary of high-altitude and entry flight control experience with the X-15 airplane.

Hoque, M., Hannan, M., Mohamed, A., & Ayob, A. (2017). Battery charge equalization controller in electric vehicle applications: A review. *Renewable and Sustainable Energy Reviews*, *75*, 1363-1385.

Huo, X., Huo, M., & Karimi, H. R. (2014). Attitude stabilization control of a quadrotor UAV by using backstepping approach. *Mathematical Problems in Engineering*, *2014*.

Infineon Technologies. (2024). 11 kW bi-directional CLLC DC-DC converter with 1200 V and 1700 V CoolSiC™ MOSFETs. In (1.2 ed.): Infineon Technologies.

Ioannou, P. A., & PV, K. (1983). Adaptive systems with reduced models.

Ise, T., Kita, M., & Taguchi, A. (2005). A hybrid energy storage with a SMES and secondary battery. *IEEE Transactions on Applied Superconductivity*, *15*(2), 1915-1918.

Islam, M., Okasha, M., & Sulaeman, E. (2019). A model predictive control (MPC) approach on unit quaternion orientation based quadrotor for trajectory tracking. *International Journal of Control, Automation and Systems*, *17*(11), 2819-2832.

Itani, K., De Bernardinis, A., Khatir, Z., & Jammal, A. (2016). Energy management of a battery-flywheel storage system used for regenerative braking recuperation of an Electric Vehicle. IECON 2016-42nd Annual Conference of the IEEE Industrial Electronics Society,

Kabala, M. (2017). *Application of distributed DC/DC electronics in photovoltaic systems* Colorado State University. Libraries].

Kamibayashi, M., & Tanaka, K. (2001). Recent sodium sulfur battery applications. 2001 IEEE/PES Transmission and Distribution Conference and Exposition. Developing New Perspectives (Cat. No. 01CH37294),

Karamanakos, P., Mattila, R., & Gever, T. (2018). Fixed switching frequency direct model predictive control based on output current gradients. IECON 2018-44th Annual Conference of the IEEE Industrial Electronics Society,

Kasprzyk, L. (2017). Modelling and analysis of dynamic states of the lead-acid batteries in electric vehicles. *Eksploatacja i Niezawodność*, *19*.

Kersting, S., & Buss, M. (2017). Direct and indirect model reference adaptive control for multivariable piecewise affine systems. *IEEE Transactions on Automatic Control*, *62*(11), 5634-5649.

Khaligh, A., & Li, Z. (2010). Battery, ultracapacitor, fuel cell, and hybrid energy storage systems for electric, hybrid electric, fuel cell, and plug-in hybrid electric vehicles: State of the art. *IEEE transactions on Vehicular Technology*, *59*(6), 2806-2814.

Khan, F., & Tolbert, L. (2009). Bi-directional power management and fault tolerant feature in a 5-kW multilevel dc–dc converter with modular architecture. *IET Power Electronics*, *2*(5), 595-604.

Khan, M. S., Ahmad, I., & Abideen, F. Z. U. (2019). Output Voltage Regulation of FC-UC Based Hybrid Electric Vehicle Using Integral Backstepping Control. *IEEE access*, *7*, 65693-65702.

Khan, M. S., Ahmad, I., Armaghan, H., & Ali, N. (2018). Backstepping sliding mode control of FC-UC based hybrid electric vehicle. *IEEE Access*, *6*, 77202-77211.

Kolli, A., Gaillard, A., De Bernardinis, A., Bethoux, O., Hissel, D., & Khatir, Z. (2015). A review on DC/DC converter architectures for power fuel cell applications. *Energy Conversion and Management*, *105*, 716-730.

Kurtz, M. J., & Henson, M. A. (1998). Feedback linearizing control of discrete-time nonlinear systems with input constraints. *International Journal of Control*, *70*(4), 603-616.

Lai, C.-M., Cheng, Y.-H., Hsieh, M.-H., & Lin, Y.-C. (2017). Development of a bidirectional DC/DC converter with dual-battery energy storage for hybrid electric vehicle system. *IEEE transactions on Vehicular Technology*, *67*(2), 1036-1052.

Landau, I. (1969). A hyperstability criterion for model reference adaptive control systems. *IEEE Transactions on Automatic Control*, *14*(5), 552-555.

Lee, C.-M., Han, S.-H., Zheng, C.-H., & Lin, W.-S. (2012). Power split of fuel cell/ultracapacitor hybrid power system by backstepping sliding mode control. 2012 10th International Power & Energy Conference (IPEC),

Levant, A. (2007). Principles of 2-sliding mode design. *automatica*, *43*(4), 576-586.

Lex, P., & Matthews, J. (1992). Recent developments in zinc/bromine battery technology at Johnson Controls. IEEE 35th International Power Sources Symposium,

Li, G., Lu, X., Kim, J. Y., Meinhardt, K. D., Chang, H. J., Canfield, N. L., & Sprenkle, V. L. (2016). Advanced intermediate temperature sodium–nickel chloride batteries with ultra-high energy density. *Nature communications*, *7*(1), 1-6.

Li, J., Gee, A. M., Zhang, M., & Yuan, W. (2015). Analysis of battery lifetime extension in a SMES-battery hybrid energy storage system using a novel battery lifetime model. *Energy*, *86*, 175-185.

Li, J., Zhang, M., Yang, Q., Zhang, Z., & Yuan, W. (2016). SMES/battery hybrid energy storage system for electric buses. *IEEE Transactions on Applied Superconductivity*, *26*(4), 1-5.

Li, W., & He, X. (2010). Review of nonisolated high-step-up DC/DC converters in photovoltaic grid-connected applications. *IEEE Transactions on Industrial Electronics*, *58*(4), 1239-1250.

Li, X., & Palazzolo, A. (2022). A review of flywheel energy storage systems: state of the art and opportunities. *Journal of Energy Storage*, *46*, 103576.

Li, Y., Gong, M., Liang, Y., Feng, J., Kim, J.-E., Wang, H., Hong, G., Zhang, B., & Dai, H. (2013). Advanced zinc-air batteries based on high-performance hybrid electrocatalysts. *Nature communications*, *4*(1), 1-7.

Linden, D., & Reddy, T. (2002). Handbook of Batteries. In: McGraw-Hill.

Liu, H., & Jiang, J. (2007). Flywheel energy storage—An upswing technology for energy sustainability. *Energy and buildings*, *39*(5), 599-604.

Liu, H., & Yang, S. (2013). Study on nonlinear phenomena in Buck-Boost converter with switched-inductor structure. *Mathematical Problems in Engineering*, *2013*.

Liu, J., Yan, Q., Qu, X., Jiang, F., Liu, W., & Huang, Z. (2014). Explicit model predictive control of bidirectional DC/DC converter for ultracapacitors energy storage unit applied to light rail vehicle. *IFAC Proceedings Volumes*, *47*(3), 10293-10298.

Liu, X., & Wu, X. (2023). A two-stage bidirectional DC-DC converter system and its control strategy. *Energy*, *266*, 126462.

Long, Z., & Zhiping, Q. (2008). Review of flywheel energy storage system. Proceedings of ISES World Congress 2007 (Vol. I–Vol. V),

Lu, L., Han, X., Li, J., Hua, J., & Ouyang, M. (2013). A review on the key issues for lithium-ion battery management in electric vehicles. *Journal of power sources*, *226*, 272-288.

Lukic, S. M., Cao, J., Bansal, R. C., Rodriguez, F., & Emadi, A. (2008). Energy storage systems for automotive applications. *IEEE Transactions on industrial electronics*, *55*(6), 2258-2267.

Lukic, S. M., Wirasingha, S. G., Rodriguez, F., Cao, J., & Emadi, A. (2006). Power management of an ultracapacitor/battery hybrid energy storage system in an HEV. 2006 IEEE Vehicle Power and Propulsion Conference,

Lundmark, S. T., Alatalo, M., Thiringer, T., & Grunditz, E. A. (2013). *Vehicle Components and Configurations*

Luo, F. L. (2001). Six self-lift DC-DC converters, voltage lift technique. *IEEE Transactions on Industrial Electronics*, *48*(6), 1268-1272.

Luo, F. L., & Ye, H. (2004). Positive output cascade boost converters. *IEE Proceedings-Electric Power Applications*, *151*(5), 590-606.

Lyapunov, A. M. (1992). The general problem of the stability of motion. *International journal of control*, *55*(3), 531-534.

Mackenzie, W. (2020). *Electric Vehicle Research*. Wood Mackenzie. https://www.woodmac.com/our-expertise/capabilities/electric-vehicles/2040-forecast/

Majeed, M. A., Khan, M. G., & Asghar, F. (2020). Nonlinear control of hybrid energy storage system for hybrid electric vehicles. *International transactions on electrical energy systems*, *30*(4), e12268.

Malachesky, P., Bellows, R., Einstein, H., Grimes, P., Kantner, E., Newby, K., & Young, A. (1982). *Design and Performance of Bipolar, Flowing Electrolye Zinc-Bromine Batteries for Electric Vehicles* (0148-7191).

Mali, V., & Tripathi, B. (2020). Thermal and economic analysis of hybrid energy storage system based on lithium-ion battery and supercapacitor for electric vehicle application. *Clean Technologies and Environmental Policy*, 1-16.

Maric, P. (2019). *2020 Toyota Prius review*. https://www.drive.com.au/reviews/2020-toyota-prius-review/

Mathworks. (2022). *Supercapacitor Model*. The MathWorks, Inc. Retrieved 20 June from https://au.mathworks.com/help/physmod/sps/ug/supercapacitor-model.html

MathWorks. (2023). *Vehicle Modeling Using Simulink*, The MathWorks, Inc. https://au.mathworks.com/videos/matlab-and-simulink-racing-lounge-vehicle-modeling-part-1-simulink-1502466996305.html

Mendoza-Torres, A., Visairo, N., Nuñez, C., Armenta, J., Rodríguez, E., & Cervantes, I. (2019). Switching rule for a bidirectional DC/DC converter in an electric vehicle. *Control Engineering Practice*, *82*, 108-117.

Mercedes-Benz, G. (2016). F-CELL in 2017 will be plug-in FCEV. *Fuel Cells Bull*, *2016*, 12.

Mesbahi, T., Bartholomeus, P., Rizoug, N., Sadoun, R., Khenfri, F., & Lemoigne, P. (2020). Advanced Model of Hybrid Energy Storage System Integrating Lithium-ion Battery and Supercapacitor For Electric Vehicle Applications. *IEEE Transactions on Industrial Electronics*.

Mira, M. C., Zhang, Z., & Andersen, M. A. (2017). Review of high efficiency bidirectional dc-dc topologies with high voltage gain. 2017 52nd International Universities Power Engineering Conference (UPEC),

Modabbernia, M. R., Khoshkbijari, F. K., Fouladi, R., & Nejati, S. S. (2013). The state space average model of buck-boost switching regulator including all of the system uncertainties. *International Journal on Computer Science and Engineering*, *5*(2), 120.

Monopoli, R. (1967). Liapunov's method for adaptive control-system design. *IEEE Transactions on Automatic Control*, *12*(3), 334-335.

Morales-Saldana, J. A., Loera-Palomo, R., Palacios-Hernández, E., & Gonzalez-Martinez, J. L. (2014). Modelling and control of a DC–DC quadratic boost converter with R 2 P 2. *IET Power Electronics*, *7*(1), 11-22.

Morandi, A., Trevisani, L., Negrini, F., Ribani, P. L., & Fabbri, M. (2011). Feasibility of superconducting magnetic energy storage on board of ground vehicles with present state-of-the-art superconductors. *IEEE transactions on applied superconductivity*, *22*(2), 5700106-5700106.

Nakad, A., Madi, M., Aaker, O., Ntantis, E. L., & Kabalan, K. Y. (2023). Comparing supercapacitors to lithium-ion batteries through measurements and simulations.

Nayak, H. K., Goswami, D., & Hablani, V. (2013). Technical review on study of compressed air vehicle (cav). *International Journal of Automobile Engineering Research & Development (IJAuERD)*, *3*(1), 81-90.

Nazir, M. S., Ahmad, I., Khan, M. J., Ayaz, Y., & Armghan, H. (2020). Adaptive control of fuel cell and supercapacitor based hybrid electric vehicles. *Energies*, *13*(21), 5587.

Nguyen, N. T., & Nguyen, N. T. (2018). *Model-reference adaptive control*. Springer.

Ortúzar, M., Moreno, J., & Dixon, J. (2007). Ultracapacitor-based auxiliary energy system for an electric vehicle: Implementation and evaluation. *IEEE Transactions on industrial electronics*, *54*(4), 2147-2156.

Ostadi, A., Kazerani, M., & Chen, S.-K. (2013). Hybrid Energy Storage System (HESS) in vehicular applications: A review on interfacing battery and ultra-capacitor units. 2013 IEEE Transportation Electrification Conference and Expo (ITEC),

Pachauri, R. K., & Chauhan, Y. K. (2016). Modeling and simulation analysis of PV fed Cuk, Sepic, Zeta and Luo DC-DC converter. 2016 IEEE 1st international conference on power electronics, intelligent control and energy systems (ICPEICES),

Pan, C.-T., Chuang, C.-F., & Chu, C.-C. (2013). A novel transformer-less adaptable voltage quadrupler DC converter with low switch voltage stress. *IEEE Transactions on Power Electronics*, *29*(9), 4787-4796.

Pan, C.-T., Chuang, C.-F., & Chu, C.-C. (2014). A novel transformerless interleaved high step-down conversion ratio DC–DC converter with low switch voltage stress. *IEEE transactions on industrial electronics*, *61*(10), 5290-5299.

Pan, C.-T., & Lai, C.-M. (2009). A high-efficiency high step-up converter with low switch voltage stress for fuel-cell system applications. *IEEE Transactions on Industrial Electronics*, *57*(6), 1998-2006.

Pany, P., Singh, R., & Tripathi, R. (2011). Bidirectional DC-DC converter fed drive for electric vehicle system. *International Journal of Engineering, Science and Technology*, *3*(3).

Papson, A., Creutzig, F., & Schipper, L. (2010). Compressed air vehicles: Drive-cycle analysis of vehicle performance, environmental impacts, and economic costs. *Transportation research record*, *2191*(1), 67-74.

Parks, P. (1966). Liapunov redesign of model reference adaptive control systems. *IEEE Transactions on Automatic Control*, *11*(3), 362-367.

Pawar, R., & Parvat, B. (2015). Design and implementation of MRAC and modified MRAC technique for inverted pendulum. 2015 International Conference on Pervasive Computing (ICPC),

Perreault, D. J., Sato, K., Selders, R., & Kassakian, J. G. (1999). Switching-ripple-based current sharing for paralleled power converters. *IEEE Transactions on Circuits and Systems I: Fundamental Theory and Applications*, *46*(10), 1264-1274.

Pires, V. F., Monteiro, J., & Silva, J. F. (2019). Dual 3-Phase Bridge Multilevel Inverters for AC Drives with Voltage Sag Ride-through Capability. *Energies*, *12*(12), 2324.

Pirooz, A., & Noroozian, R. (2016). Model predictive control of classic bidirectional DC-DC converter for battery applications. 2016 7th Power Electronics and Drive Systems Technologies Conference (PEDSTC),

Plett, G. L. (2015). *Battery management systems, Volume I: Battery modeling* (Vol. 1). Artech House.

Pop, C. I., & Dulf, E. H. (2011). Robust feedback linearization control for reference tracking and disturbance rejection in nonlinear systems. In *Recent Advances in Robust Control-Novel Approaches and Design Methods*. InTech.

Poyyamani Sunddararaj, S., S Rangarajan, S., & Gopalan, S. (2019). Neoteric fuzzy control stratagem and design of chopper fed multilevel inverter for enhanced voltage output involving plug-in electric vehicle (PEV) applications. *Electronics*, *8*(10), 1092.

Purohit, C. S., Geetha, M., Sanjeevikumar, P., Maroti, P. K., Swami, S., & Ramachandaramurthy, V. K. (2019). Performance analysis of DC/DC bidirectional converter with sliding mode and pi controller. *International Journal of Power Electronics and Drive Systems*, *10*(1), 357-365.

Putt, R. (1979). Assessment of technical and economic feasibility of zinc/bromine batteries for utility load leveling. *Final Report Gould, Inc., Rolling Meadows, IL*.

Rajarathnam, G. P., & Vassallo, A. M. (2016). *The Zinc/Bromine Flow Battery: Materials Challenges and Practical Solutions for Technology Advancement*. Springer.

Rajarshi, P., & Maksimovic, D. (2008). Analysis of PWM nonlinearity in non-inverting buck-boost power converters. 2008 IEEE Power Electronics Specialists Conference,

Ralon, P., Taylor, M., Ilas, A., Diaz-Bone, H., & Kairies, K. (2017). Electricity storage and renewables: Costs and markets to 2030. *International Renewable Energy Agency: Abu Dhabi, United Arab Emirates*.

Ramya, K., & Jegathesan, V. (2016). Comparison of pi and pid controlled bidirectional dc-dc converter systems. *International Journal of Power Electronics and Drive Systems*, *7*(1), 56.

Ranjan, A., & Bodkhe, S. B. (2021). Modified energy management strategy for hess in electric vehicle. 2021 9th IEEE International Conference on Power Systems (ICPS),

Rashid, M. H. (2017). *Power electronics handbook*. Butterworth-Heinemann.

Rashid, M. H. (2018). *Power electronics handbook: devices, circuits, and applications handbook*. Butterworth-Heinemann.

Richards, L., Vanschalwijk, W., Albert, G., Tarjanyi, M., Leo, A., & Lott, S. (1990). Zinc-bromine battery development. *Final Report Sandia National Labs., Albuquerque, NM.*

Roy, R., Islam, M., Rashid, M., Mounis, S., Ahsan, M. M., Ahad, M. T., Siddique, Z., Kouzani, A. Z., & Mahmud, M. P. (2021). Investigation of 2dof pid controller for physio-therapeutic application for elbow rehabilitation. *Applied Sciences*, *11*(18), 8617.

Roy, R., Islam, M., Sadman, N., Mahmud, M. P., Gupta, K. D., & Ahsan, M. M. (2021). A review on comparative remarks, performance evaluation and improvement strategies of quadrotor controllers. *Technologies*, *9*(2), 37.

Runcharoon, K., & Srichatrapimuk, V. (2013). Sliding mode control of quadrotor. Technological Advances in Electrical, Electronics and Computer Engineering (TAEECE), 2013 International Conference on May 9,

Salama, H. S., & Vokony, I. (2020). Comparison of Different Electric Vehicle Integration Approaches in Presence of Photovoltaic and Superconducting Magnetic Energy Storage Systems. *Journal of Cleaner Production*, 121099.

Sharma, A., Tyagi, V. V., Chen, C., & Buddhi, D. (2009). Review on thermal energy storage with phase change materials and applications. *Renewable and Sustainable energy reviews*, *13*(2), 318-345.

Sheet, N. A. F. (2014). X-15 Hypersonic Research Program. In: Accessed: Feb.

Shtessel, Y., Edwards, C., Fridman, L., & Levant, A. (2014). Introduction: Intuitive theory of sliding mode control. In *Sliding Mode Control and Observation* (pp. 1-42). Springer.

Shyu, K.-K., Yang, M.-J., Chen, Y.-M., & Lin, Y.-F. (2008). Model reference adaptive control design for a shunt active-power-filter system. *IEEE Transactions on Industrial Electronics*, *55*(1), 97-106.

Song, Z., Hofmann, H., Li, J., Hou, J., Han, X., & Ouyang, M. (2014). Energy management strategies comparison for electric vehicles with hybrid energy storage system. *Applied Energy*, *134*, 321-331.

Song, Z., Hou, J., Hofmann, H., Li, J., & Ouyang, M. (2017). Sliding-mode and Lyapunov function-based control for battery/supercapacitor hybrid energy storage system used in electric vehicles. *Energy*, *122*, 601-612.

Song, Z., Li, J., Hou, J., Hofmann, H., Ouyang, M., & Du, J. (2018). The battery-supercapacitor hybrid energy storage system in electric vehicle applications: A case study. *Energy*, *154*, 433-441.

Storebø, F. (2021). *Bidirectional DC-DC Converter For Charging Batteries of Electric Vehicles* The University of Bergen].

Stramosk, V., & Pagano, D. J. (2013). Nonlinear control of a bidirectional dc-dc converter operating with boost-type Constant-Power Loads. 2013 Brazilian Power Electronics Conference,

Team, M. S. C. (2020). *MATLAB and Simulink Racing Lounge: Vehicle Modeling*. The MathWorks, Inc.

Team, M. S. C. (2023). *MATLAB and Simulink Racing Lounge: Vehicle Modeling*. The MathWorks, Inc.

Technology, D. U. o. (2020). EV Power Electronics. In D. U. o. Technology (Ed.), *Electric Cars: Technology*. Edx.

Thounthong, P., Chunkag, V., Sethakul, P., Davat, B., & Hinaje, M. (2009). Comparative study of fuel-cell vehicle hybridization with battery or supercapacitor storage device. *IEEE transactions on Vehicular Technology*, *58*(8), 3892-3904.

Tie, S. F., & Tan, C. W. (2013). A review of energy sources and energy management system in electric vehicles. *Renewable and sustainable energy reviews*, *20*, 82-102.

Tytelmaier, K., Husev, O., Veligorskyi, O., & Yershov, R. (2016). A review of non-isolated bidirectional dc-dc converters for energy storage systems. 2016 II International Young Scientists Forum on Applied Physics and Engineering (YSF),

Umair Ali, M., Hussain Nengroo, S., Adil Khan, M., Zeb, K., Ahmad Kamran, M., & Kim, H.-J. (2018). A real-time simulink interfaced fast-charging methodology of lithium-ion batteries under temperature feedback with fuzzy logic control. *Energies*, *11*(5), 1122.

Utkin, V. (2013). Sliding mode control of DC/DC converters. *Journal of the Franklin Institute*, *350*(8), 2146-2165.

Utomo, W. M., Bakar, A., Ahmad, M., Taufik, T., & Heriansyah, R. (2011). Online learning neural network control of buck-boost converter. 2011 Eighth International Conference on Information Technology: New Generations,

Van Mierlo, J., Van den Bossche, P., & Maggetto, G. (2004). Models of energy sources for EV and HEV: fuel cells, batteries, ultracapacitors, flywheels and engine-generators. *Journal of power sources*, *128*(1), 76-89.

Vidhya, S. D., & Balaji, M. (2019). Modelling, design and control of a light electric vehicle with hybrid energy storage system for Indian driving cycle. *Measurement and Control*, 0020294019858212.

Vijayalakshmi, S., & T Raja, S. R. (2014). Time domain based digital controller for buck-boost converter. *Journal of Electrical Engineering & Technology*, *9*(5), 1551-1561.

Walker, J., & Weil, J. (1963). The X-15 program. Heterogeneous Combustion Conference,

Wang, J., Wang, B., Zhang, L., Wang, J., Shchurov, N., & Malozyomov, B. (2022). Review of bidirectional DC–DC converter topologies for hybrid energy storage system of new energy vehicles. *Green Energy and Intelligent Transportation*, *1*(2), 100010.

Wasbari, F., Bakar, R., Gan, L. M., Tahir, M., & Yusof, A. A. (2017). A review of compressed-air hybrid technology in vehicle system. *Renewable and Sustainable Energy Reviews*, *67*, 935-953.

Weber, A. Z., Mench, M. M., Meyers, J. P., Ross, P. N., Gostick, J. T., & Liu, Q. (2011). Redox flow batteries: a review. *Journal of Applied Electrochemistry*, *41*(10), 1137.

Wen, Z., Hu, Y., Wu, X., Han, J., & Gu, Z. (2013). Main challenges for high performance NAS battery: materials and interfaces. *Advanced functional materials*, *23*(8), 1005-1018.

Wu, T.-F., & Chen, Y.-K. (1998). Modeling PWM DC/DC converters out of basic converter units. *IEEE Transactions on Power Electronics*, *13*(5), 870-881.

Wu, X., Wang, J., Zhang, Y., Du, J., Liu, Z., & Chen, Y. (2021). Review of DC-DC converter topologies based on impedance network with wide input voltage range and high gain for fuel cell vehicles. *Automotive Innovation*, *4*, 351-372.

Xing, Y., Ma, E. W., Tsui, K. L., & Pecht, M. (2011). Battery management systems in electric and hybrid vehicles. *Energies*, *4*(11), 1840-1857.

Xu, Q., Vafamand, N., Chen, L., Dragičević, T., Xie, L., & Blaabjerg, F. (2020). Review on advanced control technologies for bidirectional DC/DC converters in DC microgrids. *IEEE Journal of Emerging and Selected Topics in Power Electronics*, *9*(2), 1205-1221.

Yanarates, C., & Zhou, Z. (2022). Design and cascade PI controller-based robust model reference adaptive control of DC-DC boost converter. *IEEE access*, *10*, 44909-44922.

Yang, B., Zhu, T., Zhang, X., Wang, J., Shu, H., Li, S., He, T., Yang, L., & Yu, T. (2020). Design and implementation of Battery/SMES hybrid energy storage systems used in electric vehicles: A nonlinear robust fractional-order control approach. *Energy*, *191*, 116510.

Yang, N., Wu, C., Jia, R., & Liu, C. (2016). Modeling and characteristics analysis for a buck-boost converter in pseudo-continuous conduction mode based on fractional calculus. *Mathematical Problems in Engineering*, *2016*.

Yang, Z., Zhang, J., Kintner-Meyer, M. C., Lu, X., Choi, D., Lemmon, J. P., & Liu, J. (2011). Electrochemical energy storage for green grid. *Chemical reviews*, *111*(5), 3577-3613.

Ye, Y.-m., & Cheng, K. W. E. (2013). Quadratic boost converter with low buffer capacitor stress. *IET Power Electronics*, *7*(5), 1162-1170.

Yechiel, O., & Guterman, H. (2017). A survey of adaptive control. *International Robotics & Automation Journal*, *3*(2), 290–292.

Yoo, H.-J., Nguyen, T.-T., & Kim, H.-M. (2019). MPC with constant switching frequency for inverter-based distributed generations in microgrid using gradient descent. *Energies*, *12*(6), 1156.

Zhang, B., Mi, C. C., & Zhang, M. (2011). Charge-depleting control strategies and fuel optimization of blended-mode plug-in hybrid electric vehicles. *IEEE transactions on Vehicular Technology*, *60*(4), 1516-1525.

Zhang, H., Chen, Y., Park, S.-J., & Kim, D.-H. (2019). A Family of Bidirectional DC–DC Converters for Battery Storage System with High Voltage Gain. *Energies*, *12*(7), 1289.

Zhang, M. (2018). Battery charging and discharging research based on the interactive technology of smart grid and electric vehicle. AIP Conference Proceedings,

Zhang, X., Wang, B., Manandhar, U., Gooi, H. B., & Foo, G. (2018). A model predictive current controlled bidirectional three-level DC/DC converter for hybrid energy storage system in DC microgrids. *IEEE Transactions on Power Electronics*, *34*(5), 4025-4030.

Zhang, Y., Liu, H., Li, J., & Sumner, M. (2019). A low-current ripple and wide voltage-gain range bidirectional DC–DC converter with coupled inductor. *IEEE Transactions on Power Electronics*, *35*(2), 1525-1535.

Zhou, D., Zhao, C.-Y., & Tian, Y. (2012). Review on thermal energy storage with phase change materials (PCMs) in building applications. *Applied energy*, *92*, 593-605.

Zhou, L.-w., Zhu, B.-x., Luo, Q.-m., & Chen, S. (2013). Interleaved non-isolated high step-up DC/DC converter based on the diode–capacitor multiplier. *IET Power Electronics*, *7*(2), 390-397.

Zhou, X., & He, Q. (2015). Modeling and simulation of Buck-Boost converter with voltage feedback control. MATEC web of conferences,

Zhou, Z., Benbouzid, M., Charpentier, J. F., Scuiller, F., & Tang, T. (2013). A review of energy storage technologies for marine current energy systems. *Renewable and Sustainable Energy Reviews*, *18*, 390-400.

Zulu, A., & John, S. (2016). A review of control algorithms for autonomous quadrotors. *arXiv preprint arXiv:1602.02622*.

LIST OF PUBLICATIONS

Name	Journal	Status
Performance Analysis of PI and MRAC Algorithm in Buck–Boost Converter for Voltage Tracking in Electric Vehicle Using Simulation.	Electronics (MDPI)	Published
Comparison Analysis Between PI and Adaptive Controllers for DC-DC Converter of Hybrid Energy Storage Systems in Electric Vehicle.	International Journal of Automotive and Mechanical Engineering	Published
Analysis of Direct Model Reference Adaptive Control for Power Tracking of Electric Vehicles Based on Different Drive Cycles	Journal of Advanced Research in Applied Sciences and Engineering Technology	To be submitted